Theses and Dissertations

12-2017

Free-Space Measurements of Dielectrics and Three-Dimensional Periodic Metamaterials

Clifford E. Kintner
University of Arkansas, Fayetteville

Follow this and additional works at: http://scholarworks.uark.edu/etd

Part of the Electromagnetics and Photonics Commons, and the Optics Commons

Recommended Citation

Free-Space Measurements of Dielectrics and Three-Dimensional Periodic Metamaterials

A thesis submitted in partial fulfillment
of the requirements for the degree of
Master of Science in Electrical Engineering

by

Clifford E. Kintner
University of Arkansas
Bachelor of Science in Electrical Engineering, 2015

December 2017
University of Arkansas

This thesis is approved for recommendation to the Graduate Council.

_____
Dr. Magda El-Shenawee
Thesis Director

_____   _____
Dr. Mark Arnold   Dr. Zhong Chen
Committee Member   Committee Member

Abstract

This thesis presents the free-space measurements of a periodic metamaterial structure. The metamaterial unit cell consists of two dielectric sheets intersecting at 90 degrees. The dielectric is a polyetherimide-based material 0.001" thick. Each sheet has a copper capacitively-loaded loop (CLL) structure on the front and a cut-wire structure on the back. Foam material is used to support the unit cells. The unit cell repeats 40 times in the x-direction, 58 times in the y-direction and 5 times in the z-direction. The sample measures $12" \times 12" \times 1"$ in total. We use a free-space broadband system comprised of a pair of dielectric-lens horn antennas with bandwidth from 5.8 GHz to 110 GHz, which are connected to a HP PNA series network analyzer. The dielectric lenses focus the incident beam to a footprint measuring 1 wavelength by 1 wavelength. The sample holder is positioned at the focal point between the two antennas. In this work, the coefficients of transmission and reflection (the S-parameters S21 and S11) are measured at frequencies from 12.4 GHz up to 30 GHz. Simulations are used to validate the measurements, using the Ansys HFSS commercial software package on the Arkansas High Performance Computing Center cluster. The simulation results successfully validate the S-parameters measurements, in particular the amplitudes. An algorithm based on the Nicolson-Ross-Weir (NRW) method is implemented to extract the permittivity and permeability values of the metamaterial under test. The results show epsilon-negative, mu-negative and double-negative parameters within the measured frequency range.

Acknowledgements

I would like to thank my advisor, Dr. Magda El-Shenawee, for supporting me throughout my Masters Degree program. She has provided me a steadfast example of determination and focus, and has always encouraged me to exceed the standards to which others are held. Without this, I could not have possibly completed this work, nor could I have reached my level of expertise regarding the material contained within this document. I would also like to thank my committee members, Dr. Mark Arnold and Dr. Zhong Chen. Dr. Arnold has provided me insight into numerical methods and has taught me techniques to improve the quality of the code used in this research.

This thesis is also dedicated to the memory of Dr. Michael Glover, a good friend and colleague who was originally a member of my advisory committee.

I wish to recognize my colleagues who have provided so much support during my time at the University of Arkansas: Tyler Bowman, Sharon Brasko, Nathan Burford, Luke Gabbard, Connie Jo Howard, Dan Klein, Jeff Knox, Tracy Long, Haider Mhiesan and Pawel Wolinski.

I also wish to recognize my supervisors and colleages at the United States Army Research Laboratory in Adelphi, Maryland: Theodore Anthony, Daniel Galanos, Art Harrison, Dr. Abby Hedden, Dr. Greg Mitchell, Dr. Steve Weiss and Dr. Amir Zaghloul. They have provided me with a unique research opportunity, shared their wealth of knowledge, and have graciously supplied the metamaterial sample used in this work.

Finally, I would like to thank my mother, Carmen Barry, for all her encouragement and hard work which has enabled me to succeed in my studies; my grandparents, Mary Kintner and Clifford Kintner; and my friends and loved ones: Alexa Baker, Kedron Benham, Casey and

Tasha Cloer, Trey Davis, Colby Ford, Will Green, Harrison Grimwood, Teddi Guthrie, Danny Hickinbotham, Justin Hart, Jewel Hayes, Carla Martin, Carlton McMullen, and Justin Slavens.

Table of Contents

List of Figures

I.   Introduction

A.   Motivation

Microwave and millimeter-wave (mm-wave) technology has rapidly become an integral component of modern technology. Its development has had a profound effect on a wide range of fields, in particular the development of tools for communications, defense, medical diagnostics and nondestructive testing applications [1] [2] [3] [4].

As the field continues to develop, wireless technologies are becoming increasingly pervasive in everyday life. They have enabled internet connectivity for a wide range of consumer technologies, leading to a sharp increase in the development and use of consumer products which incorporate microwave and millimeter-wave technology [5] [6] [7] [8]. As more devices begin to include some form of wireless communication or sensing, available spectrum for such use has become increasingly congested. Continuation of this trend demands that the field of wireless communications makes advancements to ensure that new designs are possible. These advancements must make existing designs smaller or more energy efficient, make better use of available spectrum, or expand the range of frequencies which can be used in practical consumer, industrial or defense technologies.

The development of new or improved dielectric materials for microwave and millimeter-wave designs is an ongoing area of research within the field [9] [10] [11] [12]. The availability of these newer materials with desirable permittivity and permeability characteristics can enable designs at higher or lower frequencies than previously feasible. These materials can be used to make equipment smaller, more portable, or more energy-efficient. They can facilitate improvements in antenna design, leading to smaller and more efficient antennas [13] [14] [15] [16]. By enabling the design of smaller antennas, arrays can be constructed with more elements

1

within a usable area, improving their performance significantly for applications such as beam-steering radar or other beam-forming communications systems [17] [18] [19].

One class of materials, referred to as metamaterials, is another area of active research within the field of microwave and millimeter-wave design [20] [21]. Within the context of electrical engineering, these materials are designed to exhibit net electrical properties which are not ordinarily found in nature. The intent is typically to create an unusually high, low or even negative effective permittivity or permeability within the metamaterial. The metamaterials consist of a repeating unit-cell constructed from ordinary homogeneous dielectric or conductive materials. The shape and arrangement of these cells result in a net effective behavior which differs from that of the cells' constituent elements and materials, often exhibiting anisotropy with regards to permittivity and permeability. The resulting unnatural properties can enable the design of new antennas with desirable features [22], surfaces which exhibit frequency-selective behaviors and other novel uses such as radar absorption [23] or "cloaking" an object at particular wavelengths [24] [25].

To be incorporated in a functional design or an accurate simulation, the permittivity and permeability of a material must be characterized for the frequencies of interest. As permittivity and permeability cannot be measured in a direct fashion, accurate microwave and millimeter-wave measurements are needed to characterize materials. These measurements can be used to solve for the effective permittivity and permeability of a material under test, using equations derived from fundamental electromagnetic relationships, generally Fresnel's equations [26] [27]. Once these properties have been accurately characterized for a material, they can be used to design and simulate components for use in microwave and millimeter-wave systems.

B. Microwave and Millimeter-wave Measurements

Microwave and millimeter-wave measurement systems in general consist of two parts: a measurement device incorporating a frequency source and signal sampling hardware, and a connected apparatus which senses or probes the material under test (MUT). The two parts comprise a complete microwave measurement system, and both aspects have seen significant advancement as the field of microwave measurements has grown in the last half-century [2].

Traditional waveguide-based methods and resonant-cavity methods have been used for decades [28] [29]. These methods both involve placing a sample of the material under test within a metallic chamber. The propagation of an electromagnetic wave within the chamber is examined, and the sample's properties are thus determined. A significant drawback of these methods is that they require very accurate machining, both for the waveguide or resonant cavity, and for the sample of the material under test, as any gaps between the sample and the conductive lining of the sample holder will result in error. Some materials are difficult to machine precisely, and any defects can have a significant effect on the results. Since the size of the waveguide or resonant cavity decreases with frequency, the required machining tolerances become more difficult to achieve with increasing frequency [30] [31]. Further complicating matters, measurements spanning multiple waveguide frequency bands require multiple samples [32].

Free-space measurement methods have been used successfully at microwave and millimeter-wave frequencies for decades [33] [34] [35], with one of the earliest noted uses of this method attributed to J.A. Saxton and J.A. Lane in 1946 to determine the dispersive behavior of water at millimeter wavelengths [1].

Free-space Measurements

Free-space measurement techniques provide a method for determining the permittivity and permeability of a material under test. These methods are distinct from others in that they contact-less; the material under test does not make direct contact with any active component of the measurement setup, such as a coaxial probe or a waveguide segment [36] [37].

The active portion of a free-space setup is used for generating a plane-wave and measuring it after it has interacted with the material under test, either reflection from or transmission through the sample. Several methods have been used to generate a plane-wave for the purpose of material characterization [38] [39] [40].

In general, the material under test is held inside a sample holder. This holder is not in direct contact with the measurement setup, and need not contain any active components. The holder could consist of two plates, to sandwich a sample and hold it in place, or it could consist of a closed container, for measurements of liquids or gases. It is ideally constructed of a material which minimizes unwanted reflections, such as acrylic.
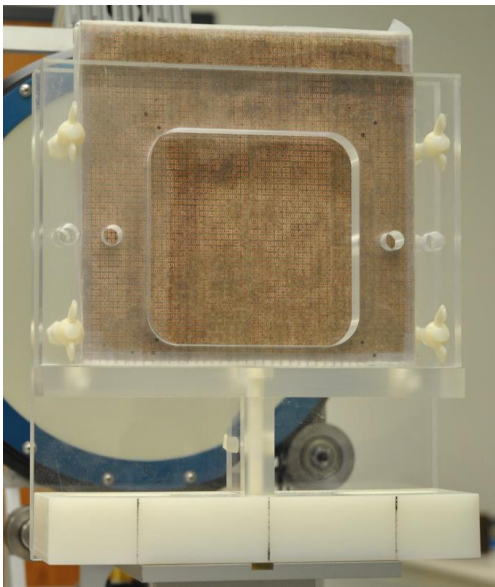
Figure I.1. Free-space sample holder with metamaterial sample between acrylic sheets.

Historical Development of Free-Space Measurements

The development of microwave and millimeter-wave technologies in the 20th and early 21st centuries have enabled measurements at progressively higher frequencies [2] [41]. Over time, the accuracy and bandwidth of measurements have been pushed higher as the technology has been refined. A review of key works related to free-space measurements follows, which serves to reinforce the validity of the free-space measurement technique.

In the 1940s, microwave free-space experiments had reached up to 50 GHz in a few cases [1]. The measurements were largely focused on developing an understanding of wave propagation in the Earth's atmosphere for communications and radar applications, in part due to the onset of World War II. Thus, much of the research on free-space measurement and characterization of dielectrics was performed on water in liquid and gaseous states, to better understand its effects on free-space wave propagation [1] [33] .

By the end of the decade, Michelson-type interferometers adapted to microwave frequencies were being used for free-space measurements of artificial dielectric samples. B. A. Lengyel used such an apparatus at the United States Naval Research Laboratory in 1948 to perform measurements on dielectric samples in sheet form [38]. This measurement technique provided both amplitude and phase information, though it was limited to measurements at normal incidence and at wavelengths about 3.2 cm. It suffered from inaccuracies due to multiple reflections occurring within samples with a refractive index greater than 1.5; it was also challenged by highly reflective samples, which lead to multiple reflections inside the measurement setup itself. It was noted in this and later works that the loss-tangent of a sample was difficult to obtain accurately with such a setup [30]. These issues are described in further detail in the following sections: I.B *Microwave and Millimeter-wave Measurements*, *Reflection-mode Measurements*, I.B *Microwave*

and Millimeter-wave Measurements, *Transmission-mode Measurements* and I.B *Microwave and Millimeter-wave Measurements*, *Sample Thickness and Loss Tangent Considerations*.

In 1952, W. Culshaw used a spectrometer setup consisting of a klystron source paired with horn antennas to perform free-space measurements of materials at wavelengths around 1.24 cm [31]. This experiment was performed by measuring the amplitude of a microwave beam reflected by a planar dielectric sample at varying oblique incidence. The dielectric constant at the measured frequency was then determined by analysis of the reflectivity vs. angle curves for both parallel and perpendicular polarizations. The perpendicular polarization was found to give the clearest measurement and thus most accurate determination of dielectric constant, while the Brewster angle was apparent in the parallel polarization measurements [31].

This experimental setup was notable in that its horn antennas incorporated dielectric lenses made of polystyrene, which were used to reduce the divergence of the microwave beam. Despite this, it was noted by the author that diffraction effects about the sample were significant enough to deviate significantly from the ideal plane-wave condition. These diffraction effects were reduced by orienting the polarization of the wave perpendicular to the plane of incidence [31].

In the early 1960s, Fabry-Perôt type interferometers were used to perform millimeter-wave measurements of dielectric materials at progressively higher frequencies [42];. In 1961, W. Culshaw and M. V. Anderson used such an interferometer to measure the complex relative permittivity of Teflon, polystyrene and Plexiglas at wavelengths of 6 mm and 3.4 mm [30]. This setup also used waveguide-fed horns and dielectric lenses to reduce the divergence of the microwave beam and thus reduce unwanted diffraction effects, as with Culshaw's setup in 1952. While the measurements were performed in free space, a resonator-type experimental setup was used; spacing between the horns was varied slightly, and the change in the calculated resonance Q

was used to determine the real part of permittivity. This experiment had similar difficulties in measuring the loss-tangent of low-loss dielectrics, except in the case where the sample thickness was a half-wavelength within the medium [30].

By the late 1960s, microwave measurement technology had advanced from the single-frequency measurements performed in the aforementioned works, with broad-band measurements performed in the time-domain by A. M. Nicolson using a tunnel diode-based pulse generator and a high-frequency sampling oscilloscope [43]. By 1970, A. M. Nicolson and G. F. Ross had expanded upon this technique toward the characterization of dielectric materials [44]. While not performed in free-space, this work had a significant impact on later free-space measurements. This was not only due to the broad-band nature of the measurements, but also due to the clear relationships presented between measured transient response and material properties. Their technique allowed the complex permittivity and permeability to be determined from 400 MHz up to 9.6 GHz. This method is discussed in detail later in the section II.D *Extraction of Permittivity and Permeability*, *Nicolson-Ross-Weir Method*.

In 1974, the increasing popularity of microwave network analyzers allowed W. B. Weir to propose their use for determining material properties [45]. Weir's work presents an adaptation of the method described by Nicolson and Ross; his technique differs by using the frequency-domain scattering parameters rather than the transient response. Weir was able to perform broad-band measurements from 8.2 GHz up to 12.4 GHz.

Nicolson, Ross and Weir's published results were band-limited due to the nature of their experimental setups and were not performed in free-space. In their works, samples were placed inside a waveguide structure, which limits the usable frequency range for measurements and requires that samples be precisely machined to fit. A technique was proposed by A. L. Cullen in

1987 that allowed for the measurement of much broader frequency ranges by measuring the sample in free-space [26]. This eliminated the need for waveguides and allowed for samples to be measured nondestructively, without altering them to fit precisely within a waveguide.

In 1989, D. K. Ghodgaonkar, V. V. Varadan and V. K. Varadan presented a free-space microwave measurement system which was the precursor to the free-space measurement system in use today at the University of Arkansas [29]. This system consisted of a pair of horn antennas with dielectric lenses connected to a network analyzer. The system bandwidth was 14.5 GHz to 17.5 GHz. Calibration was performed with the TRL method, which is discussed in detail later in the section I.B *Microwave and Millimeter-wave Measurements*, *Through Reflect Line (TRL) Calibration*, and was augmented with time-domain gating, discussed in detail later in the section I.B, *Microwave and Millimeter-wave Measurements*, *Calibration Plane*. This published work performed reflection-mode measurements (discussed in detail later in the section I.B *Microwave and Millimeter-wave Measurements*, *Reflection-mode Measurements*) and used a unique method to calculate the dielectric constant and loss-tangent for slabs of dielectric material (discussed in detail later in the section II.D *Extraction of Permittivity and Permeability*, *Ghodgaonkar's Method*).

The researchers in [29] presented results for quartz, Teflon and PVC and concluded that free-space measurements were accurate and that the results were comparable to waveguide-based techniques. They also found that the spot-focus microwave beam (approximately 1 wavelength in footprint) did not suffer significant diffraction effects for samples larger than 3 beam-widths. They noted that the iterative solution method used could result in ambiguous solutions for samples thicker than a quarter-wavelength in the medium, unless two samples of differing samples were measured [29].

In 1990, Ghodgaonkar et al. expanded on their measurement system, widening the bandwidth up to 40 GHz and modifying their technique to work with transmission-mode measurements [46]. Results were presented from 8.6 GHz to 13.4 GHz for Teflon and borosilicate glass, reporting less than 5% error at mid-band for both complex permittivity and complex permeability using the technique on samples approximately one quarter-wavelength thick.

Inaccuracy was noted with low-loss materials, with the authors suggesting reflection measurements to determine this accurately for nonmagnetic materials [46]. For thin, flexible samples, the technique of sandwiching a sample between quartz plates was used to prevent the samples from sagging and thus deflecting the microwave beam. The thickness of the quartz plates was λ_m / 2 at mid-band, where λ_m is the wavelength inside the quartz plates. To compensate for their presence, the technique of de-embedding was employed, which is discussed in further detail in the section I.B *Microwave and Millimeter-wave Measurements*, *De-embedding*.

Plane Waves and Propagation

The simplest wave-type solutions to Maxwell's equations describe a wave which propagates in the z-direction without variation in the x- or y-directions, called a plane wave [47]. Consider the case of a plane wave propagating in the z-direction, incident upon a perfectly flat sample. When the sample is oriented normal to the direction of propagation, the phase distribution along the sample's face is uniform [48]. If the sample is oriented off-normal, the phase distribution varies as a function of the angle of incidence [31] [49]. The physical approximation of this uniform phase-front condition has typically been required for free-space measurements of the dielectric properties of materials [32] [38] [39] [50]. In empty space, these wave-type solutions take a form whose components are like the one shown below [47]:

$$\hat{E}_x(z) = \hat{E}_x^+(z) + \hat{E}_x^-(z) = \hat{E}_m^+ e^{-j\omega\sqrt{\mu_0\varepsilon_0}z} + \hat{E}_m^- e^{j\omega\sqrt{\mu_0\varepsilon_0}z} \qquad (\text{I.1})$$

where in this case, $\hat{E}_x(z)$ is the x-component of a z-travelling wave, with parts $\hat{E}_x^+(z)$ travelling forward in z and $\hat{E}_x^-(z)$ travelling reversed; $\hat{E}_m^+$ and $\hat{E}_m^-$ are the amplitudes of these waves, ω is the frequency of the wave in radians, and ε_0 and μ_0 are the permittivity and permeability of vacuum, respectively. In an unbounded conductive region, these solutions must account for the permittivity, permeability and conductivity σ of the medium [47]:

$$\hat{\varepsilon} = \varepsilon' - j\varepsilon'' = \varepsilon - j\frac{\sigma}{\omega} = \varepsilon_0\varepsilon_r - j\frac{\sigma}{\omega} \tag{I.2}$$

where ε' and ε'' are the real and imaginary parts. The wave solutions then become:

$$\hat{E}_x(z) = \hat{E}_m^+ e^{-j\omega\sqrt{\mu[\varepsilon-j(\frac{\sigma}{\omega})]}z} + \hat{E}_m^- e^{j\omega\sqrt{\mu[\varepsilon-j(\frac{\sigma}{\omega})]}z} \tag{I.3}$$

This is often written in terms of the complex propagation constant γ:

$$\hat{E}_x(z) = \hat{E}_m^+ e^{-\gamma z} + \hat{E}_m^- e^{\gamma z} \tag{I.4}$$

$$\gamma = j\omega\sqrt{\mu(\varepsilon - j\frac{\sigma}{\omega})} = \alpha + j\beta \tag{I.5}$$

In this form, the attenuation constant α and the phase constant β are given by:

$$\alpha = \frac{\omega\sqrt{\mu\varepsilon}}{\sqrt{2}}[\sqrt{1 + \left(\frac{\sigma}{\omega\varepsilon}\right)^2} - 1]^{1/2} \tag{I.6}$$

$$\beta = \frac{\omega\sqrt{\mu\varepsilon}}{\sqrt{2}}[\sqrt{1 + \left(\frac{\sigma}{\omega\varepsilon}\right)^2} + 1]^{1/2} \tag{I.7}$$

This may be used to calculate the wavelength λ from the familiar form:

$$\lambda = \frac{2\pi}{\beta} \tag{I.8}$$

The interaction between a plane wave and a dielectric material under test results in some amount of reflection as described by Fresnel's equations, with the generalized relationship between a material and its reflection provided by J. A. Stratton as follows [48]:

$$\Gamma_{\parallel} = \frac{\sqrt{\mu_r\varepsilon_r - sin^2\theta_i} - \varepsilon_r\cos\theta_i}{\sqrt{\mu_r\varepsilon_r - sin^2\theta_i} + \varepsilon_r\cos\theta_i} \tag{I.9}$$

$$\Gamma_\perp = \frac{\mu_r \cos\theta_i - \sqrt{\mu_r \varepsilon_r - \sin^2\theta_i}}{\varepsilon_r \cos\theta_i + \sqrt{\mu_r \varepsilon_r - \sin^2\theta_i}} \tag{I.10}$$

where $\Gamma_\parallel$ represents the reflection coefficient for an incident wave polarized parallel to the incidence plane, and $\Gamma_\perp$ represents the reflection coefficient for an incident wave polarized normal to the incidence plane, with angle of incidence θ_i.

An additional relationship of note is that of the Brewster angle, whose basis is Snell's Law. Snell's law relates the angle of incidence θ_i of a plane wave occurring from a region of permittivity ε_1 and permittivity μ_1 to the angle of transmission θ_t inside a region of permittivity ε_2 and permittivity μ_2. Snell's law can be stated as [47]:

$$\frac{\sin\theta_i}{\sin\theta_t} = \sqrt{\frac{\mu_2 \varepsilon_2}{\mu_1 \varepsilon_1}} \tag{I.11}$$

For the parallel polarization case, a particular angle of incidence will result in zero reflection, known as the Brewster angle. The Brewster angle can be derived by setting equation (I.9) equal to zero and substituting Snell's law, equation (I.11) yields the following [47]:

$$\sin\theta_i = \left[\frac{\frac{\mu_2 \varepsilon_1}{\mu_1 \varepsilon_2} - 1}{\left(\frac{\varepsilon_1}{\varepsilon_2}\right)^2 - 1}\right]^{1/2} \tag{I.12}$$

which for nonmagnetic materials ($\mu = \mu_0$), reduces to the familiar case [47]:

$$\tan\theta_i = \sqrt{\frac{\varepsilon_2}{\varepsilon_1}} \tag{I.13}$$

where θ_i is the Brewster angle, ε_2 is the permittivity of the dielectric slab, and ε_1 is the permittivity of the bounding media, such as free space. By varying the angle of incidence and using an appropriate choice of polarization, the real part of the permittivity of a dielectric can be determined via the Brewster angle [34] [51] [52] [52].

Multiple reflections may occur within a dielectric slab, as shown below in Figure I.2.
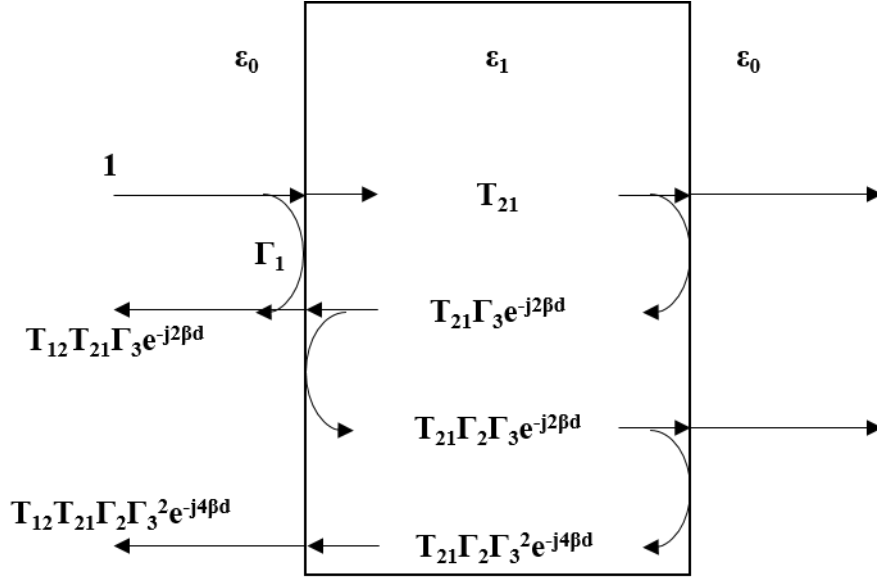
Figure I.2. Diagram showing multiple reflections within a dielectric slab.

C. K. Campbell provides an approximation for the expected reflection coefficient at arbitrary angles of incidence, to account for this effect [34]:

$$\Gamma \cong \Gamma_1 \cdot e^{-j2\beta d/\cos\theta}(e^{j2\beta d \cdot \cos\theta} - 1) \tag{I.14}$$

where Γ is the reflection coefficient, Γ_1 is the reflection coefficient of the reflection off the front face of the sample under test, β is the propagation phase constant along the propagation path inside the dielectric, d is the sample thickness, and θ is the angle of incidence.

Reflection-mode Measurements

Reflection-mode measurements provide the simplest method for determining the complex-valued permittivity of a material under test, in which only the reflected energy S_{11} is measured at normal incidence. Thus, it is a one-port measurement, and only a single antenna is needed. The material under test, of thickness *d*, is placed in a sample holder, and a highly-conductive, reflective backing is placed behind the sample. This configuration is shown below in Figure I.3:

12
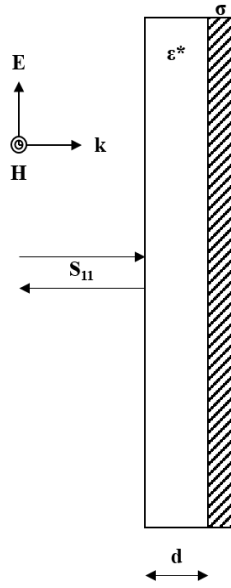
Figure I.3. Diagram of reflection-mode measurement setup.

Using equations derived from transmission line theory, the complex permittivity of the material under test is then determined iteratively using Muller's method [29] [53]. This method is detailed in the section II.D *Extraction of Permittivity and Permeability*, *Ghodgaonkar's Method*, *Reflection*. While the technique is simple to implement and provides an accurate determination of both the relative permittivity and loss-tangent of the material under test, it is only suitable for nonmagnetic materials and does not guarantee a unique solution for all sample thicknesses. This is discussed further in the section I.B *Microwave and Millimeter-wave Measurements*, *Sample Thickness and Loss Tangent Considerations*.

Transmission-mode Measurements

Transmission-mode measurements provide a method of determining both the complex permittivity and the complex permeability of a material under test. In this method, both the reflected energy S_{11} and the transmitted energy S_{21} are measured at normal incidence; thus these are sometimes referred to as Transmission/Reflection methods [54]. A matched pair of antennas

13

are required for measurements. The material under test is placed in a sample holder without a reflective backing. This configuration is shown below in Figure I.4:
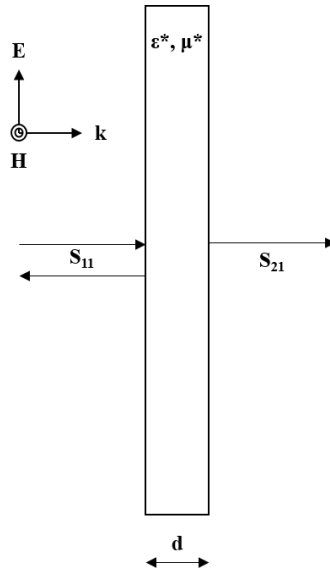
Figure I.4. Diagram of transmission-mode measurement setup.

The complex permittivity and complex permeability may then be determined directly from S_{11} and S_{21} [46]. This method is detailed in the section II.D *Extraction of Permittivity and Permeability*, *Ghodgaonkar's Method, Transmission*. Unlike reflection-mode measurements, this method allows for the measurement of ferrites or magnetic materials. However, sample thickness may have a significant impact on the calculated result.

Sample Thickness and Loss Tangent Considerations

While free-space measurement methods provide an excellent contactless, nondestructive method for determining the intrinsic properties of a material, the thickness of the sample under test may have a significant impact on the calculated result.

Of particular concern is the phenomenon of half-wavelength resonance within a sample. In the event that the sample thickness d is equal to an integer multiple of one half-wavelength inside the sample medium, resonant behavior is observed within the sample [55] [56] [57]. The

14

resonant behavior is least visible when the sample thickness is equal to an odd multiple of a quarter of a wavelength in the medium [46].

Two key reflections occur with the incident wave. The first reflection occurs at the front face of the sample (closest to the incident wave), caused by the impedance mismatch between free space and the dielectric. The un-reflected portion of the wave then enters the dielectric slab. The second reflection occurs at the back face of the sample, again caused by the impedance mismatch between the dielectric and free space. When the above sample thickness condition is met, this second reflection is exactly 180° out of phase with the incoming wave, thus it interferes destructively with the forward-travelling wave inside the dielectric [58]. If the loss-tangent of the material is relatively low, such as the case with Teflon [46], attenuation within the medium is low, and the destructive interference is significant; the resulting measured S_{11} then consists primarily of the energy reflected by the first boundary [55]. This is illustrated below in Figure I.5. The forward-travelling wave inside the dielectric is shown by a solid line, and the reverse-travelling wave caused by the second reflection is shown by a dashed line.
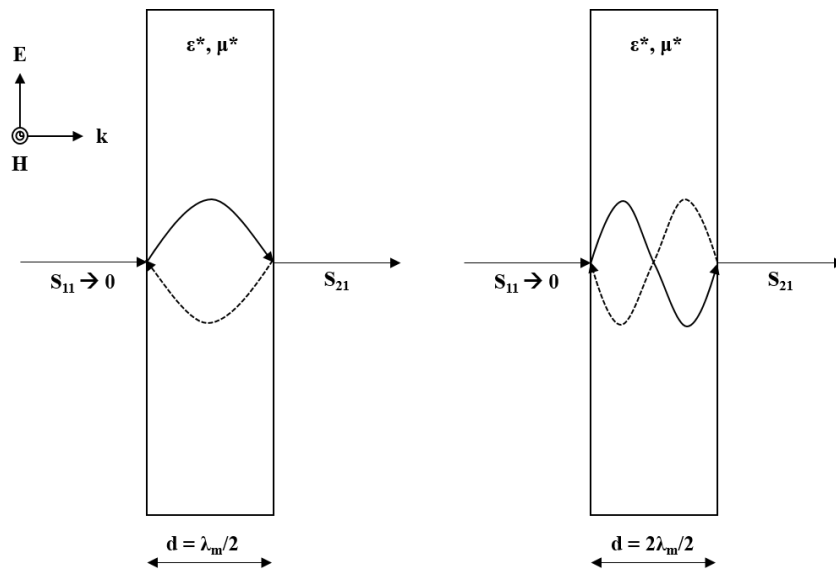
Figure I.5. Half-wavelength resonances inside a dielectric slab.

15

This resonant effect causes problems for algorithms such as the Nicolson-Ross-Weir method; this is discussed further in the section II.D *Extraction of Permittivity and Permeability, Nicolson-Ross-Weir Method.* Some earlier characterization methods actually relied on this resonance in order to determine the dielectric constant and loss tangent at a specific frequency [31] [32]. For broad-band measurements, the loss-tangent about the resonant frequency can be determined by the depth of the resonance:

$$\tan \delta = \frac{\varepsilon''}{\varepsilon'} = \frac{\Delta f}{f_0} \tag{I.15}$$

where $\tan \delta$ is the loss tangent of the dielectric at frequency f_0, the frequency of the minimum value of S_{11}, ε' is the real part of the dielectric's permittivity, ε'' is the imaginary part of the dielectric's permittivity, and Δf is the bandwidth 3 dB above the minimum.

The resonance effect is observed only in transmission-mode measurements. In reflection-mode measurements, a metal short-circuiting plate is placed behind the back face of the sample under test. As a short-circuit, the reflection coefficient at the boundary is -1, and the reflected wave is 180° out of phase, thus the second reflection interferes constructively rather than destructively [26] [59].

Network Analyzer Calibration

As with any sensitive measurement equipment, microwave systems require calibration in order to provide accurate measurements by eliminating errors due to the system and surrounding background [29] [46]. Calibration allows for the removal of systematic errors, which are assumed to be due to properties and imperfections of the measurement setup, which includes the network analyzer, cables, and any other components of the test setup [60] [61].

In general, calibration of a vector network analyzer is performed by measuring well-described references, known as calibration standards. The measurements of these standards are

compared against their known true values. The measured deviation from the standards is incorporated in a mathematical model, or error model, which provides correction factors. These correction factors are then applied to subsequent measurements, largely eliminating systematic error. The details of these calibration techniques are described below.

Network Analyzer Overview

Network analyzers are available with an arbitrary number of ports. One-port and two-port models are the most common, but models with higher numbers of ports are available. As free-space measurement techniques use one-port and two-port setups, these cases will be focused on in the discussion of the network analyzer and its error models.

The schematic overview of a network analyzer is shown below in Figure I.6 below [62]. This depicts the basic signal flow within a network analyzer. It begins with a frequency source, which is used to generate a microwave signal. This signal is detected by the incident receiver/detector (R) before reaching the material under test (MUT). The receiver/detector consists of a directional coupler and a tuned detector circuit. The portion of the incident signal which has been reflected by the MUT is sensed by a second receiver/detector (A). In the case of a two-port measurement, the transmitted signal (B) is sensed by a third receiver/detector. These uncorrected measurements are collected by the network analyzer, which then applies the correction factors determined through calibration. The resulting data is a scattering matrix (S-parameters) which characterizes the MUT in the frequency domain.
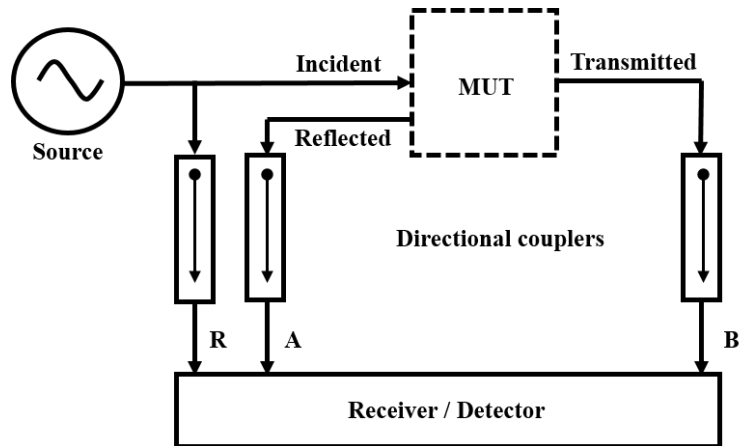
Figure I.6. Network analyzer schematic overview [63].

Calibration of the network analyzer involves a mathematical model, called the error model, which contains terms to account for the possible sources of systematic error in measurements. This model is dependent on the number of ports and the type of calibration to be employed.

One Port Model

The one port error model of the vector network analyzer is the simplest case of a network analyzer to be considered here. A single network analyzer port is used, and thus only the incident and reflected terms are collected by the network analyzer. The error model is shown in Figure I.7 below [62].

Figure I.7 shows two cases: the ideal one port measurement signal flow, and the signal flow with the error model included. In the ideal case, an incident RF signal reaches the device under test. The device reflects some amount of energy, shown as S_{11A}. The network analyzer measures this signal, S_{11M}. In this ideal case, S_{11A} is equal to S_{11M}. In reality, mechanical defects
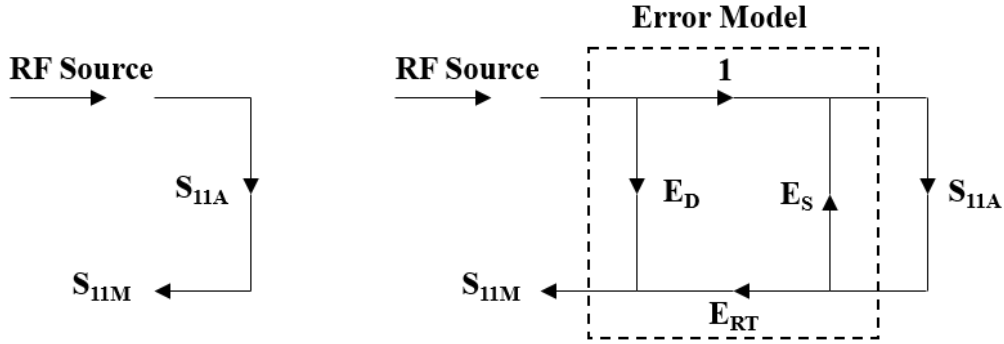
Figure I.7. Network analyzer one port error model [62].

and impedance mismatches result in a significant variance between S_{11A} and S_{11M}. These are described by the three error terms in the one port model, E_D, E_S and E_{RT}.

The E_D term, directivity error, accounts for signal leakage between the incident and reflected signal detectors. The E_S term, source match error, accounts for reflections due to an impedance mismatch between the network analyzer and the MUT. The E_{RT} term, reflection tracking error, accounts for variations in the frequency response of the receiver. The difference between the measured MUT response S_{11M} and true MUT response S_{11A} are provided by [62]:

$$S_{11M} = E_D + E_{RT}\left[\frac{S_{11A}}{1-E_S S_{11A}}\right] \tag{I.16}$$

These three terms represent the three sources of error in the signal flow graph. To fully correct for this, three calibration standards must be measured.

One Port Calibration

For one port measurements, the three calibration standards used are normally the Short, the Open and the Load. These are typically coaxial-connected reference devices provided by the network analyzer manufacturer. Their response has been tuned to match reference values which are permanently stored in the network analyzer [64].

The Open standard represents an open circuit, whereby the reflection coefficient Γ is equal to 1; in the ideal case, the incident wave is reflected completely by the calibration standard with

19

no additional change of phase. The Short standard represents a short circuit, with Γ equal to -1; the incident wave is reflected completely by the calibration standard, but with an additional 180° change in phase. The Load standard represents a matched load, such that the incident wave is completely absorbed by the load [61].

During calibration, each of these standards are measured individually by the network analyzer. The user is prompted to connect each standard, and the network analyzer performs the measurement of it. Once the calibration standards have been measured, the result is compared against the reference values stored in the network analyzer. The difference between the measured and reference values is then used to populate the terms in the error model. Calculations are automatic and handled entirely by the network analyzer. If desired, the calibration standards can be measured again with the error corrections enabled to verify the accuracy of the calibration [54].

Through Reflect Line (TRL) Calibration

For measurements involving more than one network analyzer port, a more complicated error model with additional terms is required to correct for all sources of systematic error [54]. The error model must account for cross-talk between all ports, and additional standards, such as the Through standard, must be measured. For a two-port network analyzer, the extension of the Short, Open, and Load calibration technique to Short, Open, Load and Through (SOLT) involves an error model with twelve terms, requiring seven measurements of standards [65]. This is further complicated when an object under test is not coaxially-connected, as any connected fixtures contribute to the measured S-parameters of the object under test and comparable calibration standards may be exceedingly difficult to fabricate [66]. As such, alternative calibration methods are called for, particularly in the case of free-space measurements.

The technique of Thru Reflect Line (TRL) calibration was first described by Engen and Hoer in 1979 [67]. In their work, they perform a thorough analysis of the multi-port error model. From their analysis, they determine a different set of standards which can be used to calibrate a network analyzer with two or more ports. The two-port version of their error model is shown below in Figure I.8.
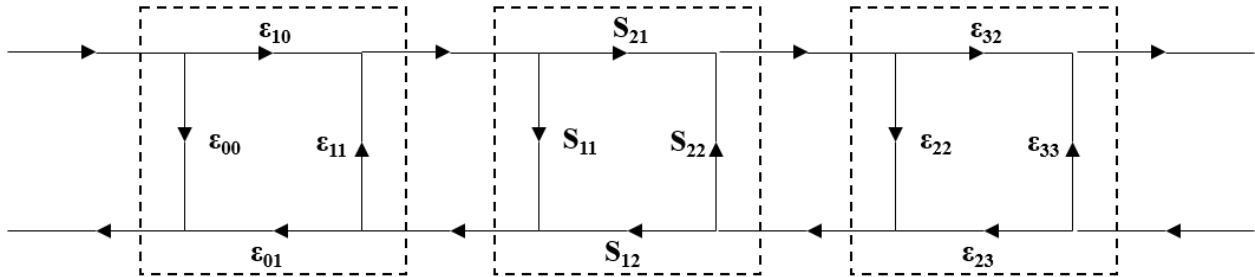
Figure I.8. TRL error model [68].

The error model contains eight unknown terms, each denoted above by ε.

Three calibration standards are used in the technique: Through, Reflect and Line. The Through, Reflect and Line standards need not be coaxial or waveguide-based; they can be fabricated to work with other measurement setups and test fixtures, such as probe stations [69]. The expected values for the calibration standards in terms of scattering parameters are as follows:

$$Thru: [S] = \begin{bmatrix} 0 & 1 \\ 1 & 0 \end{bmatrix} \tag{I.17}$$

$$Line: [S] = \begin{bmatrix} 0 & e^{-\gamma l} \\ e^{-\gamma l} & 0 \end{bmatrix} \tag{I.18}$$

$$Reflect: S_{11} = S_{22} = \Gamma \tag{I.19}$$

where [S] represents the scattering matrix representing the two-port system, γ is the complex propagation constant of the transmission line, l is the length of the transmission line, and Γ is the complex reflection coefficient. Here, the transmission line is simply free space, and l is equal to one quarter of the wavelength at mid-band; the line standard is realized by moving the receiving

antenna back by a distance equal to $\lambda / 4$ [32]. These standards are shown in terms of signal flow below in Figure I.9.
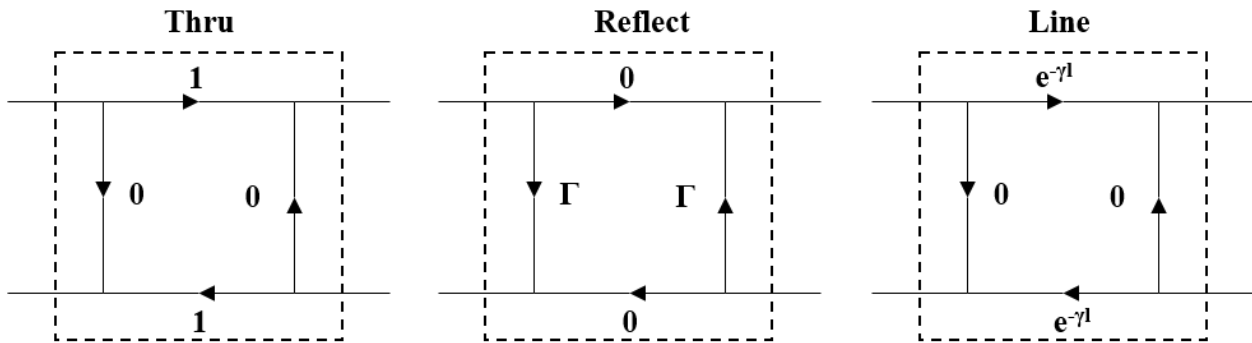
Figure I.9. TRL calibration standards [68].

This calibration technique and its associated error model is noteworthy for several reasons. This model contains eight unknown values; a total of ten measurements are performed by the network analyzer during TRL calibration, leaving the system of equations over-determined. The result of this overdetermined system is that the calibration standards need not be ideal, nor do they need to be fully characterized with the result stored in the network analyzer before calibration; only the characteristic impedance of the Line standard must be known in advance [66]. When applied to free-space measurement setups, the characteristic impedance of free space is well-known, 376.7 Ω [49].

Calibration Plane

When performing calibration of the network analyzer, it is important to differentiate between the sources of systematic error which are corrected by the calibration, and those which are not. In a signal flow graph representing the measurement setup, the boundary between these two regions is referred to as the calibration plane [45].

For coaxially-connected calibration standards, the calibration plane is set at the point where the calibration standards are connected. This is illustrated by the dashed line in Figure I.10 below.

If any adapters, cables or antennas are connected beyond this point, their response contributes to the measured scattering parameters. This unwanted response may be removed via de-embedding, but this requires a complete characterization of the devices beyond the calibration plane [70].

It is not feasible to use the technique of de-embedding to fully correct for all sources of systematic error with some measurement setups, such as free-space measurement systems. In the case of free-space measurements, de-embedding would require an accurate simulation or measurement of the measurement system itself as well as the volume surrounding it. This is because free-space measurements are sensitive to reflections from nearby objects or outside interference. Thus other calibration methods are called for in order to eliminate systematic error [71].
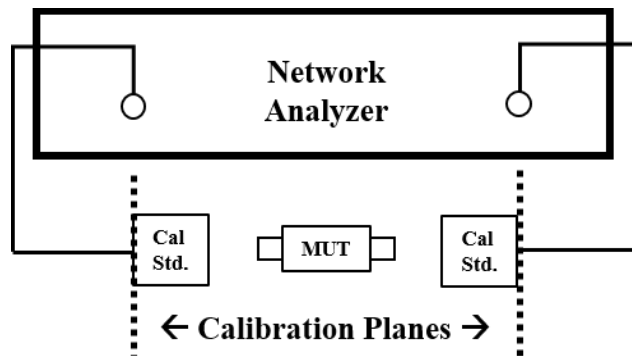
Figure I.10. Calibration plane for 2-port calibration with coaxial standards [45].

The process of TRL calibration may be used to correct for unwanted response from the measurement setup. In the case of a focused-beam free-space measurement system, the calibration plane is located at the focus of each antenna [32]. This places the calibration beyond any adapters or antennas, and thus the response from those components is corrected for by the TRL calibration process. This is illustrated by the dashed line in Figure I.11 below.
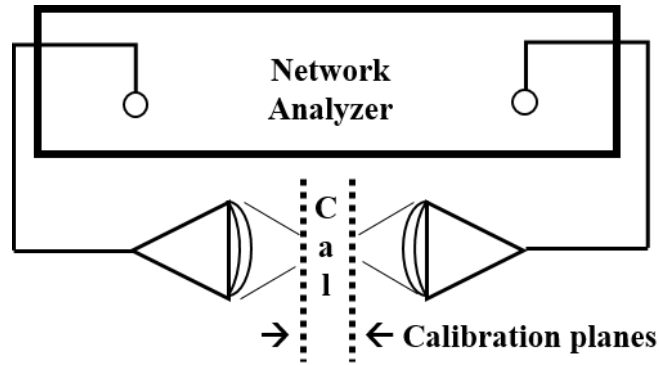
Figure I.11. Calibration plane for TRL calibration in free-space [54].

Time-domain Gating

Undesirable reflections are a significant source of error in free-space measurements [72]. These reflections have several causes, mainly cross-talk and reflections between antennas, and impedance mismatches between the sample under test and the remainder of the measurement setup [29]. These reflections must be reduced to accurately characterize a material under test [31]. The technique of time-domain gating may be used to largely eliminate these reflections, allowing for accurate characterization of a material under test [46].

Time-domain gating operates under a similar principle as frequency-domain filtering of time-domain data. With frequency-domain filtering, a time-domain signal is transformed into the frequency domain using a transform, typically the Fast Fourier Transform (FFT) [54]. Unwanted frequency components, such as low-frequency oscillations or high-frequency noise, are then filtered with a windowing function. The data is then transformed back to the time-domain with the Inverse Fast Fourier Transform (IFFT), resulting in a signal with significantly less noise [73].

Modern network analyzers perform their measurements in the frequency domain. However, due to the duality of integral transforms such as the Fourier transform, a similar filtering technique may be used, albeit in reverse. In this case, the IFFT is first used to convert the frequency-domain signal into the corresponding time-domain signal. A windowing function is applied to the time-domain signal, and the transform is reversed via the FFT. The resulting signal

24

has significantly less noise caused by reflections and impedance mismatches, allowing for an accurate characterization of the material under test [54]. This transformation process is typically performed internally by the network analyzer, using the Chirp-Z Fast Fourier Transform [73].

Results demonstrating time-domain gating are presented in the section II.E *Validation of System Performance, Results of Time Domain Gating*.

De-embedding

In the event that a thin, flexible, homogeneous sample is measured in free-space, the sample may sag or bend inside a sample holder. This deformation of the sample can result in deflection of the microwave beam, providing an inaccurate result from measurements. To correct for this, the sample may be sandwiched between two quartz plates of equal thickness [46]. Quartz is chosen as it is a rigid, low-loss material which is readily available. The measured response then includes both the response of the sample under test, as well as the response of the quartz plates. The response of the quartz plates may be removed through the technique of de-embedding [46].

De-embedding allows for the response of a component to be removed from the total measured signal. This requires that the component to be de-embedded to be fully characterized in terms of S-parameters. This characterization can be done by measurements or simulation, when measurements are not possible [69]. The S-parameters are then converted to ABCD-parameters; a series cascade of materials under test can be realized by multiplying the individual ABCD-parameter matrices of each material, and the reverse relationship can thus be easily determined [37].
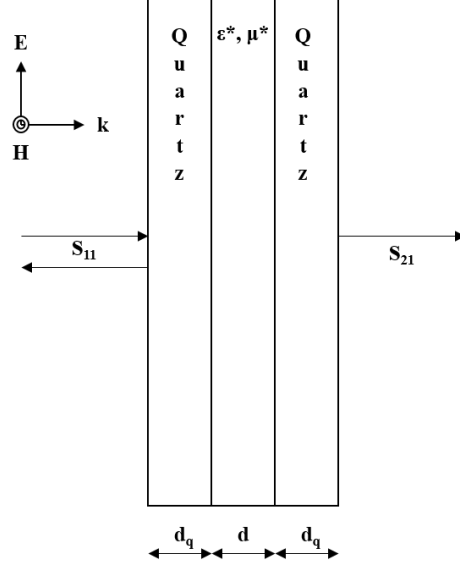
Figure I.12. Measurement of a sample sandwiched by quartz plates [46].

The ABCD matrix for the total assembly shown above in Figure I.12 is given by Ghodgaonkar, et al. as the following [46]:

$$[A^{total}] = \begin{bmatrix} A^t & B^t \\ C^t & D^t \end{bmatrix} = \frac{1}{S_{21a}} \begin{bmatrix} (1 - S_{11a}^2) + S_{21a}^2 & (1 + S_{11a}^2)^2 - S_{21a}^2 \\ (1 - S_{11a}^2)^2 - S_{21a}^2 & (1 - S_{11a}^2) + S_{21a}^2 \end{bmatrix} \qquad (I.20)$$

where S_{11a} and S_{21a} are the measured S_{11} and S_{21} values of the assembly. The ABCD matrix of the quartz plate by itself is given by [46]:

$$[A^{quartz}] = \begin{bmatrix} A^q & B^q \\ C^q & D^q \end{bmatrix} = \begin{bmatrix} \cosh(\gamma_q d_q) & Z_q \sinh(\gamma_q d_q) \\ \sinh(\gamma_q d_q)/Z_q & \cosh(\gamma_q d_q) \end{bmatrix} \qquad (I.21)$$

$$\gamma_q = \frac{j2\pi \sqrt{\varepsilon_q^*}}{\lambda_0} \qquad (I.22)$$

$$Z_q = \frac{1}{\sqrt{\varepsilon_q^*}} \qquad (I.23)$$

where γ_q is the propagation constant in quartz, λ_0 is the wavelength in free-space, and Z_q is the normalized characteristic impedance of quartz.

Due to the cascading relationship of ABCD-parameters, the relationship between the total response, the response of the quartz plates and the response of the sample is given by:

26

$$[A^{total}] = [A^{quartz}] \cdot [A^{sample}] \cdot [A^{quartz}] \qquad (I.24)$$

The response of the sample is then given by:

$$[A^{sample}] = [A^{quartz}]^{-1} \cdot [A^{total}] \cdot [A^{quartz}]^{-1} = \begin{bmatrix} A & B \\ C & D \end{bmatrix} \qquad (I.25)$$

and the S-parameters of the original sample are finally given by:

$$S_{11} = \frac{A+B-C-D}{A+B+C+D} \qquad (I.26)$$

$$S_{21} = \frac{2}{A+B+C+D} \qquad (I.27)$$

C.   Computational Electromagnetics

Introduction

Due to the sensitivity of microwave and millimeter-wave measurements, as well as the potential for error in measurement procedures, it is important to be able to verify the result of measurements to ensure that they have been performed correctly. In some cases, this can be accomplished by comparing against a published result or theory.

In many cases, however, published results for a material under test may not be available and no closed-form solution exists against which a result may be checked. In these cases, a third method can be used to check against the validity of measurements: the use of Computational Electromagnetics (CEM) modelling and simulation software.

In this method, a 3D model of a material or device under test is constructed in a 3D CAD modelling package designed for such purposes. This 3D model is decomposed by the software into a mesh of tetrahedral elements. The electromagnetic behavior of the model is then simulated by solving Maxwell's equations at points along this mesh. The results may then be compared against measurements to check if the results are in agreement. While this does not guarantee a correct result, the likelihood of performing an error in measurement and producing the same error

27

in simulation results is sufficiently low that the results can be assumed valid if both are in agreement.

Ansys HFSS

One popular Computational Electromagnetics software package which can be used for this purpose is Ansys HFSS™ (High Frequency Structure Simulator) [74] [75]. It is a general-purpose Computational Electromagnetics package which can be used to simulate the electromagnetic behavior of a variety of structures, using the Finite Element Method (FEM) to find a solution to Maxwell's equations for the model domain [76]. In this work, it is primarily used to model the behavior of a novel periodic metamaterial structure which was provided for investigation by the United States Army Research Lab.

Accurate simulation of a model requires several steps. The most obvious step is the creation of a model which accurately represents the material or physical object under test. This is achieved by building the elements of the structure with a set of 2D and 3D objects referred to as primitives, shown below in Figure I.13. These are simple geometry features such as rectangles, circles, cuboids, cylinders and other polygons which can be joined together to represent a more complex structure. Joining and separating objects is accomplished via Boolean operations, arrangement operations and duplication operations.
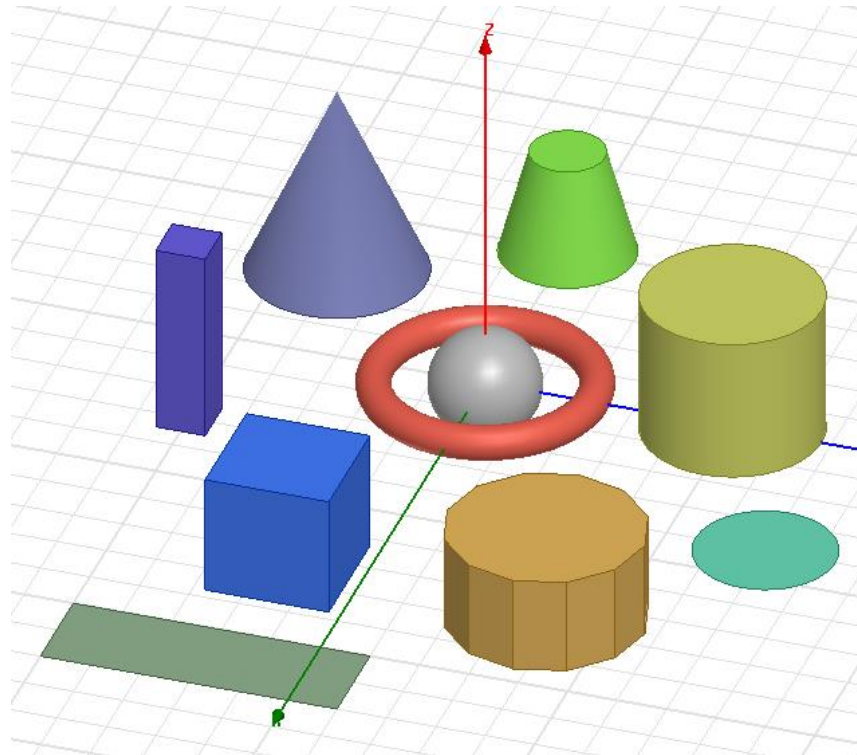
Figure I.13. HFSS 2D and 3D primitives.

An example of a structure created with primitives and Boolean operations is shown below in Figure I.14 and Figure I.15. This model represents a coaxially-fed microstrip patch antenna tuned to 2.2904 GHz. Box primitives have been used to form the antenna substrate (green) and the air (blue) surrounding the model domain. A large circle with a smaller circular cutout forms the radiating element, visible in Figure I.14. Cylindrical primitives have been used to form the coaxial feed elements, visible in Figure I.15. Boolean subtract operations have been used to subtract the cutout from the circular radiating element as well as the inner conductor from the coaxial feed, shown in the zoomed portion of Figure I.15.
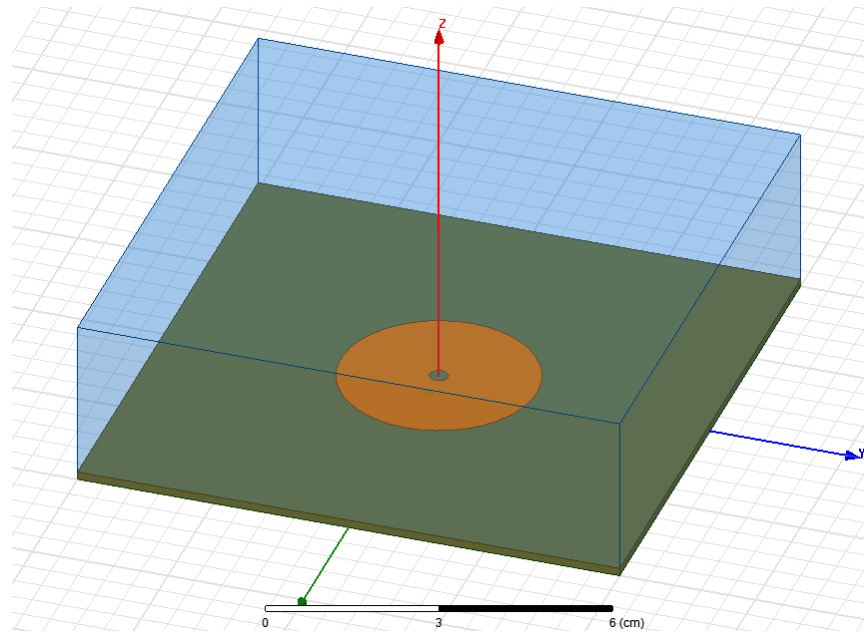
Figure I.14. Top view of coaxially-fed microstrip patch antenna model.

Three-dimensional objects must be assigned a material whose electromagnetic properties are well-defined within HFSS. An example of such a material definition is shown below in Figure I.16, which is used to model the Teflon dielectric material of the coaxial connector shown in white in Figure I.15. Of particular interest are the complex-valued relative dielectric constant, expressed as Relative Permittivity and Dielectric Loss Tangent, the complex-valued relative permeability, expressed as Relative Permeability and Magnetic Loss Tangent, and the Bulk Conductivity.
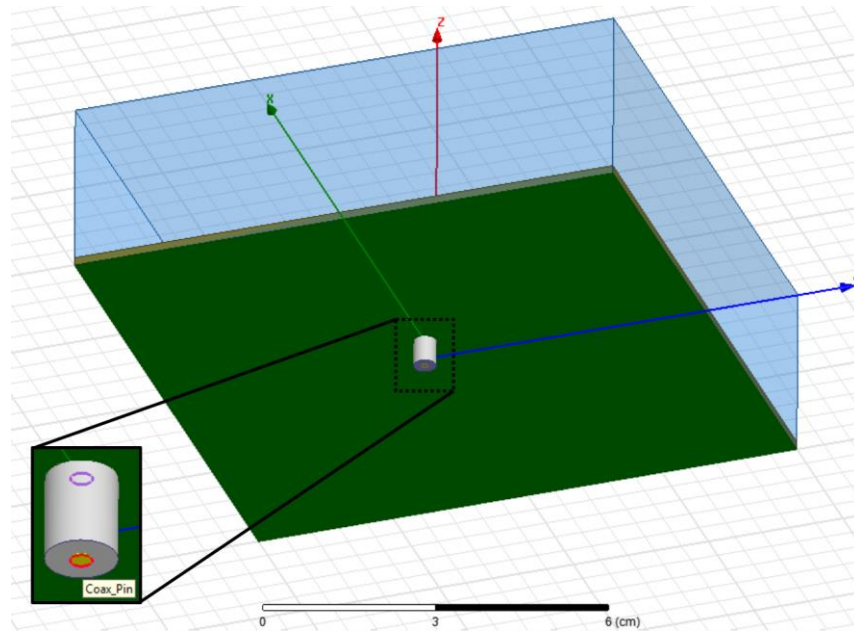
Figure I.15. Bottom view of coaxially-fed microstrip patch antenna model with detail.
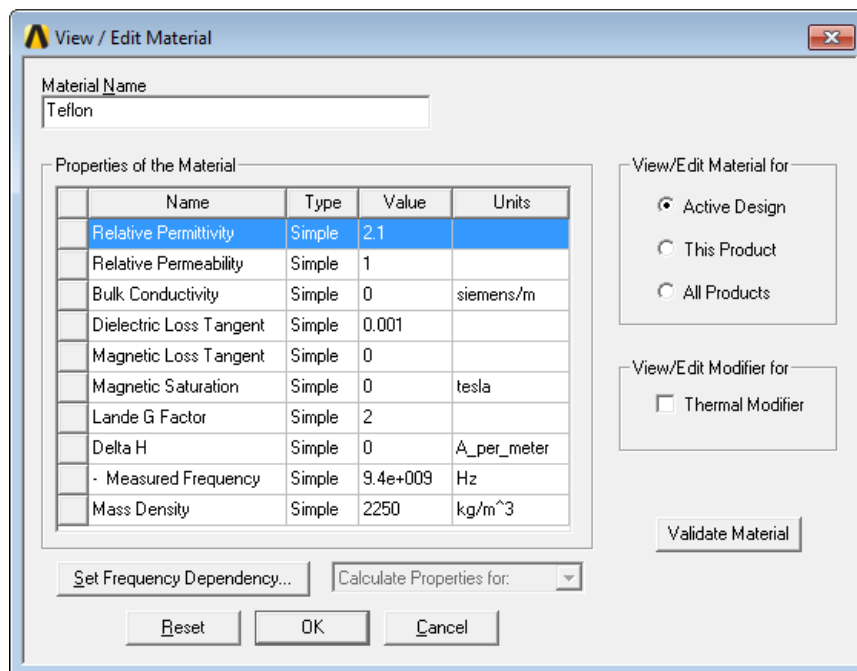
Figure I.16. Material properties for Teflon as shown in HFSS.

HFSS includes a catalog of common materials, and additional ones may be defined by the user, using either measured data or data provided by a manufacturer's data sheet.

31

Boundary Conditions

Two-dimensional objects must be assigned a boundary condition in order to interact with the simulation. These boundary conditions are used by HFSS as it computes solutions to Maxwell's equations throughout the model domain. Common boundary conditions used in a model are Radiation, Perfect E, Finite Conductivity, Perfect H, and Master/Slave boundaries, discussed in the section I.C *Computational Electromagnetics, Ansys HFSS*, *Excitations*.

Boundary conditions are typically applied to the outermost faces of the model, instructing HFSS how to handle the behavior of radiation at the boundary. The Radiation boundary type is the most commonly used in this situation, allowing electromagnetic radiation to leave the model domain. This creates an "open" model which is particularly of use for radiating structures, such as antennas. These are shown below in Figure I.17, where they have been applied to the outer faces of the air box.
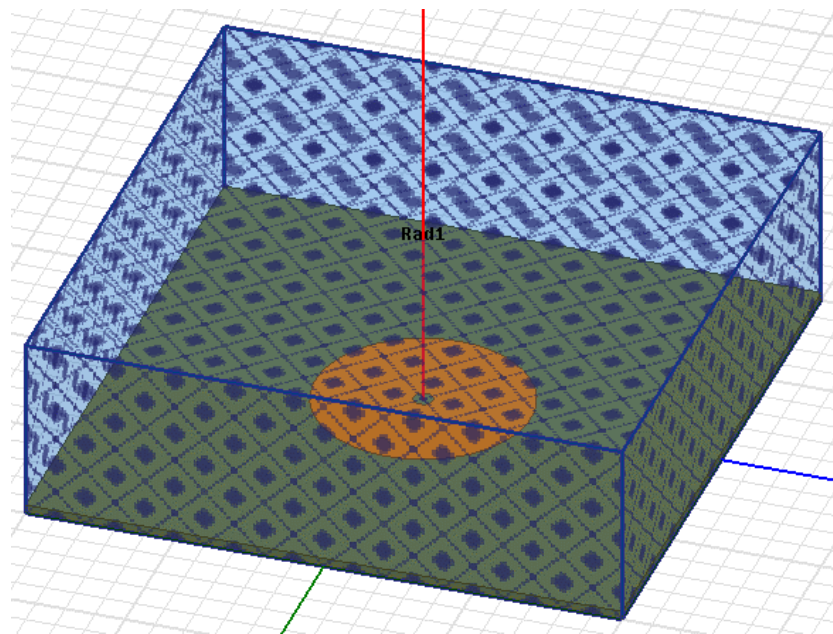
Figure I.17. Radiation boundaries in HFSS model.

The Perfect E boundary, represents a perfect electrical conductor (PEC), a conductor with infinite conductivity and zero losses. The tangential component of an electric field at this boundary

is zero, and electric fields do not penetrate the boundary. These are commonly used both inside

on the outer boundary of the model, to quickly simulate metallic 2D and 3D structures. This is

shown as the radiating element in Figure I.18, below.
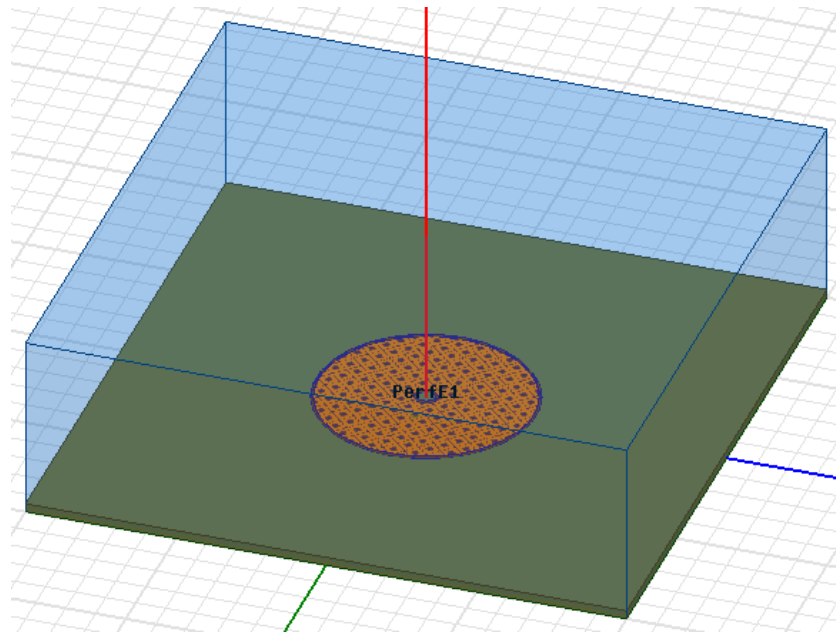
Figure I.18. PEC boundary in HFSS model.

Additionally, the PEC boundary type is used transparently by HFSS to provide the

boundary conditions needed to solve the model domain, whether or not other boundaries are

defined. HFSS assumes that a PEC boundary surrounds the outermost surfaces of the model; this

is not shown to the user but must be taken into consideration. While this boundary condition is

necessary for HFSS to reach an unambiguous solution to the simulation, it can result in unwanted

behavior. Even if a radiation boundary is specified, unwanted reflections can occur due to the

presence of the PEC boundary applied to the outermost surface of the model. For this reason, all

radiating structures should be placed at least $\lambda / 4$ away from any of the outermost boundaries of

the model, where λ is the wavelength in free space of the lowest frequency of interest. This is

commonly known as an "air box" which is modeled as a cuboid surrounding the model with either

the air or vacuum material assigned to it. This ensures that HFSS's outermost PEC boundary is

applied far enough from any radiating structure to prevent unwanted reflections from occurring in the simulation.

In the model shown above in Figure I.15, the outer metallic conductor of the coaxial feed has not been explicitly modelled; it is not needed in this case, as the air box does not extend below the substrate (see Figure I.14 above). Since HFSS wraps the outer model domain with PEC, the outer coaxial conductor is implicitly modelled. Were the air box to extend below the substrate, the outer conductor would need to be added to the model.

Excitations

With the 3D model constructed and the appropriate boundary conditions selected, the simulation requires one or more excitations assigned to it. Excitations represent an energy source or sink within the model domain. The most common types of excitations are Wave Port, Lumped Port, Floquet Port and Incident Wave. In general, Wave Ports represent energy entering or exiting the model from the outside, similar to a waveguide feed into the model. The Lumped Port is similar to this, but it represents energy entering or leaving the model from within. A Floquet Port is similar to a Wave Port, except it is adapted for use with infinite arrays; they are discussed further in the section I.C *Computational Electromagnetics, Ansys HFSS*, *Infinite Arrays*. An Incident Wave represents a source such as a plane wave or a spherical wave incident upon the model.

Since the coaxial feed in the HFSS model shown supplies energy to the antenna originating outside the model domain, a Wave Port excitation was selected and applied to the bottom face of the coaxial connector model. This is shown in an enlarged view below in Figure I.19.
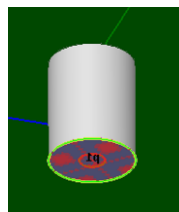
Figure I.19. Wave port excitation in HFSS model.

Infinite Arrays

Many structures of interest, such as radar antenna arrays and metamaterials, consist of a periodic structure which repeats in multiple directions [76] [40]. Simulation of a single element of such structures provides insight into the response of the element, but does not necessarily reflect the response of the total finite periodic structure. However, simulation of the total finite periodic structure may not be possible, as RAM requirements and solve time may be excessive or impossible to satisfy. HFSS provides tools to simulate an infinite array of a periodic structure, which can provide a closer approximation to the true response of a periodic structure while avoiding the requirements of simulating a finite array.

Simulation of an infinite array requires an appropriate choice of excitation and boundary conditions. Specifically, Master / Slave boundary conditions must be used for boundaries which are normal to the directions in which the infinite array should extend, and Floquet Ports must be used for any excitations which touch these boundaries.

Master / Slave Boundaries

The Master / Slave boundary conditions are used to extend a periodic structure infinitely in one direction. These are a specially matched pair of boundaries, which provide HFSS with information on how to extend the array. Radiation incident on a Master boundary is passed over to its matching Slave boundary; this is in contrast to a Radiation boundary, where incident radiation effectively leaves the model. The result of this behavior is similar to if another copy of the periodic structure existed just beyond the Master / Slave boundaries.

First, a surface must be selected and assigned a Master boundary condition. HFSS then prompts the user to define the U and V vectors for the boundary; these are an arbitrary coordinate system which gives HFSS information on how to translate energy from the Master boundary to

the Slave boundary. In general, the direction of the U and V vectors should follow the edges of the boundary's face, and should match between Master and Slave boundaries. This is illustrated below in Figure I.20. The right face has been assigned a Master boundary; its U vector (shown in red) extends parallel to the X axis, and its V vector (shown in blue) extends parallel to the Z axis. The left face has been assigned a matching Slave boundary; its U and V vectors are assigned similarly. Thus, radiation incident on the Master face "leaks over" to the matching Slave face, and the effective result is similar to an infinite array extending along the Y axis. Generally, a similar Master / Slave boundary combination would be assigned to the front and back faces of the volume, which would result in an array that extends infinitely in the X and Y directions. For clarity, this is not shown in Figure I.20.

When defining the Slave boundary, HFSS prompts the user to specify the scan angle or phase delay of the boundary. This can be used to simulate scanning through beam-steering, or a free-space separation between elements in the infinite array.
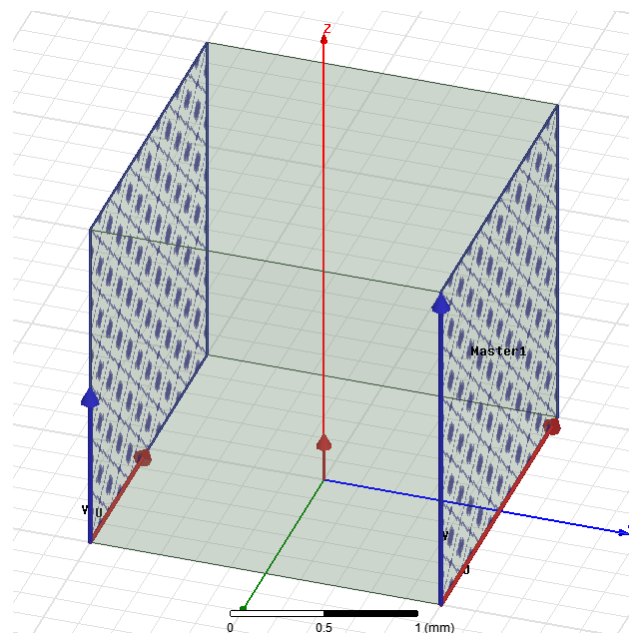
Figure I.20. Master and Slave boundaries showing U and V vectors in HFSS.

Floquet Ports

The Floquet Port excitation is used to supply energy to the infinite array model. They behave similarly to Wave Ports; they are used at outside faces of the model domain and they have modes similar to waveguide modes which determine the distribution and orientation of the electric field at their point of origin. They differ by offering compatibility with Master / Slave boundaries and providing the user control over which propagating modes are allowed or considered in mesh refinement.

As with Master / Slave boundaries, HFSS prompts the user to define A and B vectors, which are used to determine the orientation of the Floquet modes. These vectors should be aligned identically across pairs of Floquet Ports; otherwise, the ports can be cross-polarized and reject radiation unintentionally. A matching configuration of Floquet Ports is shown below in Figure I.21. Notice that the A and B vectors are aligned identically.
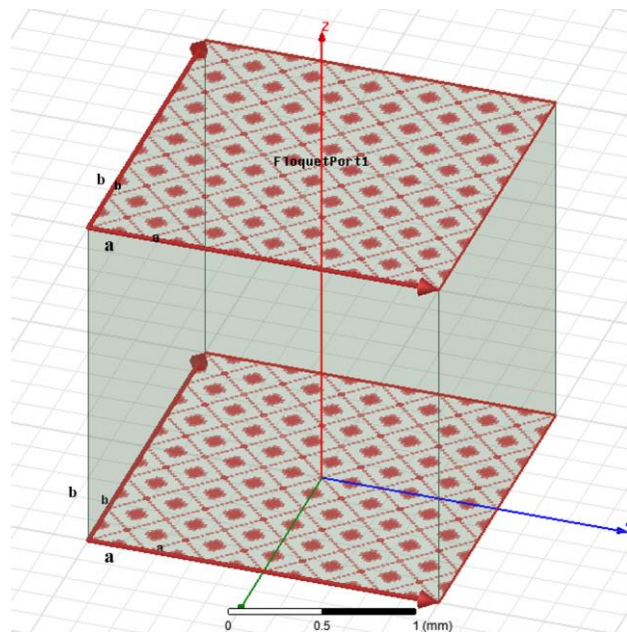
Figure I.21. Matching Floquet Ports in HFSS.

After defining the vectors, HFSS prompts the user to select the Floquet modes to be simulated. The Modes Calculator feature prompts the user for the solution frequency, then

calculates the attenuation per unit length for each mode. An example of this is shown below in Figure I.22. Modes which are strongly attenuating may then be omitted, resulting in a faster solution at little expense toward simulation accuracy.
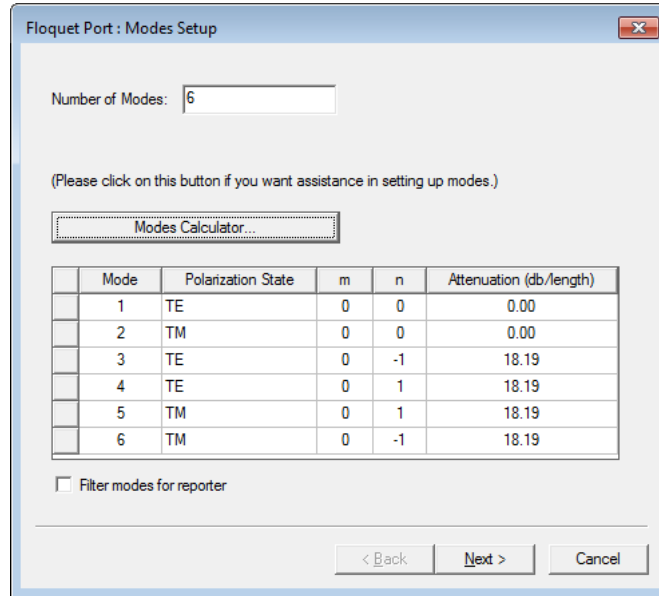
Figure I.22. Floquet mode table in HFSS.

HFSS then prompts the user to optionally de-embed the port. In this sense, de-embedding removes the unwanted phase response caused by the air box surrounding the model. The user can select a surface in the model, to which HFSS will de-embed the port and thus remove the unwanted decrease of phase as the incident wave travels through the model.

Finally, the user is prompted to choose which Floquet modes affect the refinement of the mesh. Selecting strongly attenuating modes will typically result in a model failing to converge properly. Only modes which can propagate effectively from one Floquet Port to another should be considered for refinement. Dominant modes may be selected, which can also speed up the solution process at the expense of some accuracy. This is shown below in Figure I.23.

After configuring the boundary conditions and excitations for the infinite array model, the remainder of the model may then be constructed. For this example, a mesh screen-like metallic

38
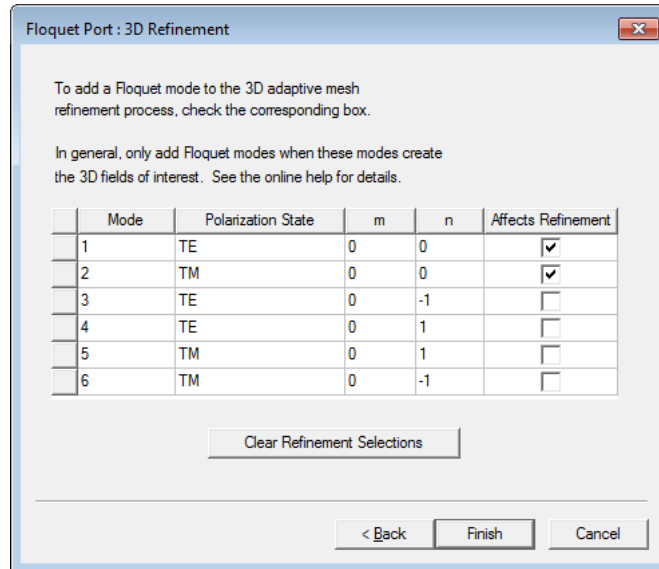
Figure I.23. Floquet mode refinement table in HFSS.

structure has been created. The completed model is shown below in Figure I.24.

Figure I.24 shows the following, clockwise from the top left: the mesh screen structure with the Perfect E boundary assigned, the Floquet Ports, the first pair of Master / Slave boundaries, and the second pair of Master / Slave boundaries. This comprises the complete model. After defining the model solution settings, simulation may commence.
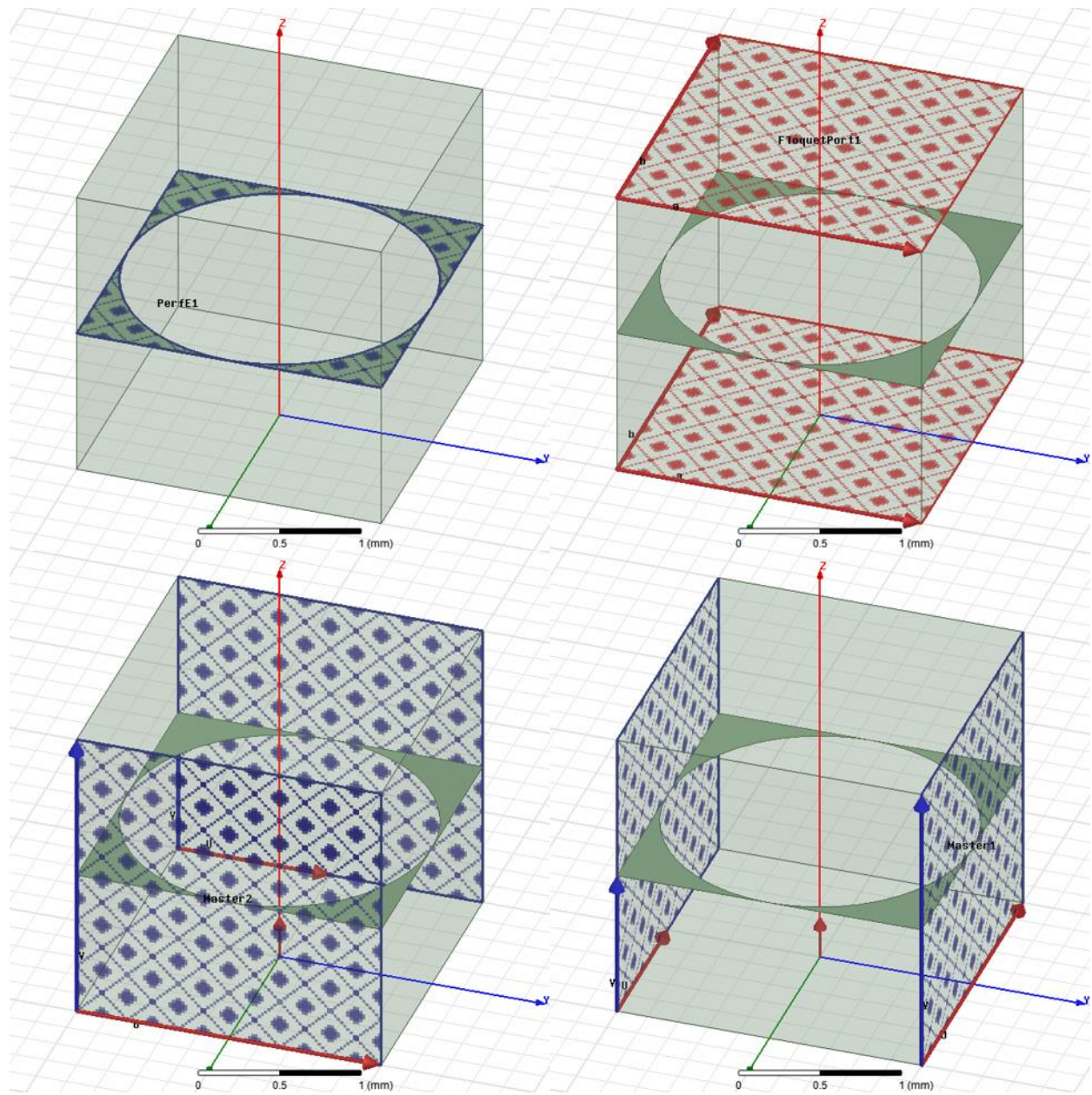
Figure I.24. Completed infinite array model in HFSS.

II.   Free-space Measurement System

The free-space measurement system in use today at the University of Arkansas is the product of years of research and development. Two generations of the system have been developed, with the modern system being used for this research.

A.   System Description

The first iteration of the free-space system was presented in the 1989 work by D. K. Ghodgaonkar, V. V. Varadan and V. K. Varadan [29]. This system consisted of a pair of focused-beam dielectric-lens horn antennas mounted to an aluminum and steel table. The system was completely manually controlled, with no motors or other automation features present. The system was designed for lower-frequency measurements, resulting in a larger beam footprint and thus requiring larger material samples to avoid diffraction effects around the edge of the sample [29]. The antennas were connected to a HP 8510B network analyzer, and material properties were extracted using a HP 9836 computer [46].

Construction

The second-generation version of the free-space measurement system was constructed around the year 2000 at Penn State University. Information regarding the construction of this system was not published, so the information presented here is believed to be the most accurate available. A motion control system was designed by the Parker and Bayside corporations, allowing for automated, repeatable antenna positioning. Proprietary software to control the system was developed over time by student researchers. The system as it stands today is shown below in Figure II.1.
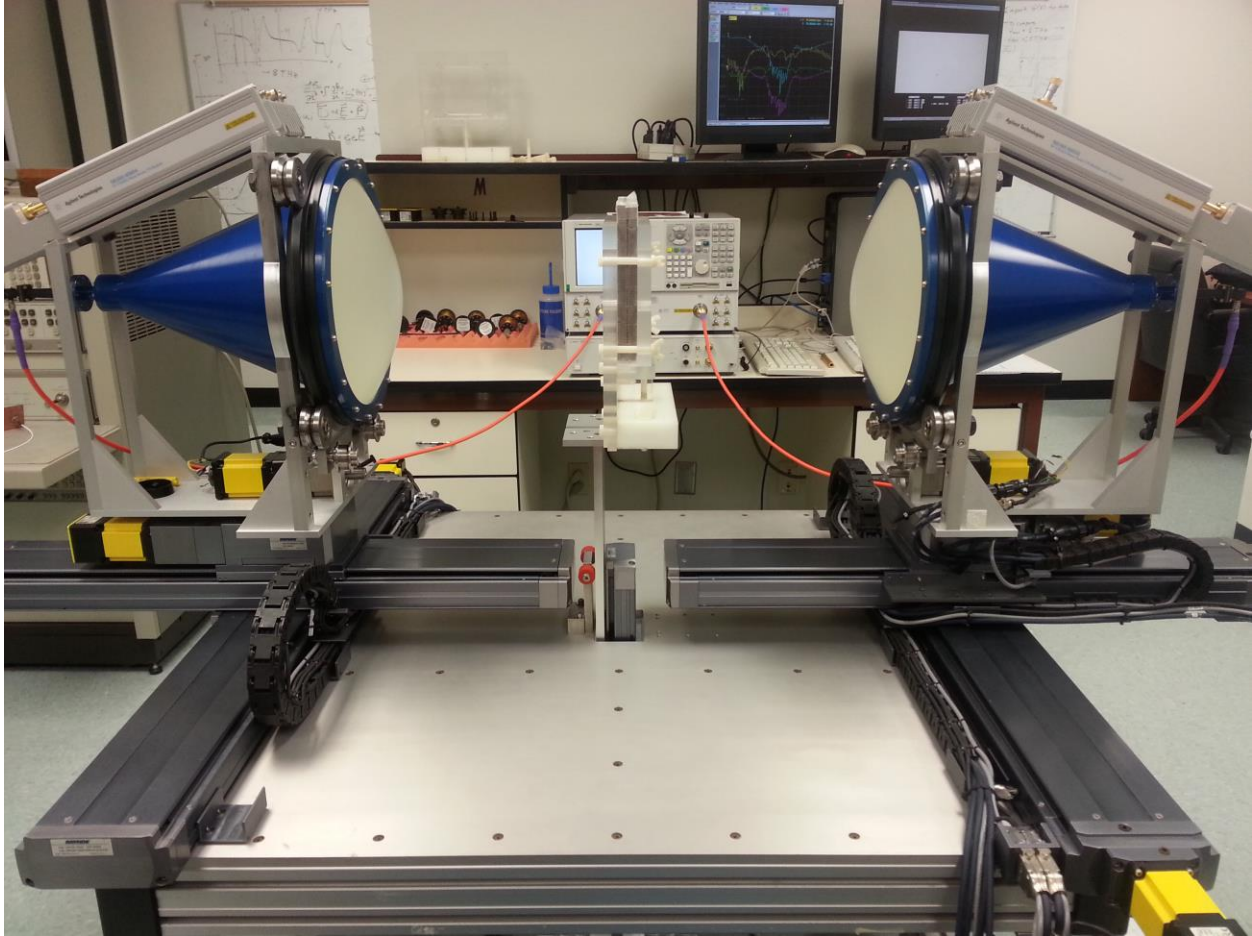
Figure II.1. Free-space measurement system.

Disassembly

When the faculty researchers moved to the University of Arkansas, they disassembled both systems and shipped them to the Engineering Research Center in Fayetteville, Arkansas. This would have required extremely careful handling, to protect the fragile dielectric lenses and other sensitive microwave components. When the faculty researchers left the University of Arkansas, the system was again disassembled and placed in storage for an indeterminate amount of time. This repeated disassembly, as well as storage in an environment uncontrolled for humidity, could have resulted in damage to the system. Any damage to these components would result in errors in measurement. This necessitated the validation of the system to ensure that its performance was

not compromised. The validation work is presented in the section II.E *Validation of System Performance*.

Description of Components

The modern free-space system at the University of Arkansas consists of many components. These components can be divided into categories which are detailed below.

Network Analyzer and Cables

The network analyzer used with the free-space system is an Agilent Technologies E8361A PNA Series model capable of measurements from 10 MHz up to 67 GHz. The network analyzer contains built-in diagnostic software which was used to verify the internal performance of the unit. All self-tests passed without error when the unit was brought online in 2015. The network analyzer is shown in operation in Figure II.2 below.
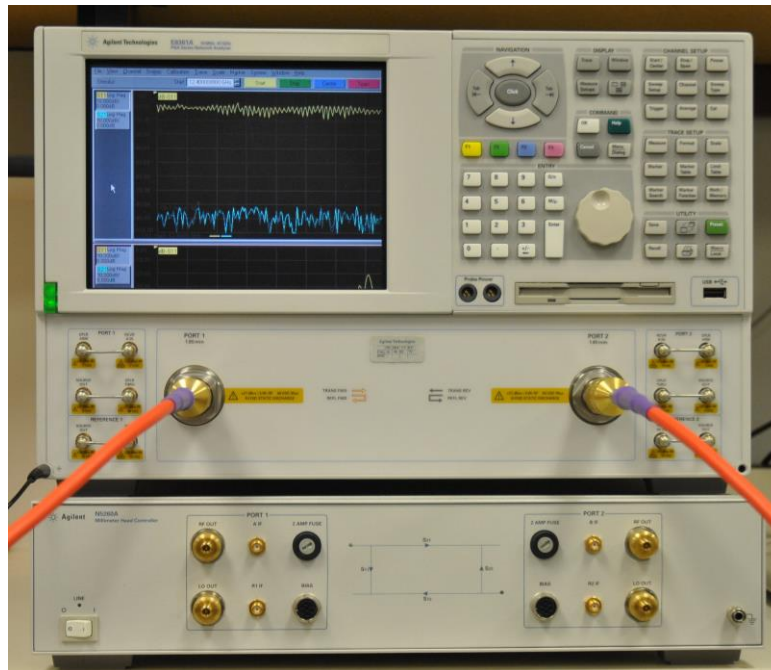
Figure II.2. Agilent E8361A network analyzer with millimeter head controller (below).

The network analyzer is equipped with a pair of 1.85 mm coaxial connectors, which connect the network analyzer to the rest of the system via microwave coaxial cables. A new pair

of cables were purchased for use with this system, as the previously used cables were not found when the system was brought out of storage. The new cables are produced by MegaPhase, RF Orange Bench Test, item TM67-V1V1-60, each measuring 60 inches in length and terminated at each end with 1.85mm male connectors. The cables' performance and phase stability was certified at the factory; cable #16001101001 has an insertion loss of 11.79 dB and a SWR of 1.42 at 67 GHz, and cable #16001101002 has an insertion loss of 11.86 dB and a SWR of 1.45 at 67 GHz. The cables are shown in Figure II.3 below.

Figure II.3. MegaPhase RF Orange Bench Test cables.

The network analyzer has an extension module, the Agilent N5260A Millimeter Head Controller, visible at the bottom of Figure II.2. The controller allows for the operation of the network analyzer up to 110 GHz. It has a second set of ports, each with 5 connectors used to connect the controller to the N5260 67-110 GHz Wave Guide T/R Modules, with one module shown below in Figure II.4.

The modules use a set of air dielectric cables to transmit down-mixed microwave signals to the network analyzer. These are shown below in Figure II.5. They are rated up to 20 GHz, with 3.5 mm male coaxial connectors on each end.

The network analyzer automatically makes use of the millimeter head controller when measurements above 67 GHz are performed. No configuration is necessary for the use of the T/R modules; they are automatically detected when all cables are connected to the millimeter head controller. When measurements below 67 GHz are performed, the T/R modules need not be
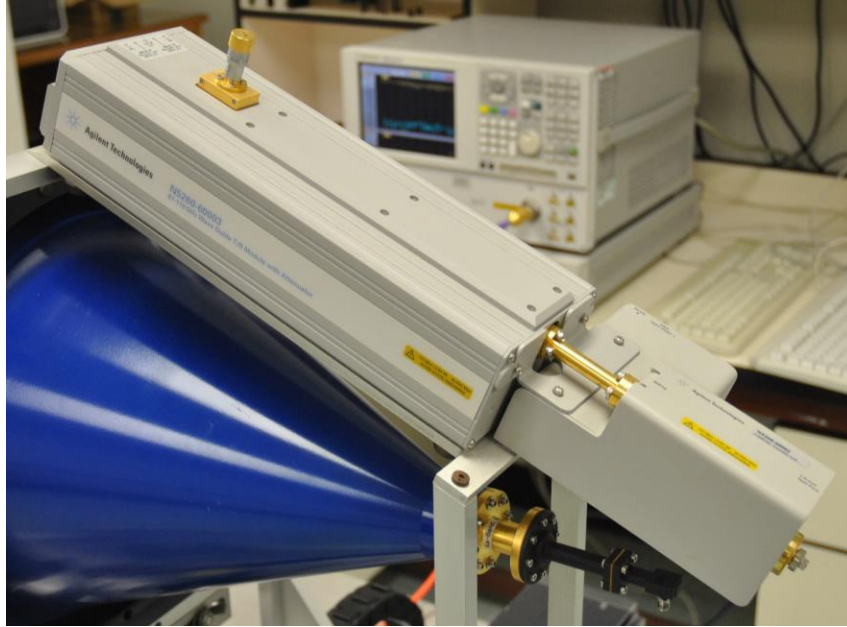
Figure II.4. N5260 67-110 GHz Wave Guide T/R Module.

Figure II.5. Air dielectric cables.

connected to the millimeter head controller, and the controller is automatically disabled when not in use.

Between 50 GHz and 67 GHz, the T/R modules act as a pass-through to connect the network analyzer to the higher-frequency coaxial transitions which possess a 1.00 mm connector. While their internal frequency source is inactive through this frequency range, the T/R modules must still be connected to the millimeter head controller for measurements in this frequency range.

Motor Controller and Servo Motors

The free-space system uses a total of 9 servo motors to accurately position the antennas and sample holder. These are Parker BE232FJ-NFLN servo motors which are connected to two

motion controllers inside the motor controller housing. The motion controllers are produced by Galil, model numbers DMC2142 and DMC2162. The motor controller housing is shown below in Figure II.6.

Figure II.6. Motor controller housing.

Each motor connects to the motion controller with a circular 4-pin power connector and a DA-15 connector for data. The motion controllers connect to the free-space system's computer via Ethernet with a standard RJ45 cat5 connector. The motors can be immediately stopped at any time by turning off the orange power switch on the motor controller housing.

Horn Lens Antennas

The free-space system uses a matching pair of conical horn antennas to send and receive microwave radiation through a material sample. One antenna is shown below in Figure II.7. The antennas are believed to be Series 857 Spot-Focusing Horn Lens Antennas manufactured by the now defunct Alpha Industries, Inc. of Woburn, MA.

Each of the antennas has a spot-focusing lens assembly consisting of two equal plano-convex dielectric lenses mounted back to back at the aperture of a horn antenna [32]. They focus
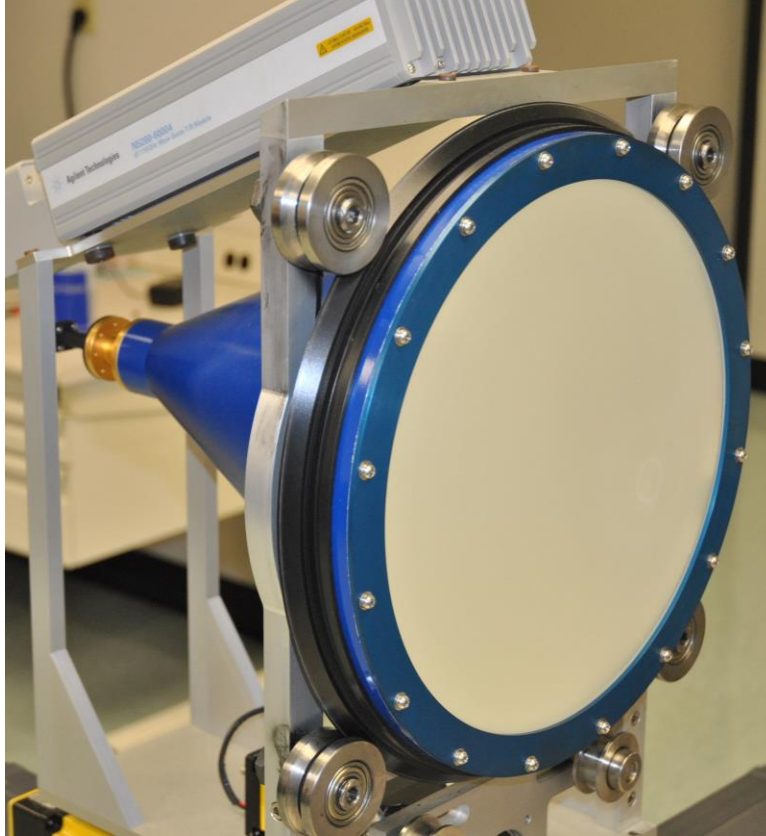
Figure II.7. Conical horn antenna with dielectric lens.

the microwave beam such that at the beam's focus, the -3 dB footprint is approximately one wavelength [36] with minimal phase variation across the footprint [32], thus approximating the plane-wave condition needed for material characterization[40]. The depth of focus of the antennas is approximately 10 wavelengths, and the focal point is located in front of the lens at a distance equal to the diameter of the lens. The antennas are linearly polarized [77]. The polarization was determined experimentally. Details of this are presented in the section V *Appendix A: Antenna Polarization Measurements*.

Coaxial Transitions

Broad-band measurements with the system are accomplished using several pairs of coaxial transitions. Each transition is an assembly consisting of a coaxial cable to rectangular waveguide transition, followed by a rectangular waveguide to circular waveguide transition and flange. This

flange connects to the back end of each of the horn-lens antennas. The flanges have protective caps and the coaxial adapters have protective covers when not in use, included in the figures below.

A total of 6 pairs of coaxial transitions are used with the broad-band horn-lens antennas. These frequency ranges have been selected such that only the TE_{10} dominant mode is excited within the rectangular waveguide portion of the antenna. This has been verified by two means: measuring the inside dimension of the rectangular waveguide portion, which determines the cutoff frequency of each possible mode; and by exciting the transition with the network analyzer and measuring the frequency response of the transition.

The Ku-band transitions have an operating frequency from 12.4 GHz to 18.0 GHz. They have a 3.5 mm coaxial connector, and thus require a 3.5 mm coaxial to 1.85 mm coaxial adapter to connect to the E8361A network analyzer. The transitions, including the coaxial adapters, are shown below in Figure II.8.

Figure II.8. Ku-band transitions with 3.5 mm to 1.85 mm coaxial adapters.

The K-band transitions have an operating frequency from 18.0 GHz to 26.5 GHz. They have a 1.85 mm coaxial connector, used to connect the transition to the network analyzer. The transitions are shown below in Figure II.9.

Figure II.9. K-band transitions with 1.85 mm coaxial connectors.

The Ka-band transitions have an operating frequency from 26.5 GHz to 40.0 GHz. They

have a 1.85 mm coaxial connector, used to connect the transition to the network analyzer. The

transitions are shown below in Figure II.10.

Figure II.10. Ka-band transitions with 1.85 mm coaxial connectors.

The B-band transitions have an operating frequency from 33.0 GHz to 50.0 GHz. They have a 1.85 mm coaxial connector, used to connect the transition to the network analyzer. A circular flange connects the coaxial transition to the remainder of the assembly, though the waveguide inside it is still rectangular. The transitions are shown below in Figure II.11.

Figure II.11. B-band transitions with 1.85 mm coaxial connectors.

The V-band transitions have an operating frequency from 50.0 GHz to 75.0 GHz. They have a 1.00 mm coaxial connector, used to connect the transition to the T/R modules. The 1.00 mm coaxial cable is used for this connection. A circular flange connects the coaxial transition to the remainder of the assembly, though the waveguide inside it is still rectangular. The transitions and the 1.00 mm cable are shown below in Figure II.12.

The W-band transitions have an operating frequency from 75.0 GHz to 110.0 GHz. They have a 1.00 mm coaxial connector, used to connect the transition to the T/R modules. The 1.00 mm coaxial cable is used for this connection. A circular flange connects the coaxial transition to the remainder of the assembly, though the waveguide inside it is still rectangular. The transitions and the 1.00 mm cable are shown below in Figure II.13.

Figure II.12. V-band transitions with 1.00 mm coaxial connectors and 1.00 mm coaxial cable.

Figure II.13. W-band transitions with 1.00 mm coaxial connectors and 1.00 mm coaxial cable.

Transition Measurements

To verify that only the dominant TE_{10} mode is excited in the rectangular waveguide portion of the coaxial transitions, two methods were used. The rectangular cross-section of the inside dimension of the waveguide was measured for each coaxial transition, and the cutoff frequencies for the modes of waveguides were calculated. The code is included in the section VI *Appendix B: MATLAB Codes*, *4. Waveguide cutoff frequencies calculator*. The results of these calculations are

shown below in Figure II.14 and Figure II.15. These results show that the TE_{10} mode begins below

the designated region of operation, shown in blue, and that the next dominant mode (TE01 or

TE20) begins after the designated region of operation.
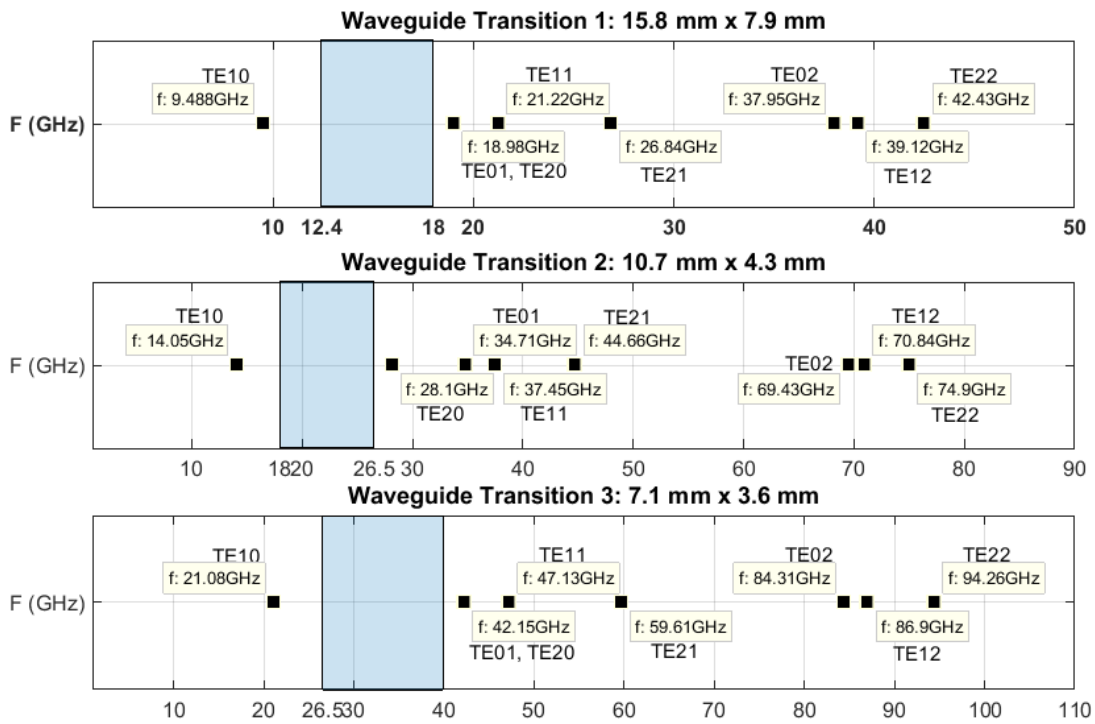
Figure II.14. Calculated waveguide mode cutoff frequencies for Ku-, K- and Ka-band transitions.

Additionally, three pairs of the coaxial transitions were measured using the network

analyzer. Their frequency response is shown below in Figure II.16, Figure II.17 and Figure II.18.

These results show that the -10 dB bandwidth for the measured transitions covers the specified

frequency range for each transition. This provided additional verification that the TE10 mode was

being excited in the rectangular waveguide portion of each tested coaxial transition.
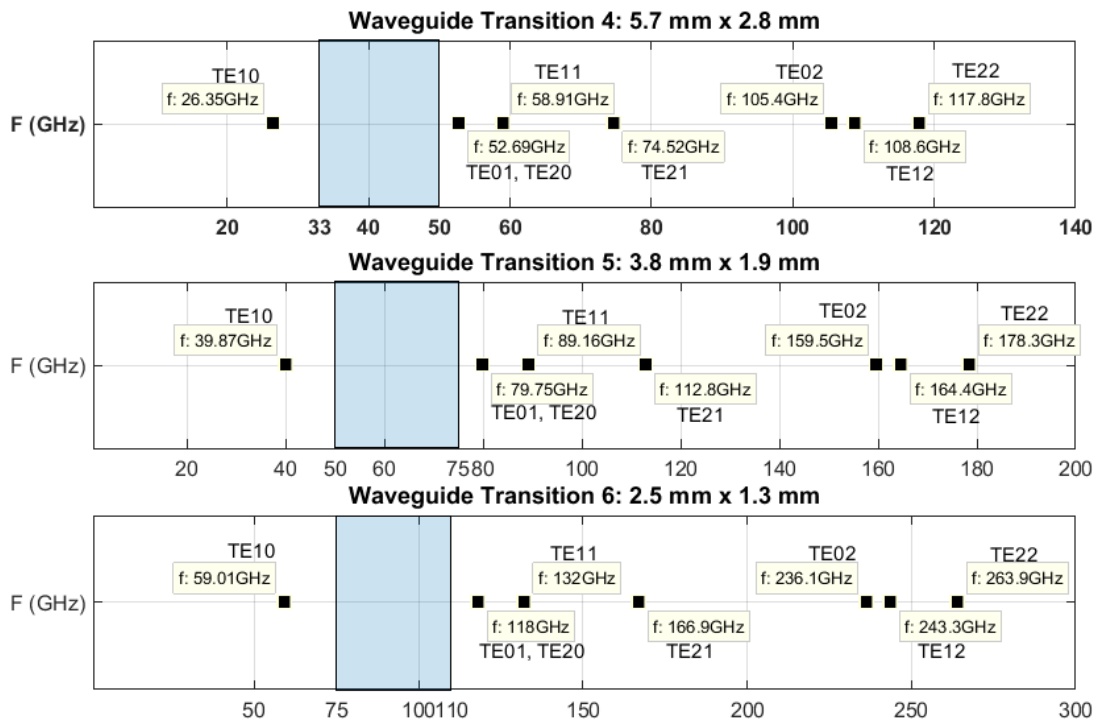
Figure II.15. Calculated waveguide mode cutoff frequencies for B-, V- and W-band transitions.
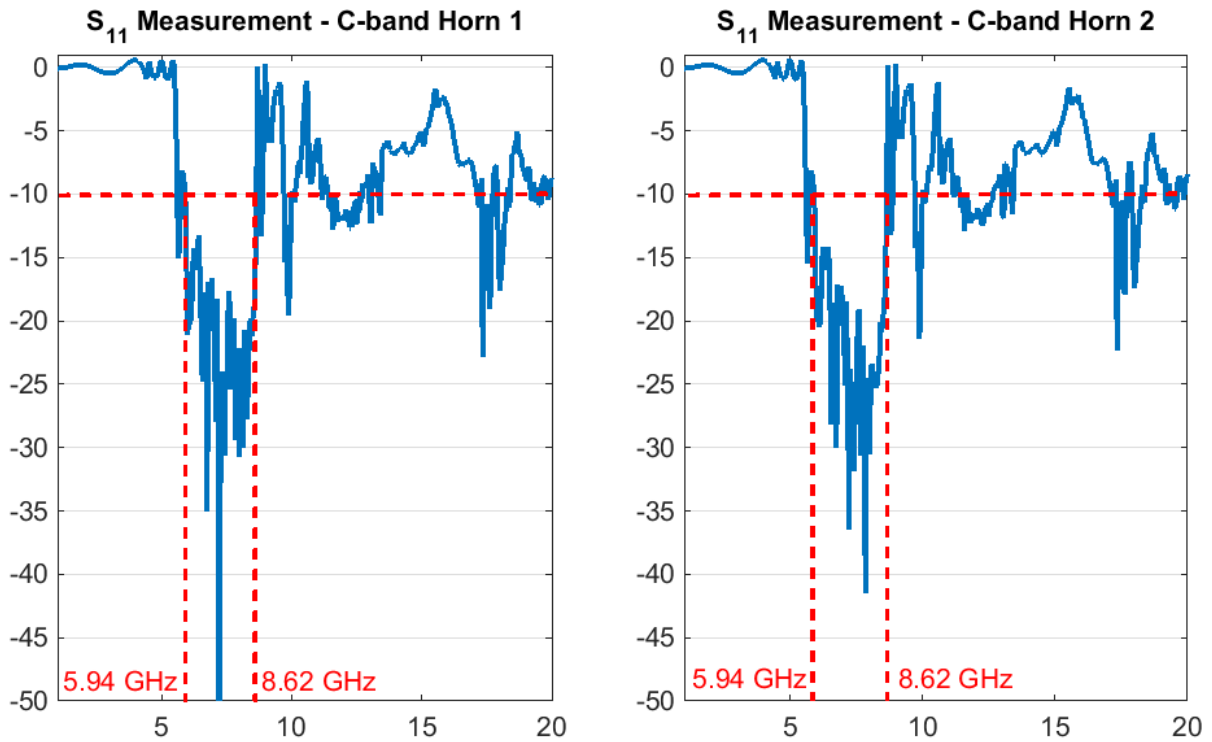
Figure II.16. Measured frequency response of C-band coaxial transition.
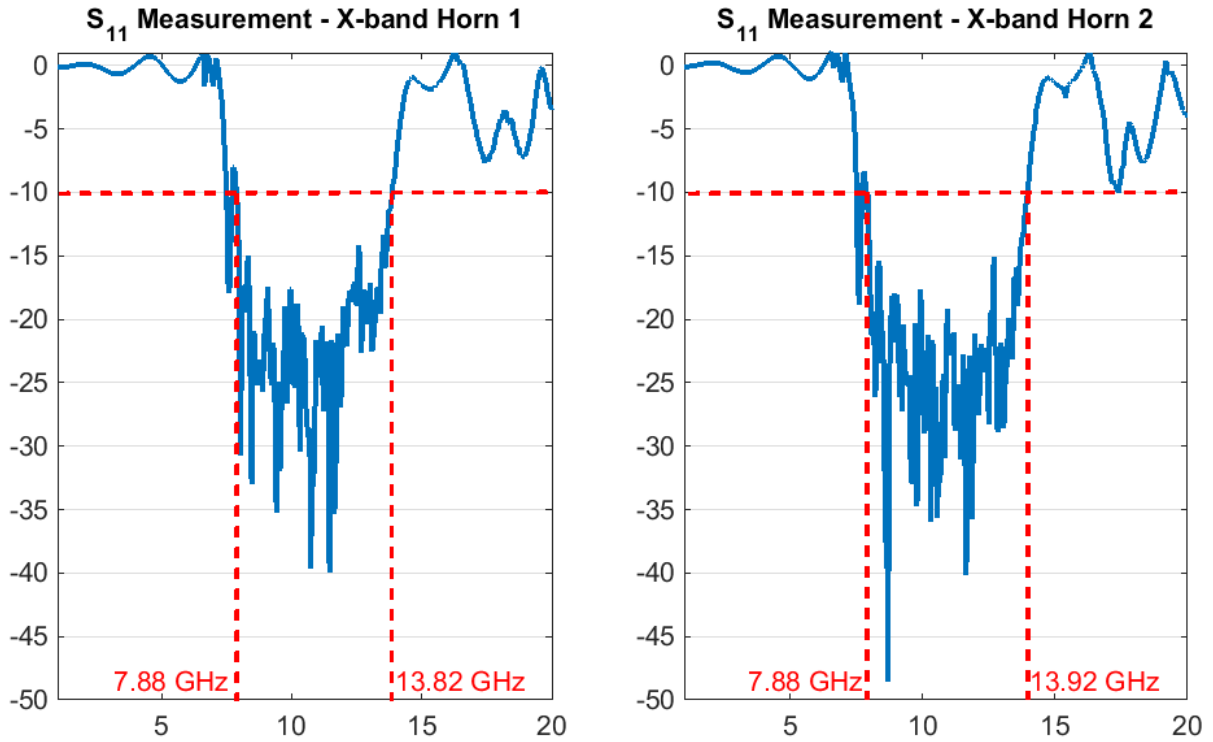
Figure II.17. Measured frequency response of X-band coaxial transition.
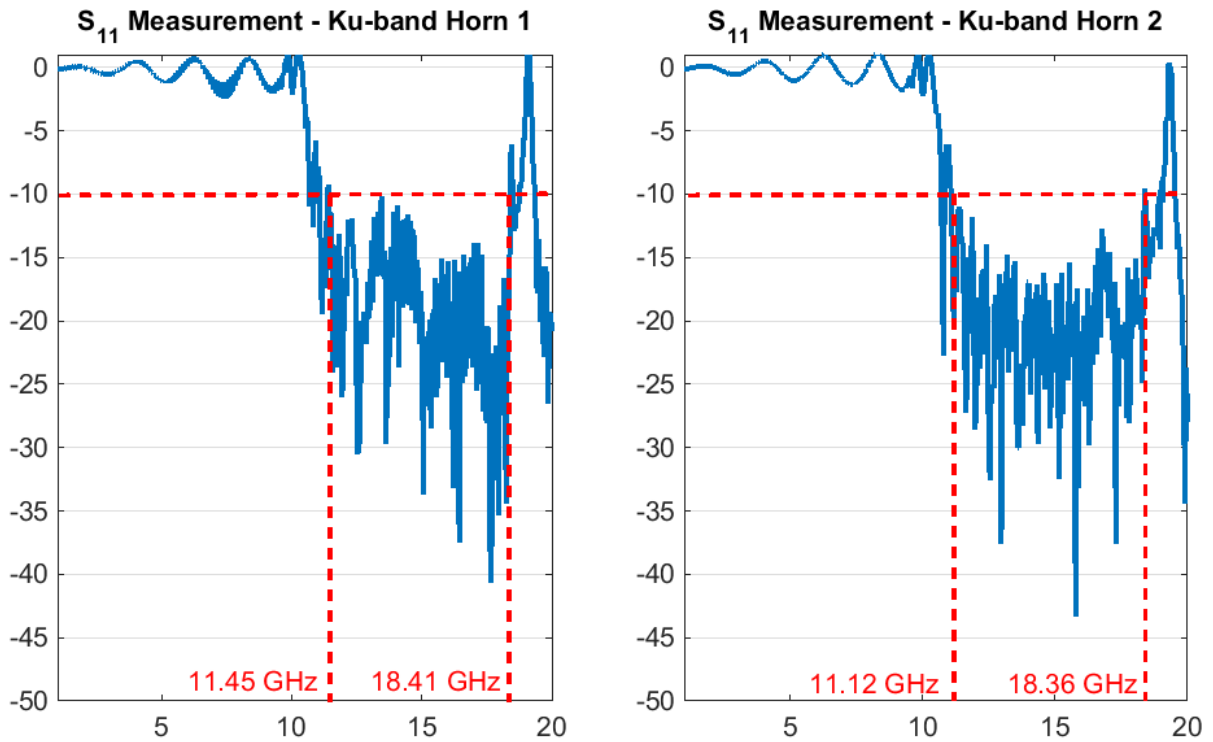
Figure II.18. Measured frequency response of Ku-band coaxial transition.

Additional Horn Lens Antennas

Two additional pairs of horn-lens antennas are included with the system, designed for measurements from 5.8 GHz to 8.2 GHz (C band) and from 8.2 GHz to 12.4 GHz (X band). They have a larger rear flange connector and are permanently connected to their respective coaxial transitions. These are otherwise identical to the main broadband pairs of horn-lens antennas. The antennas are shown below in Figure II.19.

Figure II.19. C-band and X-band horn lens antennas.

Sample Holder

The sample holder for the free-space system consists of an assembly of several thick acrylic sheets. The sheets hold a sample under test between the two horn-lens antennas, such that the focal point of the port 1 antenna is at the front face of the sample and the focal point of the port 2 antenna is at the back face of the sample. Nylon bolts are used to secure the sample inside the

holder, and to secure the sample holder to the table. The sample holder can be moved up and down by the Y-axis motor, allowing for scanning of samples along the Y axis.
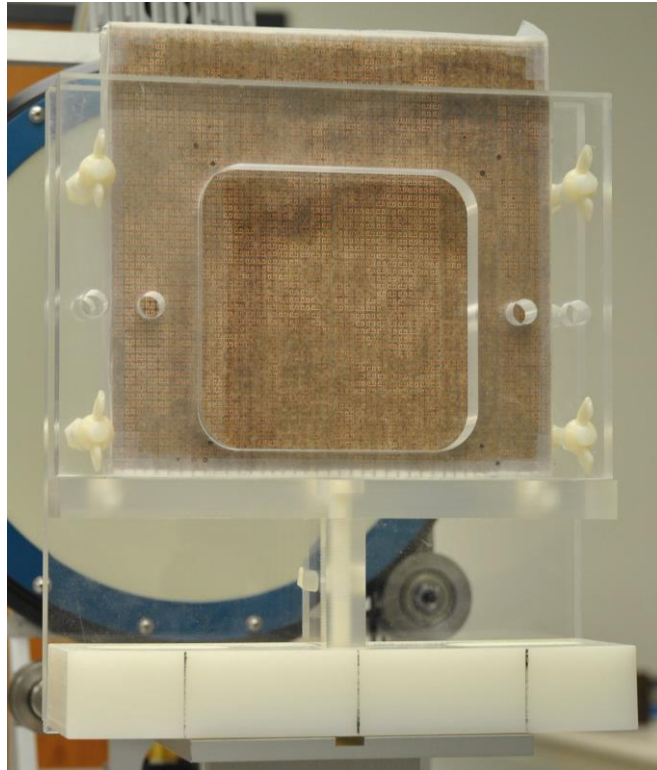
Figure II.20. Free-space sample holder with metamaterial sample between acrylic sheets.

Controller Computer

The controller computer for the free-space system is a standard Dell PC running Windows XP. The computer has a secondary Ethernet controller, used to connect the PC to the motor controller housing. The computer also has a GPIB interface card, used to connect the PC to the network analyzer. A closed-source, proprietary piece of software was developed to control the motors of the free-space system and the attached network analyzer. However, the motion controllers and network analyzer could be controlled similarly with other software, such as National Instruments LabView. This would allow for advanced automated measurements and interactive debugging of the system when needed.

Upon startup, the position of the motors is not known to the software. The positioners must be initialized before measurements can be performed. This is accomplished by choosing *Initialize Positioners* from the *Positioners* menu. Once selected, the software determines the position of the motors by returning them to their home coordinates. All cables connecting the free-space system to the network analyzer must be disconnected for this process. Significant damage to the free-space system components can occur if this is not done. If the software is closed or crashes, this process must be repeated in full.

B.   Calibration of the System

Calibration of the system is accomplished through the Through-Reflect-Line calibration technique [32]. Calibration must be performed before measurements can be taken with the system. Calibration may also need to be repeated if environmental conditions change or if much time has passed since the last calibration. The need for this can be determined though the process detailed in the beginning of the section II.E *Validation of System Performance*.

The Through-Reflect-Line calibration technique requires a reflective short-circuit calibration standard. The reflective plate included with the free-space system is shown below in Figure II.21.

Figure II.21. Gold-plated reflective plate used for TRL calibration.

Calibration is started by selecting *TRL Calibration* from the *PNA/NWA* menu. The user is prompted for the desired frequency band to be measured, as shown below in Figure II.22. A custom frequency band may be entered, if a subset of one of the frequency bands is to be measured.

The user is then prompted for the number of points. This determines the number of discrete frequency steps between the minimum and maximum frequencies to be measured. This is shown below in Figure II.23.
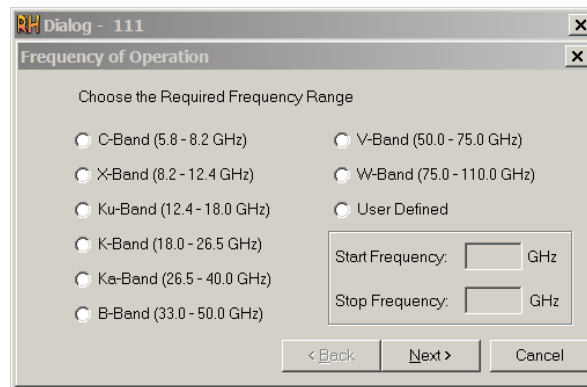
Figure II.22. Free-space software dialog for frequency range.
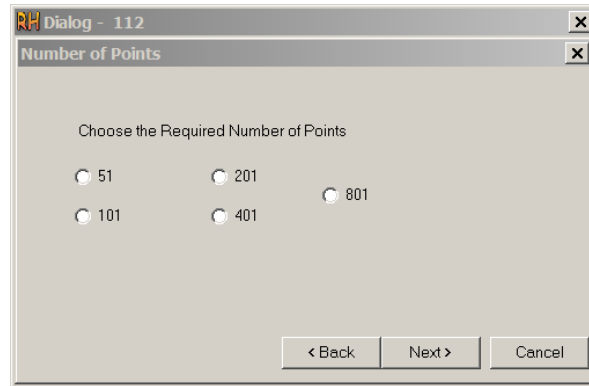
Figure II.23. Free-space software dialog for number of points.

The user is then prompted for the averaging factor for measurements. This is shown below in Figure II.24. The averaging factor determines the number of times each discrete frequency point is sampled before moving to the next frequency point. These samples are then averaged together to produce the data which is returned by the network analyzer. A higher number results in greater immunity to random error, at the expense of increased measurement time.
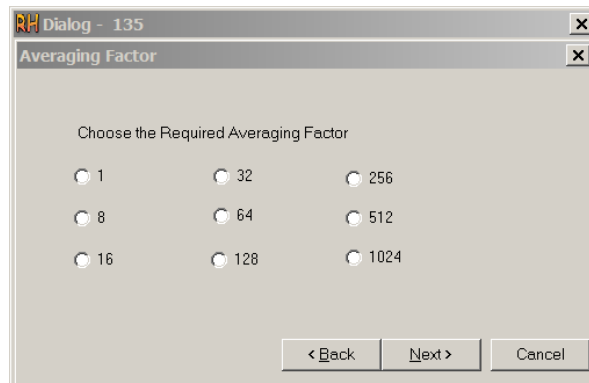
Figure II.24. Free-space software dialog for averaging factor.

The user is finally prompted for options pertaining to the TRL calibration. This is shown below in Figure II.25. The *Thru* option is used for transmission measurements, and the *Reflect* option is used for reflection measurements, where the sample under test is backed by the reflective plate.

59
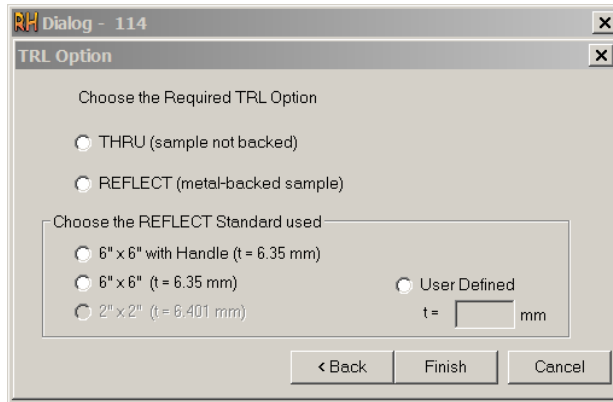
Figure II.25. Free-space software dialog for TRL options.

After selecting *Finish*, the user is then prompted to measure the Thru, Reflect and Line standards. The order in which these are measured is determined by the user's choice in the TRL Option dialog.

Measurement of the Thru standard is achieved by emptying the sample holder. This is illustrated below in Figure II.26. After selecting *OK*, the port 2 antenna is moved by the software so that its focus overlaps with the focus of the port 1 antenna.
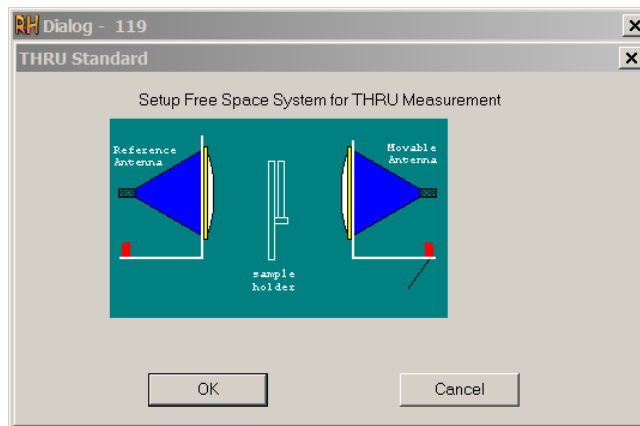
Figure II.26. Free-space software dialog for Thru standard measurement.

Measurement of the Reflect standard is achieved by placing the reflective plate in the sample holder. This is illustrated below in Figure II.27 and demonstrated in Figure II.28. After selecting *OK*, the port 2 antenna is moved by the software so that its focus is at the back surface of the reflective plate.

60
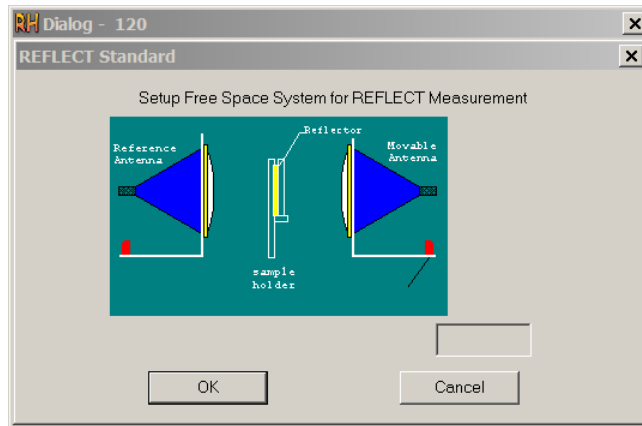
Figure II.27. Free-space software dialog for Reflect standard measurement.
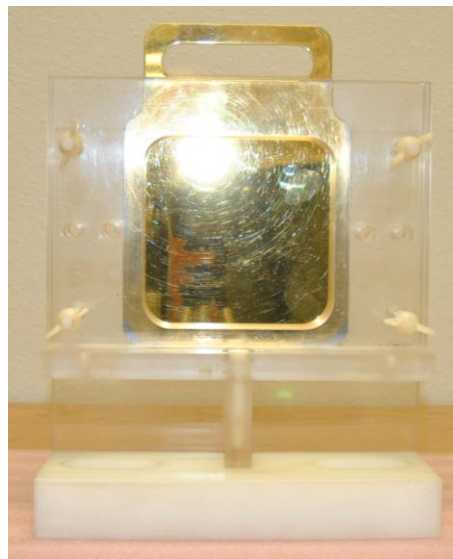
Figure II.28. Gold-plated reflective plate mounted in sample holder.

Measurement of the Line standard is achieved by emptying the sample holder. This is illustrated below in Figure II.29. After selecting *OK*, the port 2 antenna is moved by the software so that its focus is a quarter-wavelength at mid-band from the focus of the port 1 antenna.
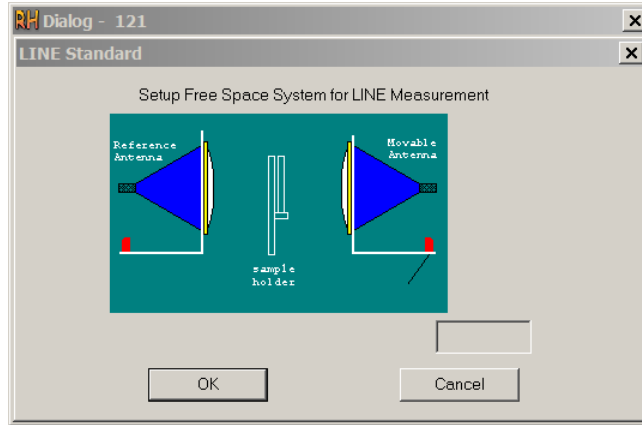
Figure II.29. Free-space software dialog for Line standard measurement.

After measuring the Thru, Reflect and Line standards, the user is prompted to repeat any measurements if desired before saving and verifying the calibration.
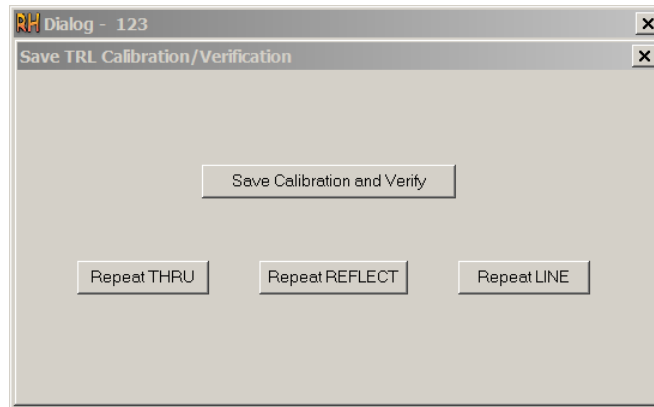
Figure II.30. Free-space software dialog for saving and verifying calibration.

After selecting *Save Calibration and Verify*, the user is prompted to repeat measurement of two of the calibration standards. The software then reports if the calibration was successful.

C. Measurements Using the System

Once the free-space system has been calibrated, measurements of a sample may be performed. Transmission-mode measurements are enabled by selecting *Thru* from the TRL Options dialog, and reflection-mode measurements are enabled by selecting *Reflect* from the TRL Options dialog, as shown above in Figure II.25.

Measurements are started by selecting *Make Measurement* from the *PNA/NWA* menu. The user is then presented with the measurement dialog, shown below in Figure II.31.
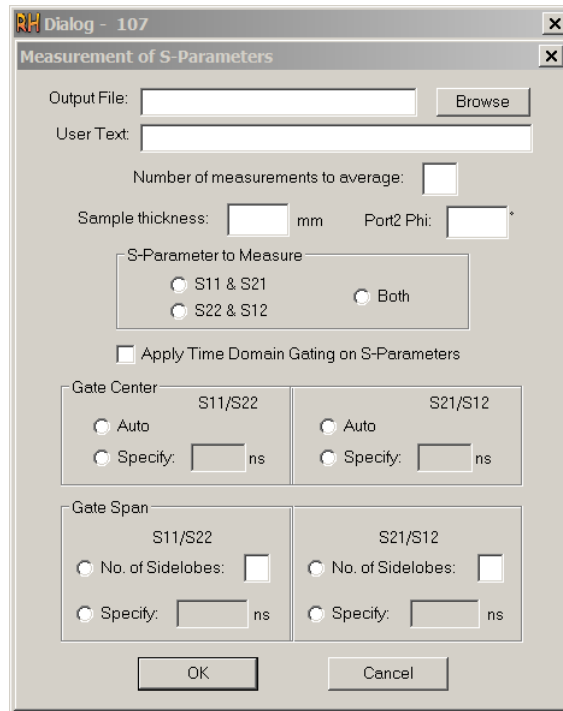
Figure II.31. Free-space software dialog for measurements.

The user selects an output file to store the measured data. This file may be read by the *5. Import_Real_Imag_*HVS code located in Appendix D. The *User Text* field adds a note to the stored measurement data. The user must specify the sample thickness, in mm. This determines the position to which the port 2 antenna is moved by the software prior to measurement.

Transmission-mode Measurements

Transmission-mode measurements are performed by placing the sample under test directly in the sample holder, then tightening its nylon bolts so that the sample is held securely in place. The user can select *S11 & S21*, *S22 & S12* or *Both* from the measurements dialog.

Reflection-mode Measurements

Reflection-mode measurements are performed by placing the sample under test along with the reflective plate in the sample holder, with the plate facing the port 2 antenna. The nylon bolts

are then tightened so that the sample and the reflective plate are held together securely in the sample holder. The user should select *S11 & S21* from the measurements dialog.

Polarization

The *Port 2 Phi* option determines the rotation of the port 2 antenna. A choice of 0° leaves the port 2 antenna vertically polarized, co-polarized with respect to the port 1 antenna. A choice of 90° leaves the port 2 antenna horizontally polarized, cross-polarized with respect to the port 1 antenna.

Time-domain Gating

Time-domain gating is enabled by selecting *Apply Time Domain Gating on S-Parameters* from the measurement dialog. The four fields below allow the user to select the gate center and gate span for reflection (*S11/S22*) and transmission (*S21/S12*) measurements. Choosing *Auto* for the gate center causes the network analyzer to select the maximum amplitude in the time-domain transformed signal as the center of the gate. The default number of side-lobes is 2, which usually captures the main reflections off the front and back faces of the sample. This may not produce the expected correct result for inhomogeneous samples, or in the event that a sample with a $\lambda / 2$ resonance is measured. In these cases, the gate center and span may be manually specified.

Raster Scanning

The free-space system is capable of performing raster-scanning at normal or oblique incidence, allowing for an object to be scanned by the system [32]. These scans can then be processed further and assembled into a bitmap image. To explore this capability, a test target was created using Ansys HFSS, shown in Figure II.32 below. The total design size is 150 mm by 150 mm. The largest feature on the design measures 20 mm by 4 mm, and the smallest feature

measures 9 mm by 1.8 mm. The design was then fabricated with the Electrical Engineering department's CNC mill, with the final result shown in Figure II.33 below.

An initial scan was performed at normal incidence, with a 3 mm step size. The reflection S11 and transmission S21 scan results are shown in Figure II.34 below. The scan was then repeated with a 1 mm step size for a smaller region of the test pattern, indicated by the dashed line in Figure II.35 below. The results of this scan are show in Figure II.36 and Figure II.37 below. These preliminary scan results do not show additional detail at smaller step sizes. It is believed that this is due to diffraction effects around the boundaries of the copper features. Diffraction effects have been noted to be a source of error in previous works [26] [30] [32]. Future works may consider targets with dielectric material inclusions to avoid these effects.
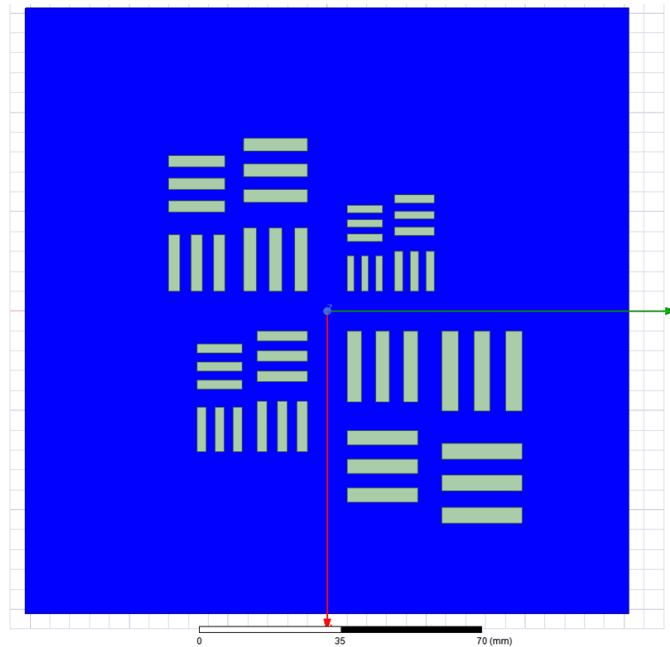
Figure II.32. Test target layout as seen in Ansys HFSS.
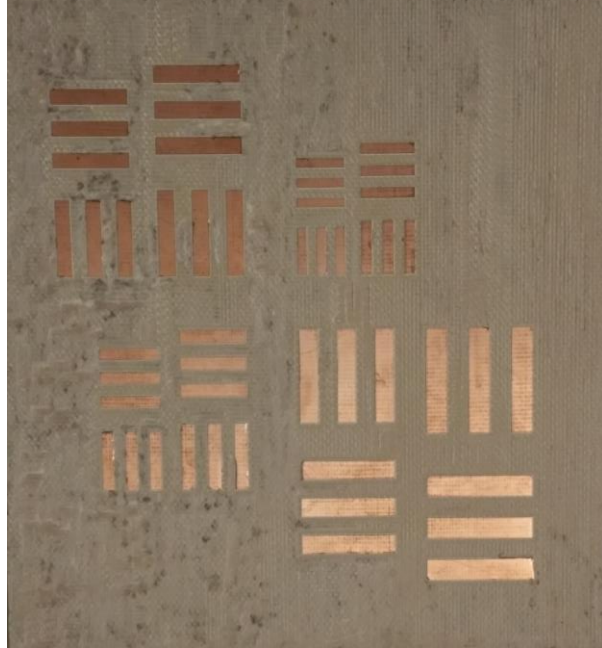
Figure II.33. Test target as milled, copper on FR4 substrate.
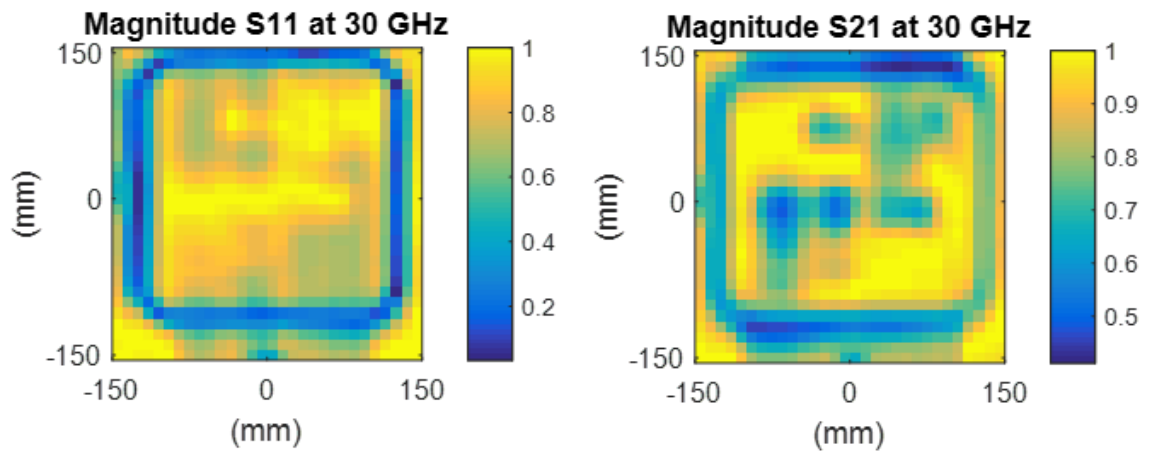
Figure II.34. Raster scan of test target, 3 mm step size.
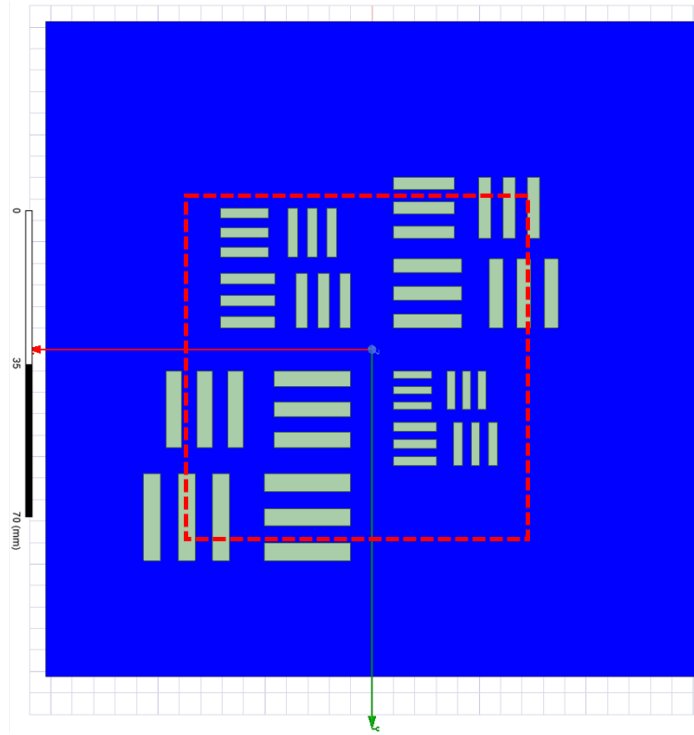
Figure II.35. Test target with zoomed region indicated (red dashed line).
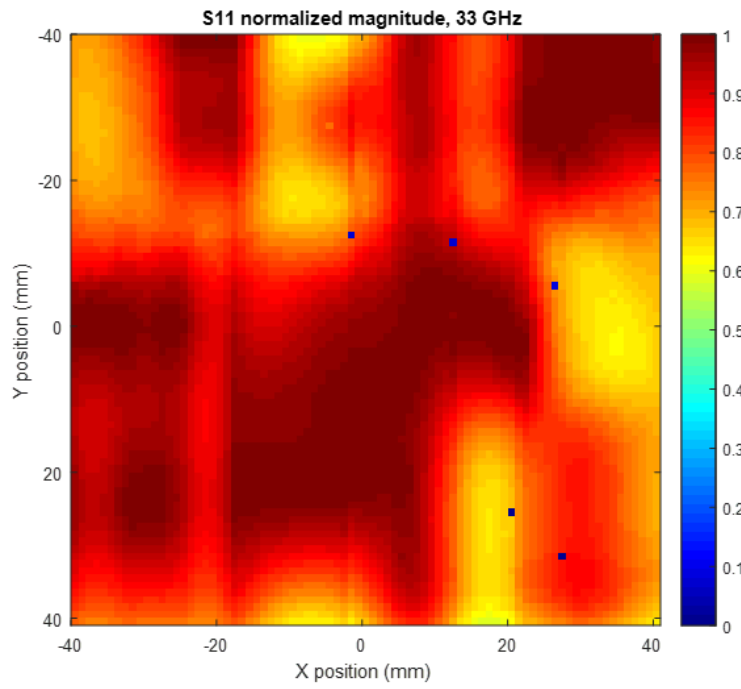
Figure II.36. Raster scan of test target, reflection, 1 mm step size.
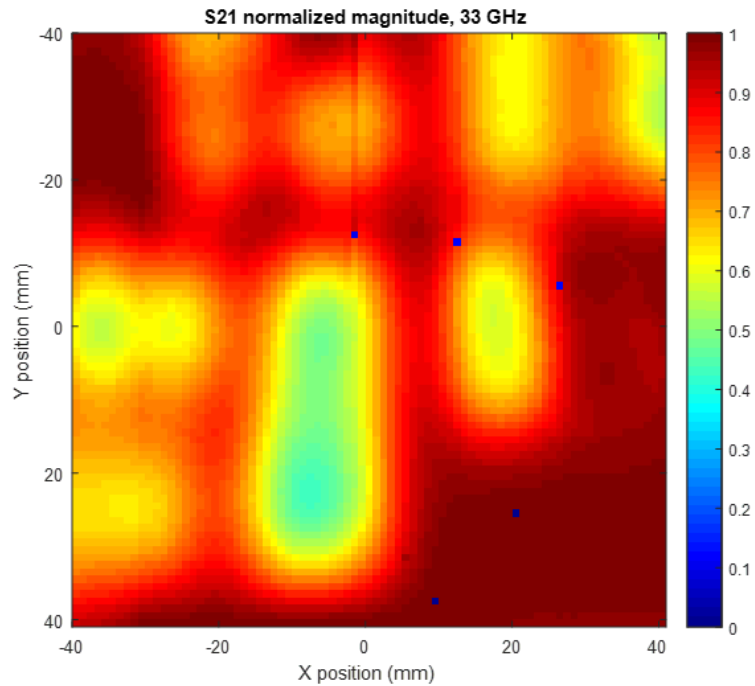
Figure II.37. Raster scan of test target, transmission, 1 mm step size.

D.   Extraction of Permittivity and Permeability

Several methods extracting the permittivity and permeability of a sample under test are available. The most commonly employed methods used with free-space measurements are presented here.

Nicolson-Ross-Weir Method

The Nicolson-Ross-Weir (NRW) method of extraction of material properties is a well-known technique which has been used in published research [54] [78] [79]. The method was originally developed by A. M. Nicolson and G. F. Ross and presented in their work, *Measurement of the Intrinsic Properties of Materials by Time-Domain Techniques* in 1970 [44]. The technique was adapted for use with the modern network analyzer by W. B. Weir and presented in the work, *Automatic Measurement of Complex Dielectric Constant and Permeability at Microwave Frequencies* [45]. A shortcoming of the technique was noticed by T. L. Blakney and presented in

68

the work, *Comments on "Automatic Measurement of Complex Dielectric Constant and Permeability at Microwave Frequencies"* in 1975 [57]. The method as presented by L. Chen, et al. is shown below [54].

The reflection coefficient Γ is given as:

$$\Gamma = K \pm \sqrt{K^2 - 1} \tag{II.1}$$

where K is a term defined as:

$$K = \frac{(S_{11}^2 - S_{21}^2) + 1}{2S_{11}} \tag{II.2}$$

The magnitude reflection coefficient |Γ| is always less than 1, giving the appropriate choice of root. The transmission coefficient T is given as:

$$T = \frac{(S_{11} + S_{21}) - \Gamma}{1 - \Gamma(S_{11} + S_{21})} \tag{II.3}$$

The complex relative permeability and complex relative permittivity of the material are then given by:

$$\mu_r = \frac{1 + \Gamma}{(1 - \Gamma)\Lambda\sqrt{(1/\lambda_0^2) - (1/\lambda_c^2)}} \tag{II.4}$$

$$\varepsilon_r = \frac{\lambda_0^2}{\mu_r[(1/\lambda_c^2) - (1/\Lambda^2)]} \tag{II.5}$$

where λ_0 is the free-space wavelength, λ_c is the cutoff wavelength of the transmission line (which $\lambda_c = \infty$ for TEM transmission lines such as coaxial lines and free-space) and with the $1/\Lambda^2$ term given by:

$$\frac{1}{\Lambda^2} = -[\frac{1}{2\pi d}\ln(\frac{1}{T})]^2 \tag{II.6}$$

where d is the sample thickness in meters.

Two faults are apparent in the NRW method. The last equation has an infinite number of roots, introducing ambiguity for samples whose thickness is greater than a wavelength. This may

be resolved by phase unwrapping or by computing the group delay at two discrete frequency points [54]. Chen, et al. provide details for resolving the ambiguity.

The method also produces anomalous results when the sample thickness is equal to an integer multiple of half of the wavelength inside the medium; this is discussed in further detail in the section I.B *Microwave and Millimeter-wave Measurements*, *Sample Thickness and Loss Tangent Considerations*. In short, as S_{11} approaches zero (-∞ dB), the denominator of the K term approaches zero, and the K term approaches infinity. Several researchers have proposed modified NRW methods that seek to avoid this problem [56] [58] [80].

Ghodgaonkar's Methods

The methods presented by Ghodgaonkar, et al. are used in this work to validate the performance of the free-space system. The author's published results were achieved with the first generation of the free-space system in use at the University of Arkansas.

Reflection

Ghodgaonkar's method of determining complex permittivity from reflection measurements was presented in the work, *A Free-Space Method for Measurement of Dielectric Constants and Loss Tangents at Microwave Frequencies* in 1989 [29]. As a reflection method, only S_{11} is used to determine complex permittivity. The relationship between S_{11} and the material's permittivity is given by Ghodgaonkar, et al. as:

$$S_{11} = \frac{jZ_{dn}\tan(\beta_d d) - 1}{jZ_{dn}\tan(\beta_d d) + 1} \tag{II.7}$$

where Z_{dn} is the normalized wave impedance of the material under test, β_d is the phase constant in the material under test, d is the sample thickness [29].

This method is limited to measuring nonmagnetic materials. The code implementing this method can be found in the section VI *Appendix B: MATLAB Codes*, *2. Iterative algorithm*.

70

Transmission

Ghodgaonkar's method of determining complex permittivity and complex permeability from transmission measurements was presented in the work, *Free-Space Measurement of Complex Permittivity and Complex Permeability of Magnetic Materials at Microwave Frequencies* in 1990 [46]. The relationship between S_{11}, S_{21} and the material's complex relative permittivity ε^* and complex relative permeability μ^* are as follows:

$$S_{11} = \frac{\Gamma(1-T^2)}{1-\Gamma^2 T^2} \tag{II.8}$$

$$S_{21} = \frac{T(1-\Gamma^2)}{1-\Gamma^2 T^2} \tag{II.9}$$

The reflection coefficient Γ and the transmission coefficient T are given by:

$$\Gamma = \frac{Z_{sn}-1}{Z_{sn}+1} \tag{II.10}$$

$$T = e^{-\gamma d} \tag{II.11}$$

where Z_{sn} is the normalized characteristic impedance and γ is the propagation constant of the sample. These are given by:

$$Z_{sn} = \sqrt{\frac{\mu^*}{\varepsilon^*}} \tag{II.12}$$

$$\gamma = \gamma_0 \sqrt{\varepsilon^* \mu^*} \tag{II.13}$$

with γ_0, the propagation constant in free space, given by:

$$\gamma_0 = j2\pi/\lambda_0 \tag{II.14}$$

with λ_0 as the wavelength in free-space. The method then proceeds similarly to the NRW method, with the following:

$$K = \frac{(S_{11}^2 - S_{21}^2)+1}{2S_{11}} \tag{II.15}$$

$$T = \frac{(S_{11}+S_{21})-\Gamma}{1-\Gamma(S_{11}+S_{21})} \tag{II.16}$$

$$\Gamma = K \pm \sqrt{K^2-1} \tag{II.17}$$

71

Finally, the complex relative permittivity ε^* and complex relative permeability μ^* are given by:

$$\varepsilon^* = \frac{\gamma}{\gamma_0}\left(\frac{1-\Gamma}{1+\Gamma}\right) \tag{II.18}$$

$$\mu^* = \frac{\gamma}{\gamma_0}\left(\frac{1+\Gamma}{1-\Gamma}\right) \tag{II.19}$$

Ghodgaonkar suggests resolving the multiple values for γ using the following relationships:

$$T = |T|e^{j\phi} \tag{II.20}$$

$$\gamma = \frac{\left[\ln\left(\frac{1}{|T|}\right)\right]}{d} + j\left[\frac{2\pi n - \phi}{d}\right] \tag{II.21}$$

where $n = 0, \pm 1, \pm 2, \ldots$

The imaginary part of γ, which is β, is given by:

$$\beta = \frac{2\pi}{\lambda_m} \tag{II.22}$$

where λ_m is the wavelength inside the medium, which can be obtained from:

$$\frac{d}{\lambda_m} = n - \frac{\phi}{2\pi} \tag{II.23}$$

If the sample thickness is less than λ_m, then $n = 0$ gives a unique value for ε^* and μ^*. If the sample thickness is greater than λ_m, then measurements on two samples of the same material with different thicknesses each can resolve the ambiguity.

E.   Validation of System Performance

After calibration of the free-space system, testing should be performed to verify that the system has been calibrated successfully. A calibration is considered successful if systematic errors have been effectively removed from measurements. The Through-Reflect-Line calibration method allows for a simple test to be performed after calibration [29]. In this test method, the same calibration standards are measured a second time after the Network Analyzer has computed its correction coefficients and applied them to its internal two-port error model [66].

To validate the accuracy of a Through-Reflect-Line calibration, two standards must be measured across the calibrated frequency range: the Reflect standard, and either the Through or the Line standard [29]. Typically, the Reflect and the Through standards are chosen for verification. These measurements should be performed without the use of time-domain gating.

In the ideal case, the measurement of the Reflect standard will yield a magnitude of 0 dB for the reflection terms S_{11} and S_{22}, and $-\infty$ dB for the transmission terms S_{21} and S_{12} [61]. As the ideal Reflect standard is a perfect short circuit, it has a reflection coefficient Γ of -1, and thus the expected phase shift for the reflection terms S_{11} and S_{22} is 180°. There is no expected phase shift for the transmission terms S_{21} and S_{12} as the magnitude of these terms should be $-\infty$ dB.

Also in the ideal case, the measurement of the Through standard will yield a magnitude of 0 dB for the transmission terms S_{21} and S_{12}, and $-\infty$ dB for the reflection terms S_{11} and S_{22} [61]. As the ideal Through standard has a reflection coefficient Γ of 0, the expected phase shift for the transmission terms S_{21} and S_{12} is 0°. There is no expected phase shift for the reflection terms S_{11} and S_{22} as the magnitude of these terms should be $-\infty$ dB.

The Line standard is typically not chosen for verification as there is uncertainty for the expectation of the amplitude of the transmission terms S_{21} and S_{12} [61]. This is because some amount of attenuation will occur when the free-space system's Port 2 antenna is moved back by λ / 4 at mid-band for the Line standard. The amount of attenuation is dependent on the frequencies covered by the calibration, and environmental factors, particularly humidity. However, the measurement can be used to verify the phase accuracy of the transmission terms S_{21} and S_{12}. A phase shift of 90° at mid-band is expected if a single Line standard is used in calibration.

In practice, there will be some deviation from the ideal expected measurements of the calibration standards and the actual error-corrected measurements. This is primarily due to slight

variations in ambient temperature and humidity. Other sources of error contribute to this drift, such as temperature changes within the Network Analyzer, temperature changes of the attenuators within in the coaxial-to-waveguide transitions, movement of objects near the free-space system resulting in changes in reflected microwaves, movement of cables as the free-space system's antennas are moved, and random error [81]. These deviations should be insignificant immediately after calibration of the system. A repeat measurement of the calibration standards can be performed if some time has passed since the previous calibration, in order to determine if the calibration is still valid.

Verification of the Through-Reflect-Line calibration allows a user of the free-space system to check if calibration has been performed successfully, and if the current calibration is still valid. While this answers the question of whether systematic errors have been corrected for in the measurement system, it does not provide much insight into the sensitivity of measurements performed with the system. Accurate extraction of permittivity and permeability from measurements is highly dependent not only on the elimination of systematic error, but also on the overall sensitivity of the system.

Because the free-space system had been kept in storage for an undetermined period of time and under unknown conditions, the possibility existed that the system had sustained damage due to mis-handling or environmental degradation due to uncontrolled humidity. Any such damage would have adversely affected the sensitivity of the system. Thus, it was critical to validate the performance of the system.

Since the system was custom-built and much of the technical documentation was not available, the only feasible method to verify the sensitivity of the system was to replicate existing research which was performed using the system. By performing a set of measurements and

comparing these against previously published works, these measurements would serve as a benchmark to determine if the system was as sensitive as it was prior to its storage.

Results of Time Domain Gating

Figure II.38 below shows a comparison of measurement and extraction results with and without time-domain gating applied. A quartz plate 6.345 mm thick was measured using the University of Arkansas free-space system. Measurements were performed twice: once without applying time-domain gating, and once with applying time-domain gating. The sample's permittivity and permeability were extracted using the Nicolson-Ross-Weir method (detailed in the section II.D *Extraction of Permittivity and Permeability, Nicolson-Ross-Weir Method*). The expected value of permittivity ε_r for quartz is 3.78, and the expected value of permeability μ_r for quartz is 1, as the material is nonmagnetic [46].
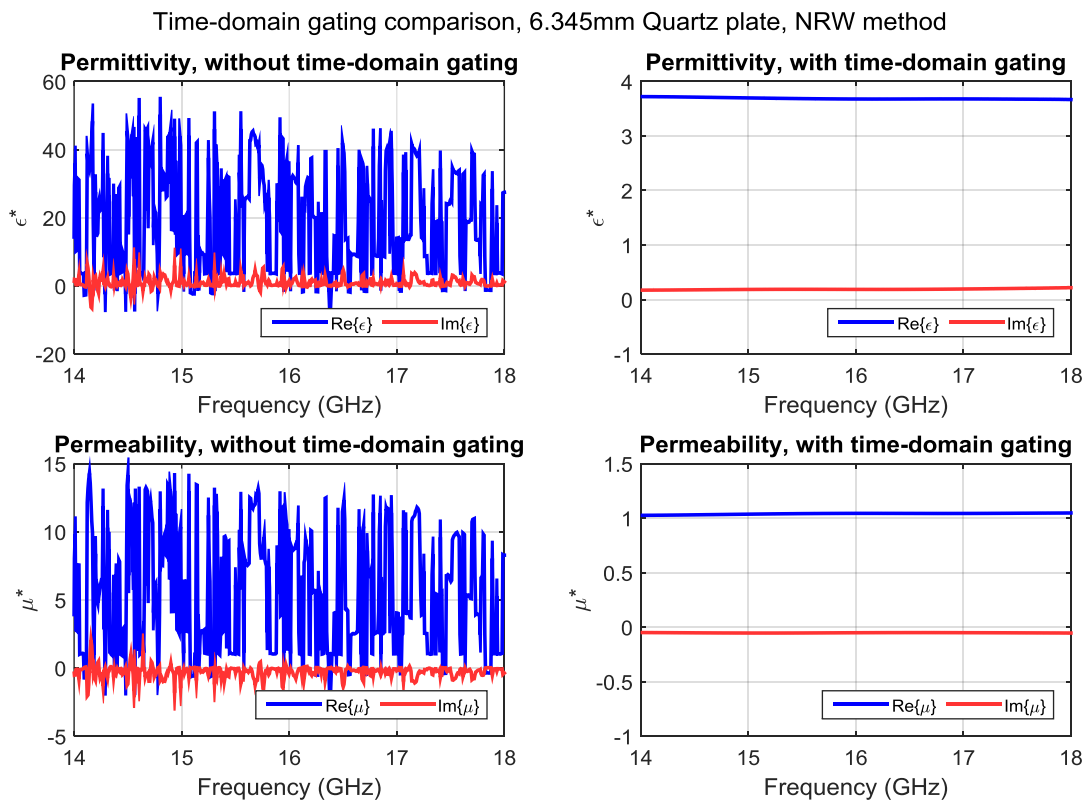

Figure II.38. Comparison of extraction results using time-domain gating.

The results presented in Figure II.38 show a significant difference when time-domain gating is applied to the measurement data. The extracted parameters without time-domain gating show wild variability and do not agree with published data. The extracted parameters with time-domain gating show strong agreement with the expected values, demonstrating that unwanted reflections have been eliminated from the data, resulting in an accurate characterization of the material under test.

A MATLAB implementation of the time-domain gating technique is demonstrated in the section VI *Appendix B: MATLAB Codes*, *3. Time-domain gating algorithm*.

Results of Teflon and Quartz Measurements

The ultimate test to validate the performance of the free-space system is to determine whether the result of published, peer-reviewed literature can be reproduced using the same system. A convenient source of data for this purpose is found in the paper *Microwave Characterization of Dielectric Materials from 8 to 110 GHz using a Free-space Setup* by R. D. Hollinger, et al. published in 2000 before the free-space system was disassembled and moved to the University of Arkansas [36]. This work presents the characterization based on free-space measurements of Teflon, Quartz, and additional materials. The researchers measure a 13.3096 mm thick sample of Teflon and a 6.45 mm thick sample of Quartz with the same free-space system in use today at the University of Arkansas [36]. To validate against this work, a 9.763 mm thick sample of Teflon and a 6.362 mm thick sample of quartz were measured with the free-space system. Measurements were performed using the reflection method, to avoid the issues detailed in the section I.B *Microwave and Millimeter-wave Measurements*, *Sample Thickness and Loss Tangent Considerations*. The reflection iterative solver described in the section II.D *Extraction of Permittivity and Permeability*, *Ghodgaonkar's Methods* and implemented in the section VI

76

Appendix B: MATLAB Codes, *2. Iterative algorithm* was used to extract the samples' permittivity. The data from [36] was digitized using the tool *Engauge Digitizer 6.2* found at http://markummitchell.github.io/engauge-digitizer. These digitized values were then compared against the results extracted from the iterative algorithm. The comparison for quartz is shown in Figure II.39 below, and the comparison for Teflon is shown in Figure II.40 below.

The results of the comparison against published literature for both the quartz and Teflon samples show an error of less than 5% from 12.4 GHz up to 110 GHz. This demonstrates that the free-space system is functioning correctly and that the techniques used with it are valid.
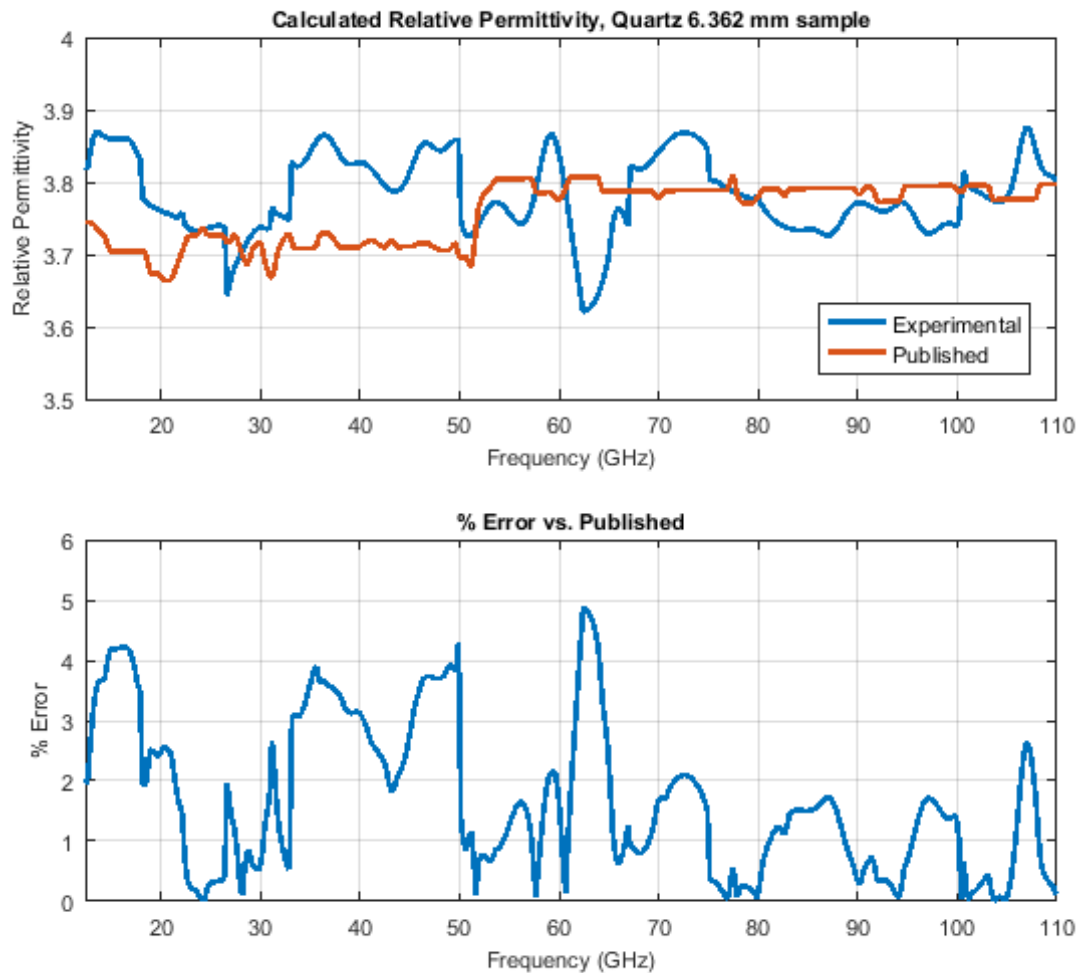
Figure II.39. Experimental results of Quartz characterization, 6.362 mm thick sample.
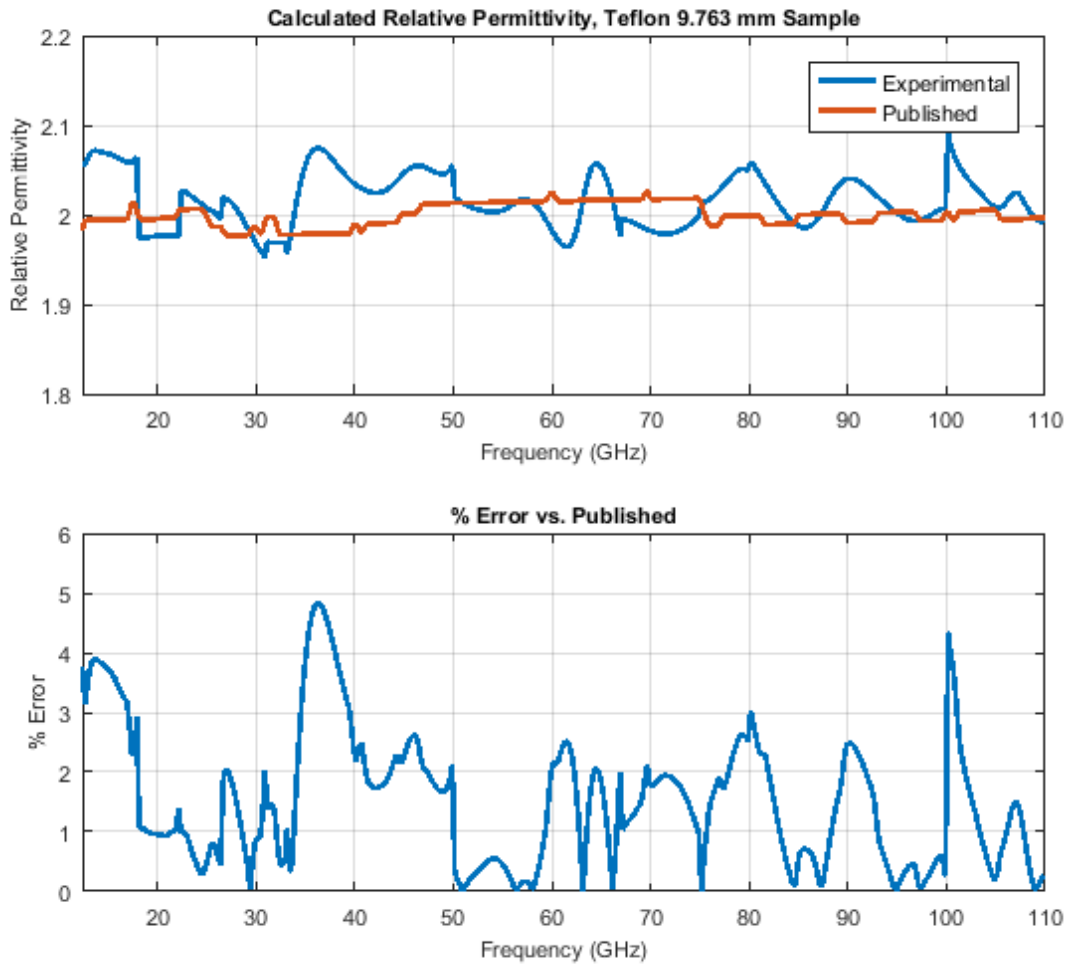
Figure II.40. Experimental results of Teflon characterization, 9.763 mm thick sample.

III. Metamaterial Measurements

A. Description

Metamaterials are a class of materials which exhibit intrinsic properties which differ from those found in nature, particularly in the case of those with a negative permittivity, negative permeability or negative index of refraction [54]. Materials with such properties have been of interest since the early days of microwave measurements [38] [41]. One class of such materials, known as double-negative materials, was proposed by Veselago in 1968 [82]. These materials exhibit apparent effects indicative of negative permittivity and negative permeability, which may allow for novel microwave designs [79]. The University of Arkansas' free-space measurement system has previously been used to characterize such materials successfully [40] [75] [83] [84].

A metamaterial block was provided by the United States Army Research Lab in Adelphi, Maryland for measurement. The metamaterial block consists of a periodic unit cell structure repeating in 3 dimensions. The x- and y-faces of the unit cell consist of a copper structure imprinted upon a thin dielectric sheet, specified as CuFlon, a thin PTFE-based substrate. The 2D structures are shown below in Figure III.1. A capacitively-loaded loop structure is present on the front face of the dielectric, and a cut-wire structure is present on the back face of the dielectric.
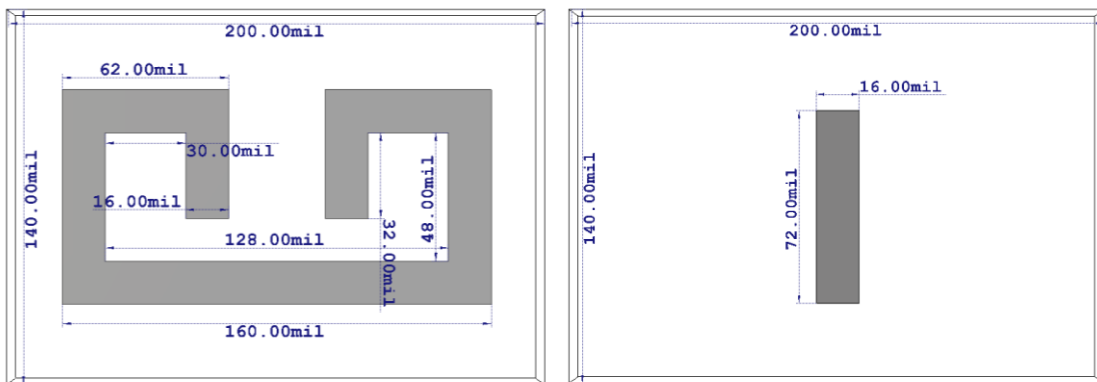

Figure III.1. Front and back views of the metamaterial unit cell.

The 2D structure joins along the z-axis to form a unit cell, shown below in Figure III.2, and the unit cell repeats in each direction.
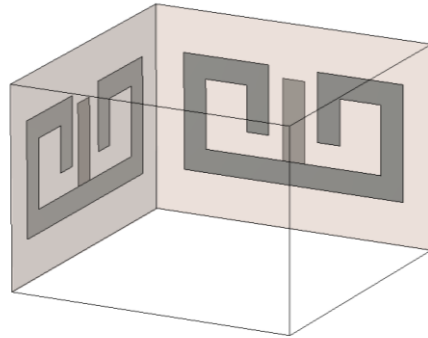
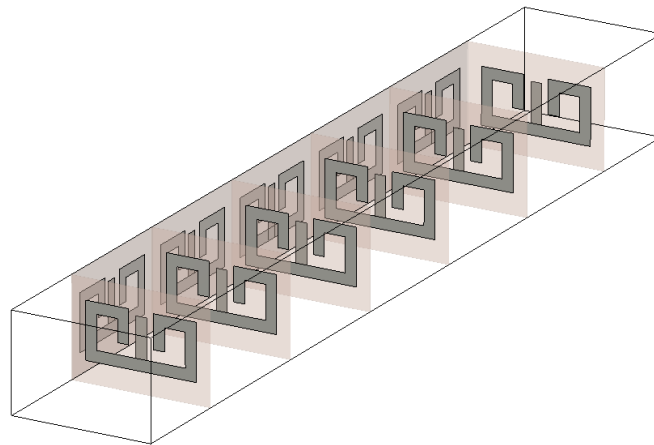Figure III.2. 3D unit cell of the metamaterial block.

Figure III.3. Extension of unit cell to five layers.

B. Simulation of Metamaterial

Simulations of the metamaterial block was executed on the University of Arkansas' High Performance Computing cluster running Ansys HFSS 15. A periodic array was simulated, with the structure repeating infinitely in the x- and y-directions. This infinite array was established by using master/slave boundary conditions. The simulations were meant to approximate the cases seen in orientations 1, the co-polarized case, and 2, the cross-polarized case. In the co-polarized case, the electric field is oriented parallel to the cut-wire structures. In the cross-polarized case, the electric field is oriented normal to the cut-wire structures. Only the dominant propagation modes were considered in the model's Floquet ports; propagating modes that attenuated strongly (more than 100dB loss in the free space between the port and structure) were ignored during mesh refinement. The solution frequency was initially set to 30 GHz, and the second-pass solution frequency was set to the highest resonant frequency found in S_{11}.

C. Measurement of Metamaterial

Procedure

The free-space measurement system was used in conjunction with a HP E8361A microwave network analyzer to perform measurements. A TRL calibration was performed on the system, to counteract the effect of reflections from the apparatus or other sources of error. Averaging was used, with 1,024 samples taken per frequency point. Measurements were done in 3 bands, Ku (12.4 to 18.0 GHz), K (18.0 GHz to 26.5 GHz) and Ka (26.5 to 33.0 GHz). Each band was measured with a matched set of coaxial-to-rectangular-waveguide adapters, which were connected to the feeds of the horn-lens antennas. The single propagating mode in the rectangular portion of the waveguide is TE_{10}, oriented vertically.

Measurements were performed in 2 orientations, shown below. Figure III.4 shows the experimental setup for orientations 1 and 2. The measurements were all performed at normal incidence, such that the wave propagates in the Z direction, normal to the surface of the metamaterial block. The electric field is vertically polarized in each orientation.

Figure III.5 is a photo of the metamaterial block placed inside the sample holder of the free-space system for measurement in orientation 1, the co-polarized case. The system's horn-lens antenna is partially visible behind the sample.

Figure III.6 shows a sketch depicting the orientation 1 of the metamaterial. The sketch is not to scale; it is only to clarify the orientation of the unit cells relative to the free-space system. The wave is propagating in the z-direction (red). The electric field is vertically polarized, parallel to the long axis of the cut wire structure in the unit cell. The unit cell repeats 5 times in the z-direction (as shown). The unit cell also repeats 40 times in the x-direction (green) and 58 times in the y-direction. This repetition is not shown in the sketch in Figure III.6 but can be seen in Figure III.5.

Figure III.7 and Figure III.8 show the metamaterial block in orientation 2, the cross-polarized case. The block has been rotated by 90 degrees in the x-y plane, so that the unit cell repeats 58 times in the x-direction and 40 times in the y-direction. The experimental setup is otherwise unchanged from orientation 1, with the wave propagating in the z-direction. In this case, the cut wire structure is rotated 90 degrees in x-y with regards to the polarization of the electric field, which remains oriented in the y-direction.
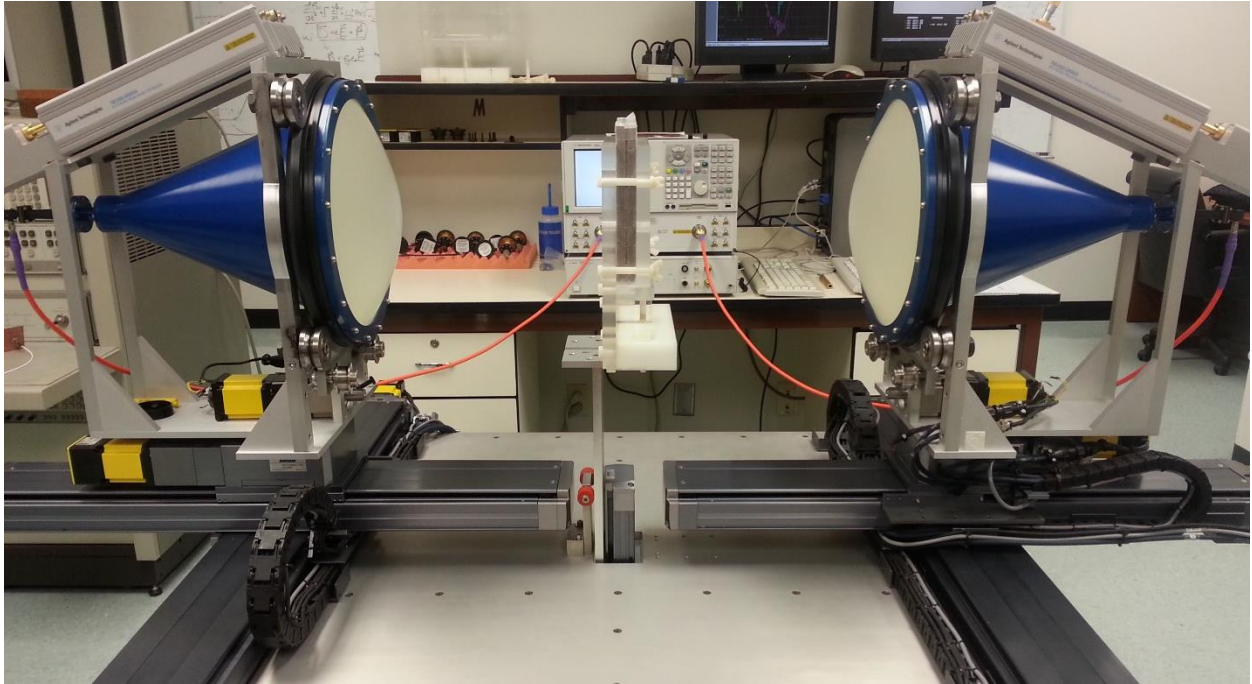
Figure III.4. Experimental setup for measurement of orientations 1 and 2.
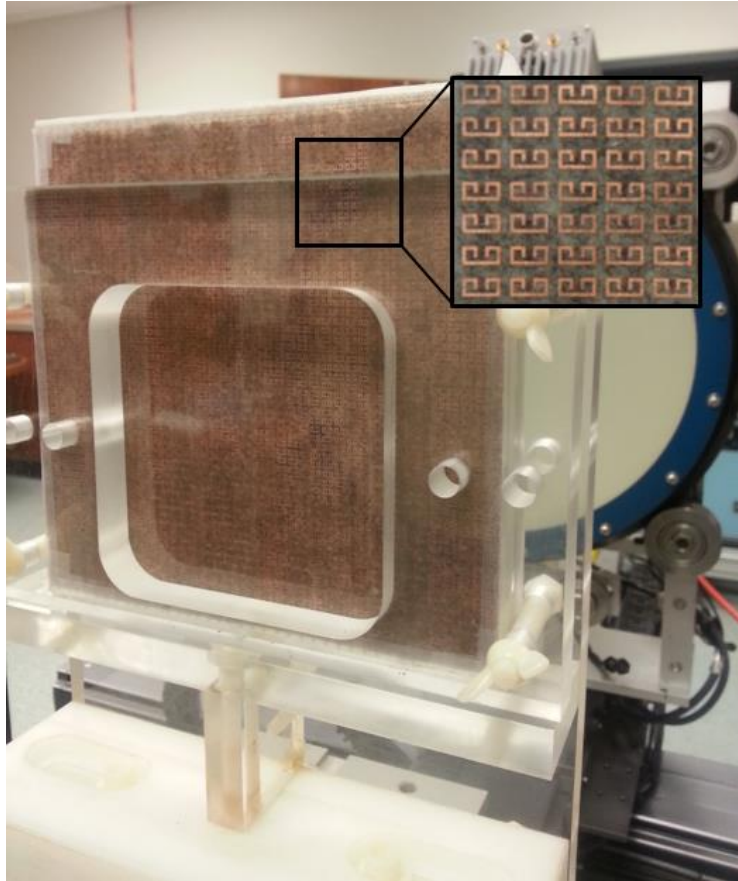
Figure III.5. Metamaterial block in orientation 1 with zoomed inset.
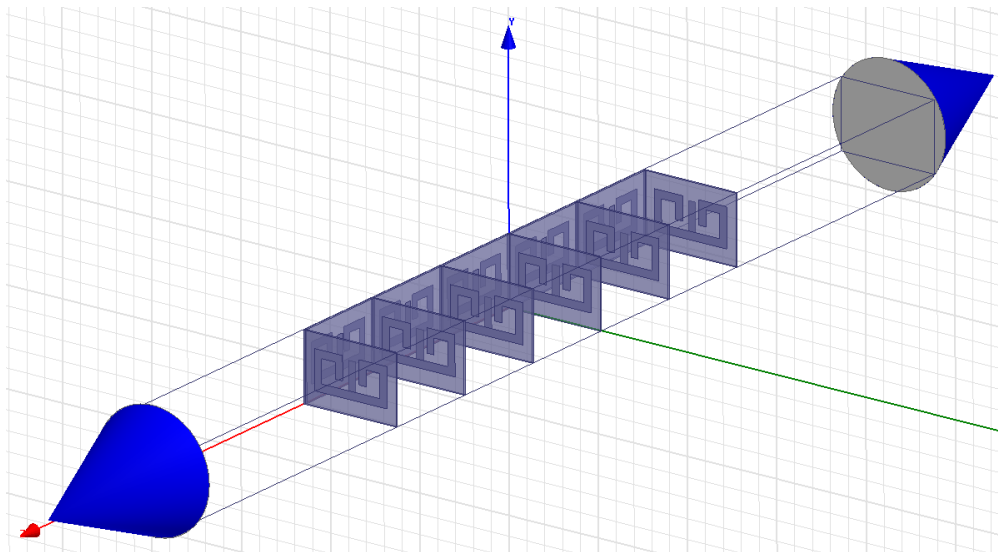
Figure III.6. Sketch of orientation 1.
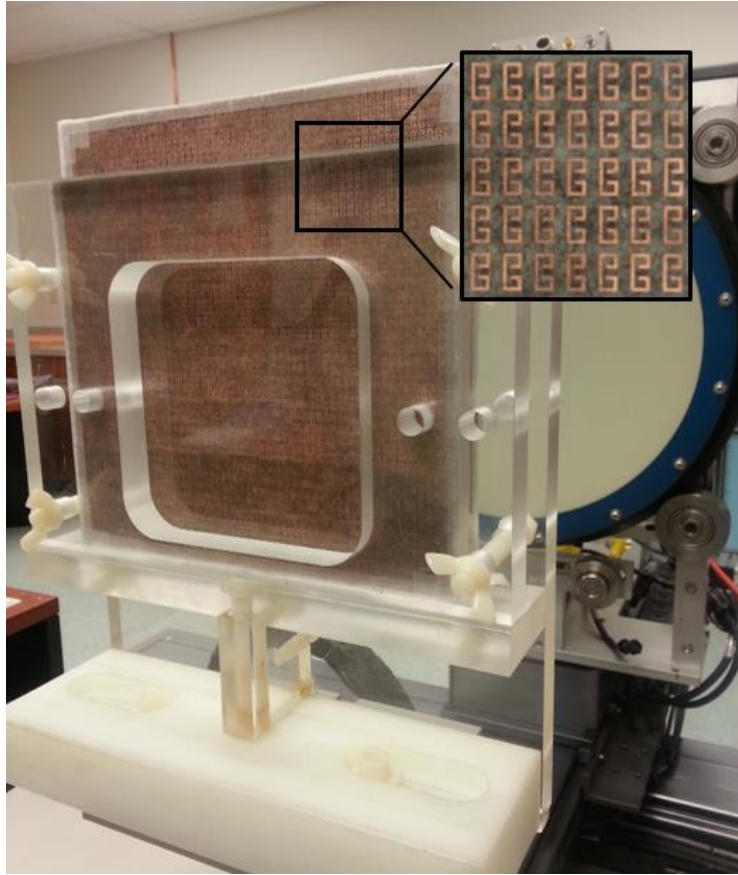
Figure III.7. Metamaterial block in orientation 2 with zoomed inset.
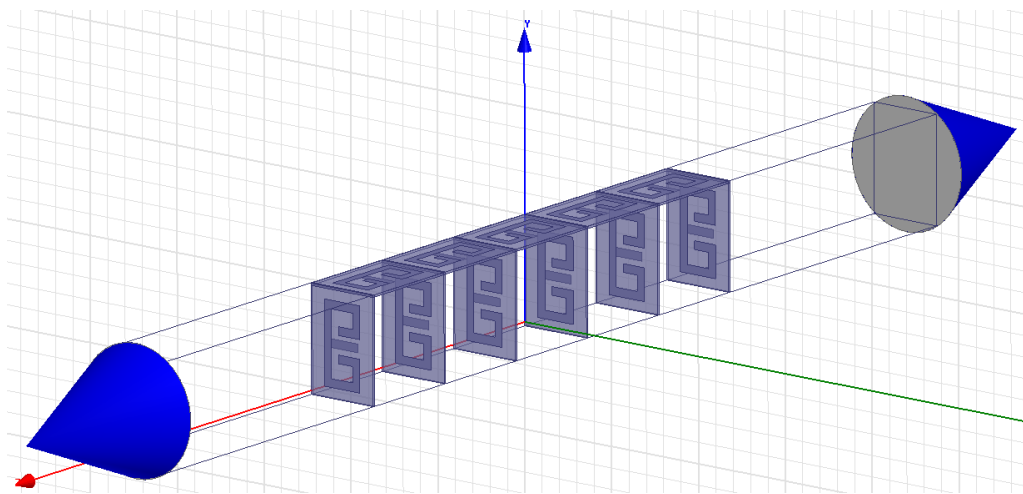
Figure III.8. Sketch of orientation 2.

Results

Figure III.9 and Figure III.10 below show the magnitude and phase S-parameter results for orientation 1 as compared with simulation. Figure III.11 and Figure III.12 below show the magnitude and phase S-parameter results for orientation 2 as compared with simulation. Figure III.13 and Figure III.14 below show the magnitude and phase S-parameter results for orientation 1, with time-domain gating applied to the measured data. Figure III.15 and Figure III.16 below show the magnitude and phase S-parameter results for orientation 2, with time-domain gating applied to the measured data.

A frequency shift in resonant features can be seen between simulation and measurement. It is proposed that this is due to a change with respect to frequency in the dielectric constant of the metamaterial substrate. Ansys HFSS's material library generally assumes a constant permittivity regardless of frequency. For some materials, such as Teflon (PTFE), this is a reasonable assumption to make across a wide range of frequencies.
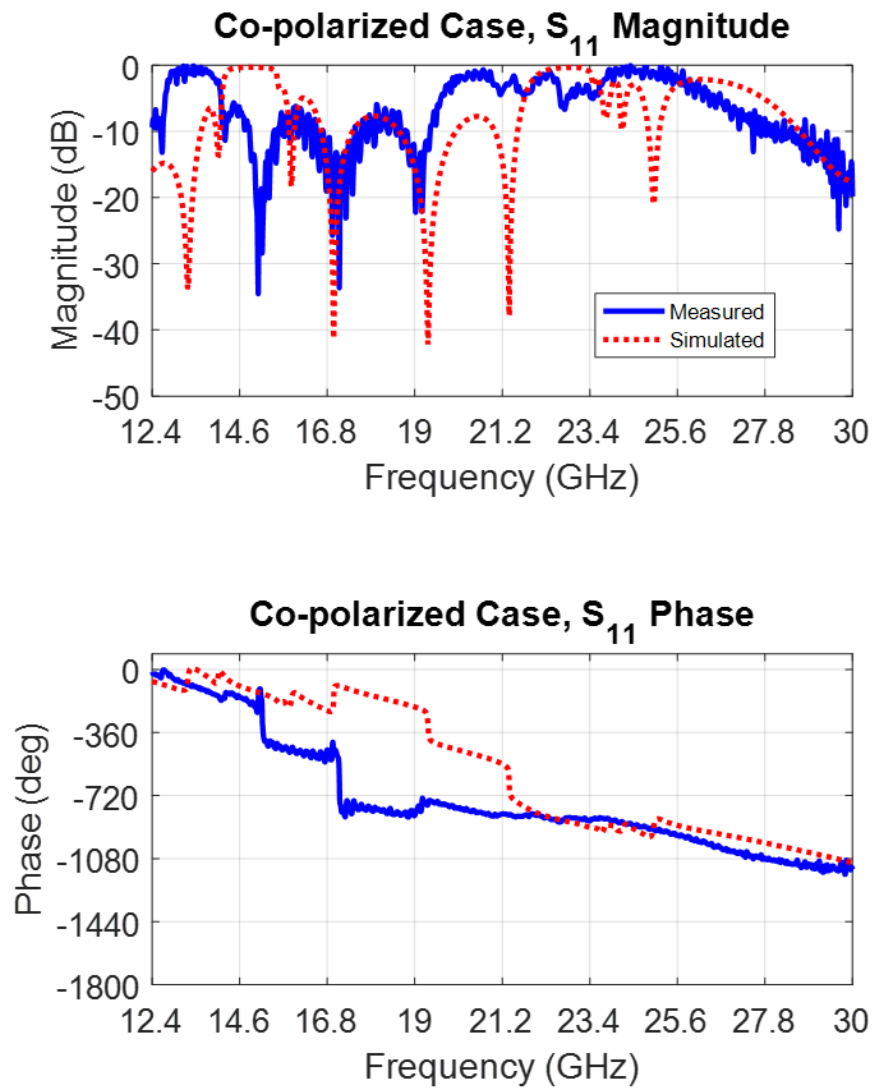
Figure III.9. Simulation and measurement results of S_{11} for orientation 1.
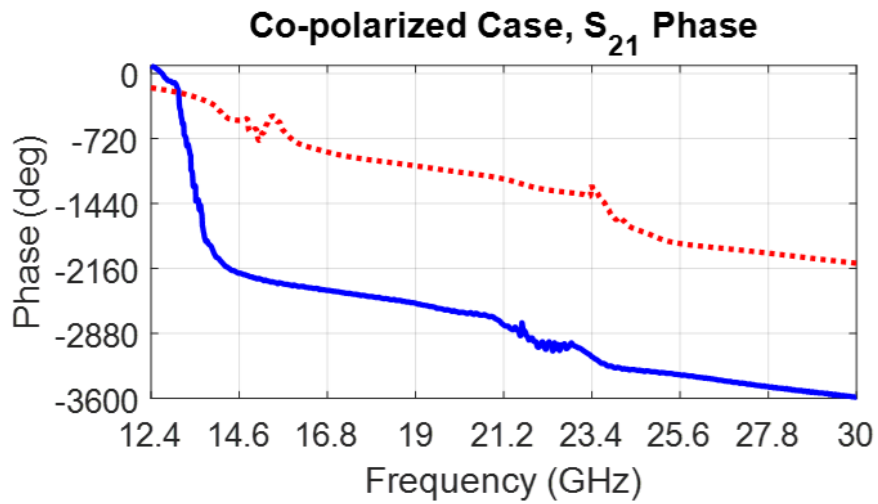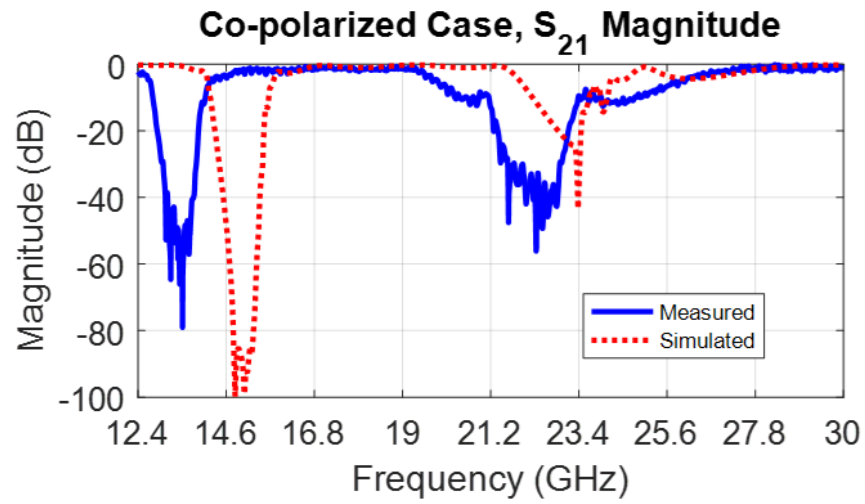
Figure III.10. Simulation and measurement results of S_{21} for orientation 1.
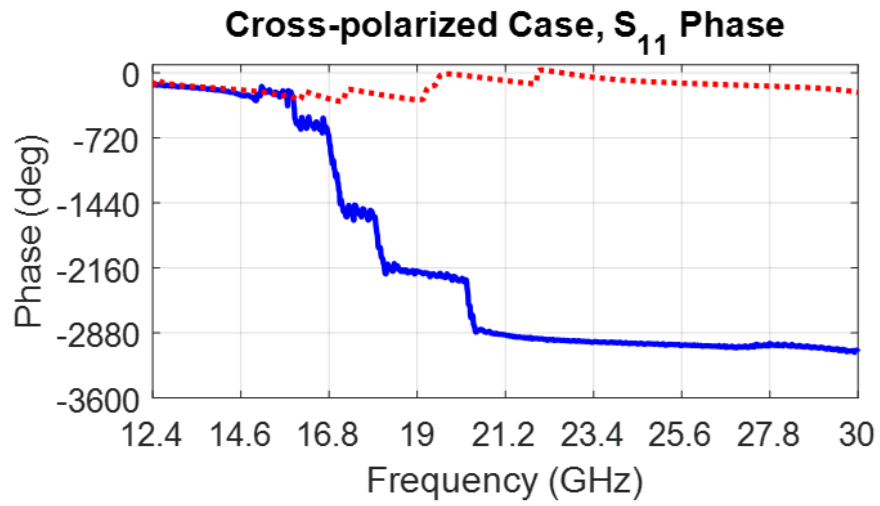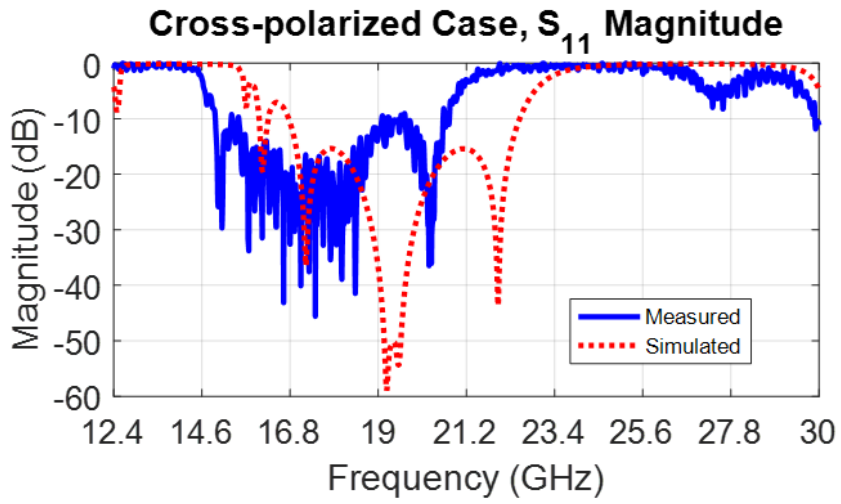
Figure III.11. Simulation and measurement results of S_{11} for orientation 2.
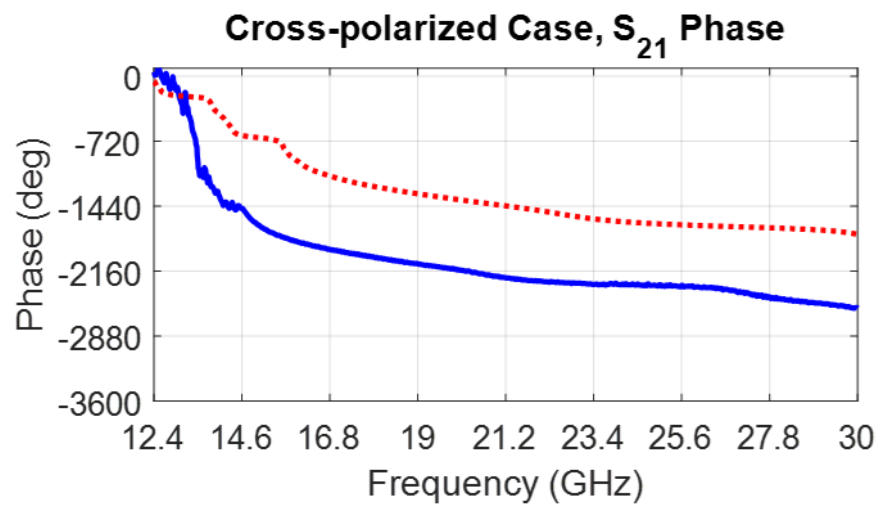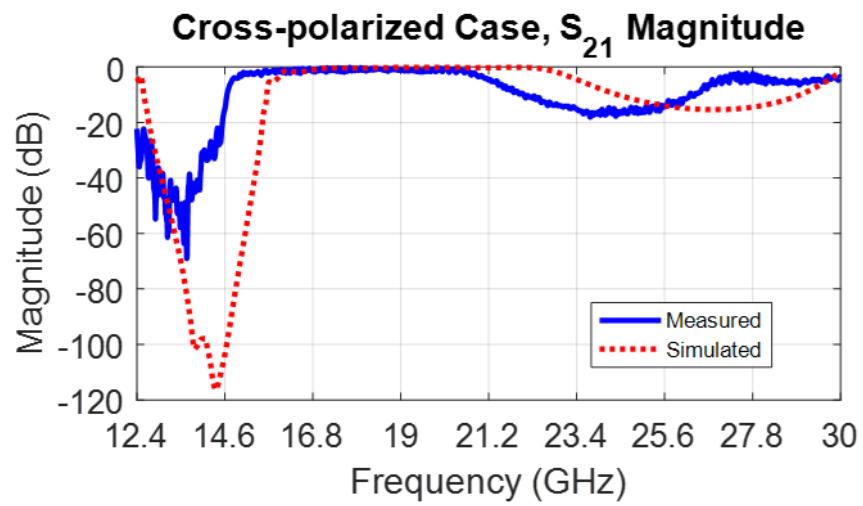
Figure III.12. Simulation and measurement results of S_{21} for orientation 2.
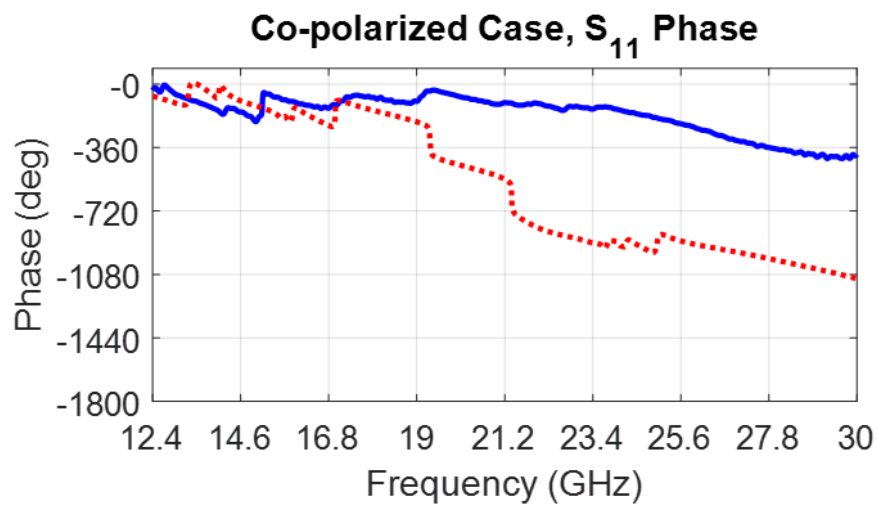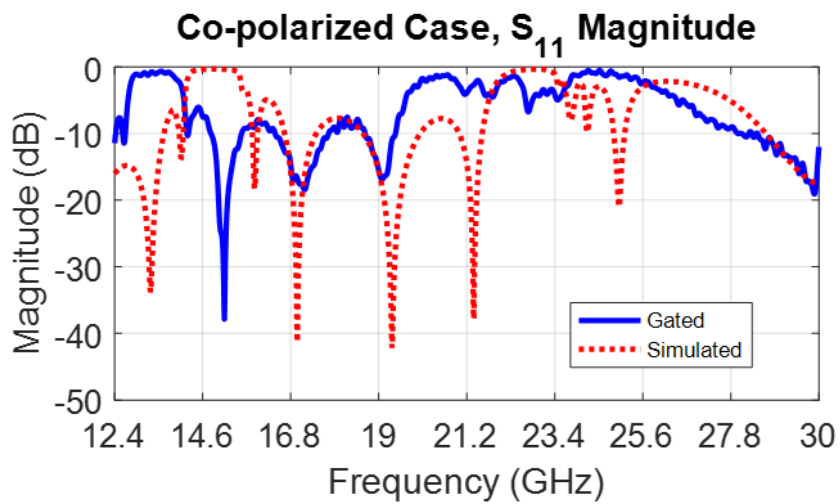
Figure III.13. Simulation and gated measurement results of S_{11} for orientation 1.
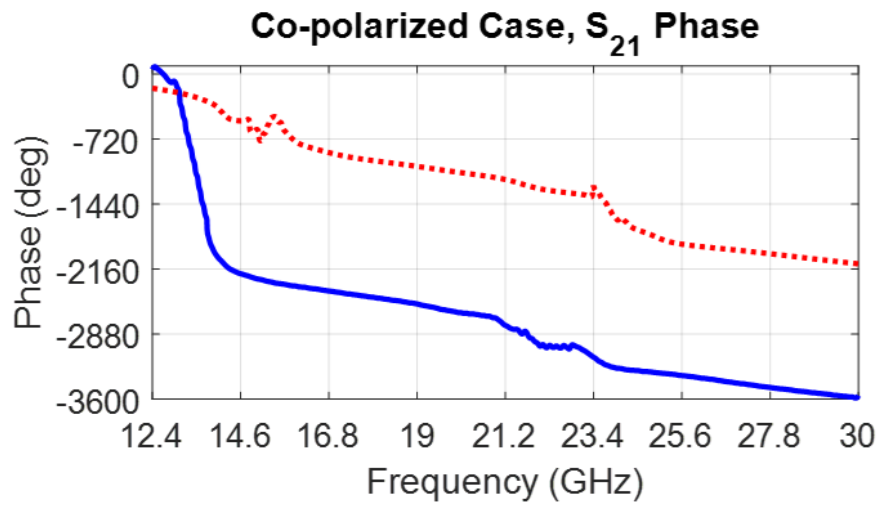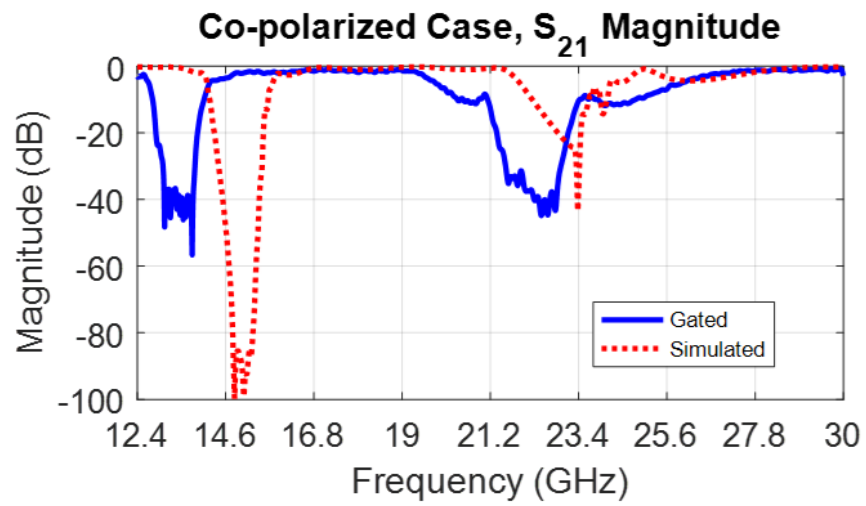
Figure III.14. Simulation and gated measurement results of S_{21} for orientation 1.
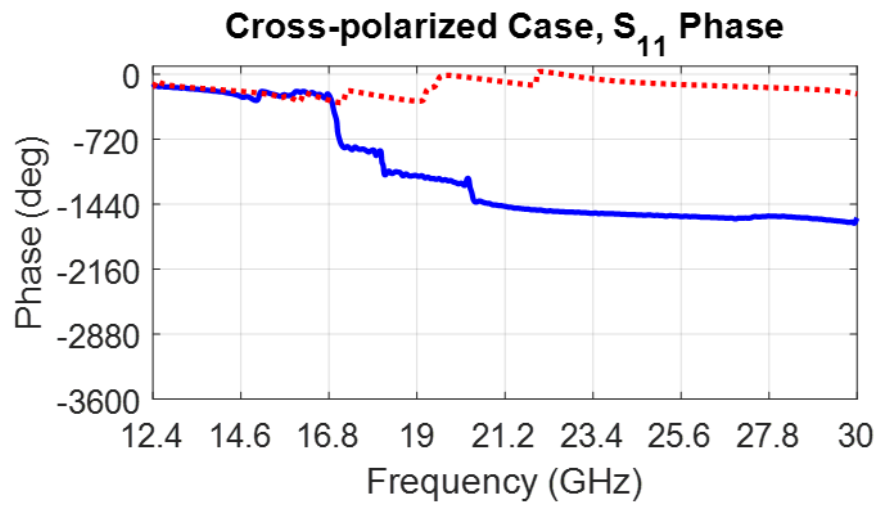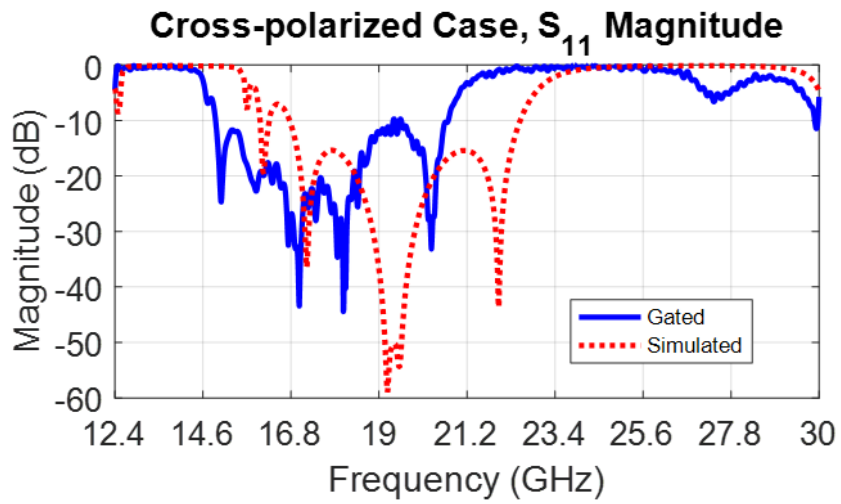
Figure III.15. Simulation and gated measurement results of S_{11} for orientation 2.
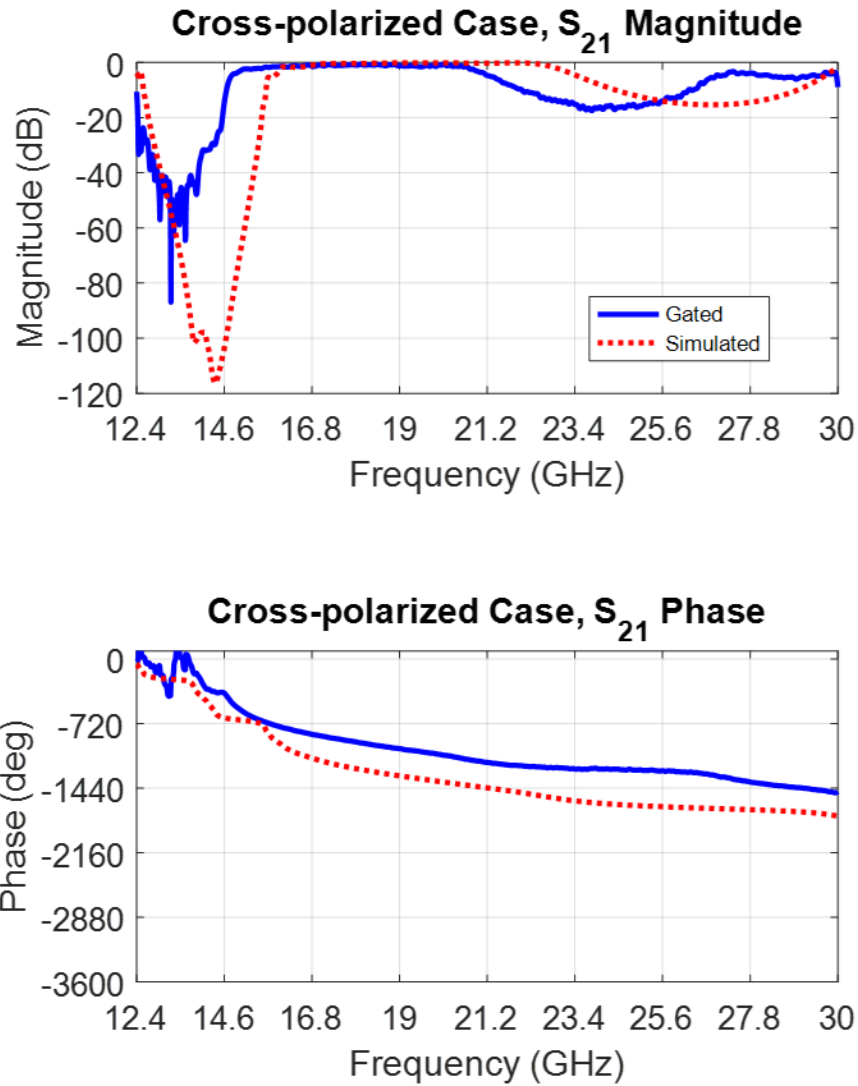
Figure III.16. Simulation and gated measurement results of S_{21} for orientation 2.

Figure III.17 and Figure III.18 below show the permittivity and permeability from orientation 1 as extracted with the NRW algorithm, using the time-domain-gated measurement data and simulation data as sources. Figure III.19 and Figure III.21 below show the permittivity and permeability from orientation 2 as extracted with the NRW algorithm, with Figure III.20 showing the zoomed-out view of the result due to the extreme values of permittivity.
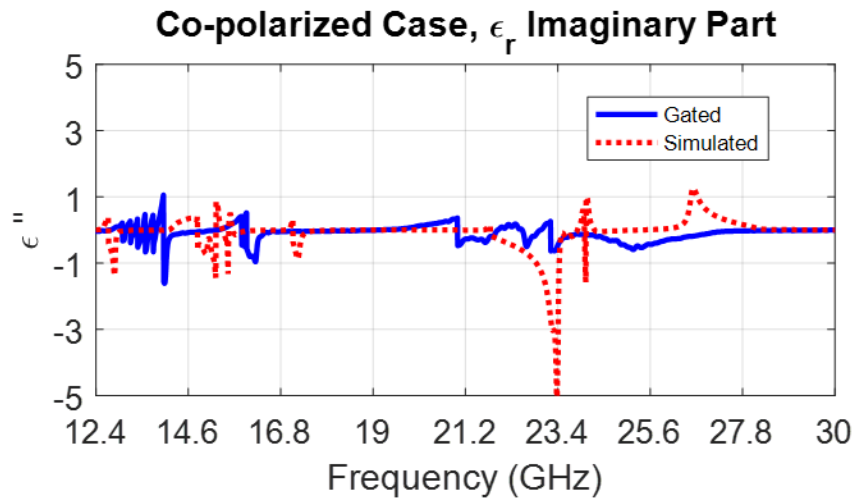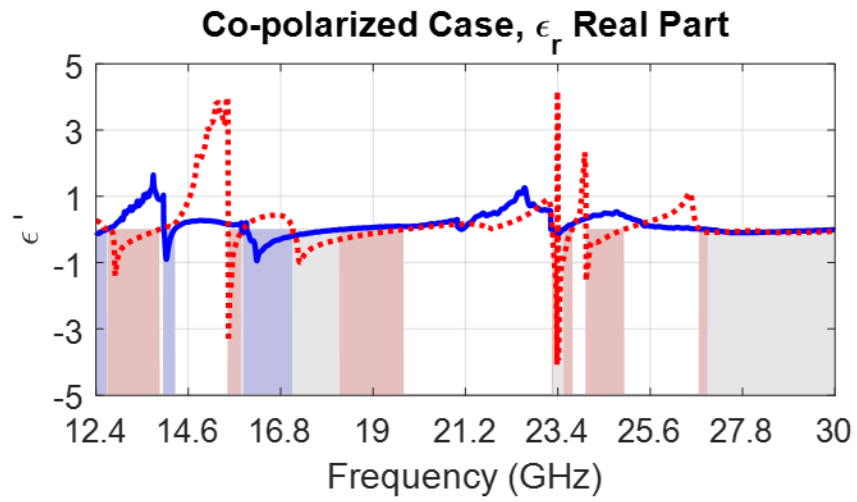
Figure III.17. Extracted permittivity for orientation 1.
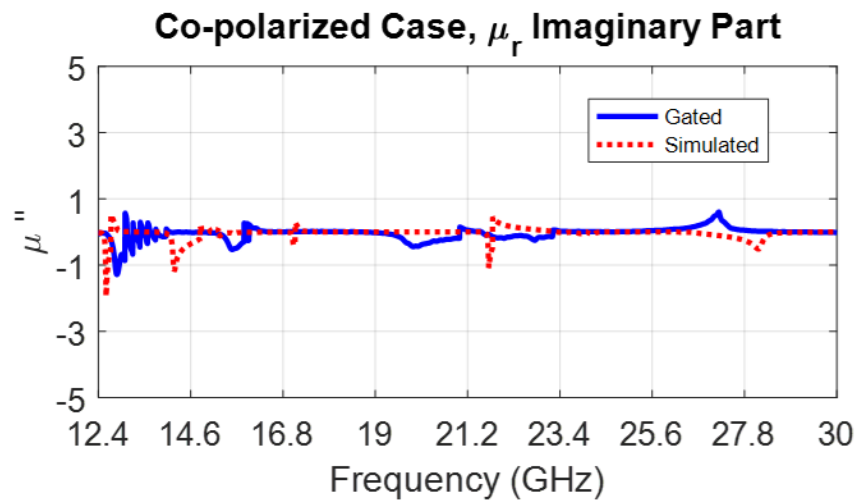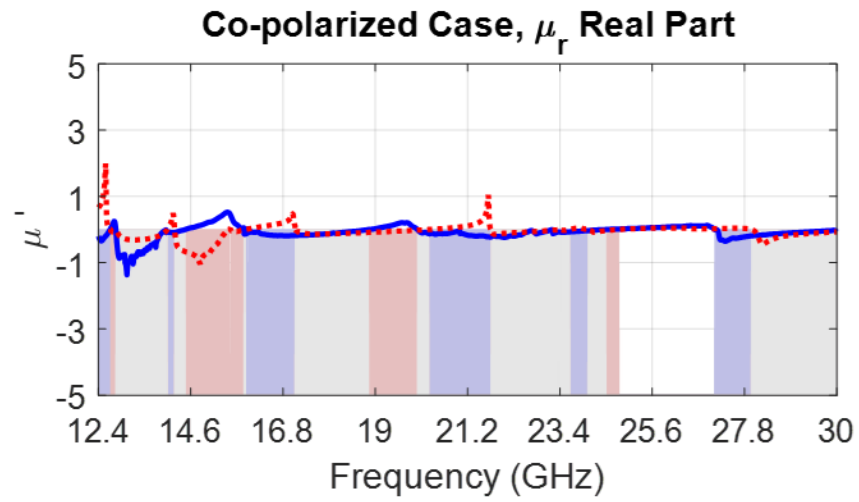
Figure III.18. Extracted permeability for orientation 1.
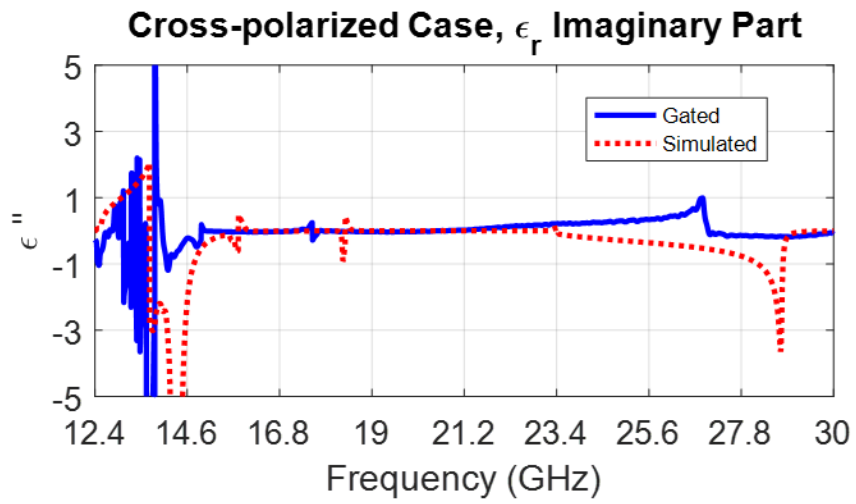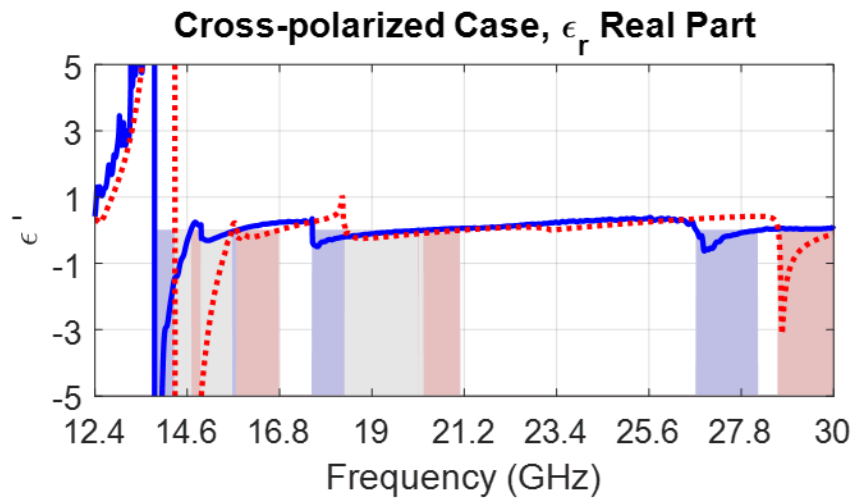
Figure III.19. Extracted permittivity for orientation 2.
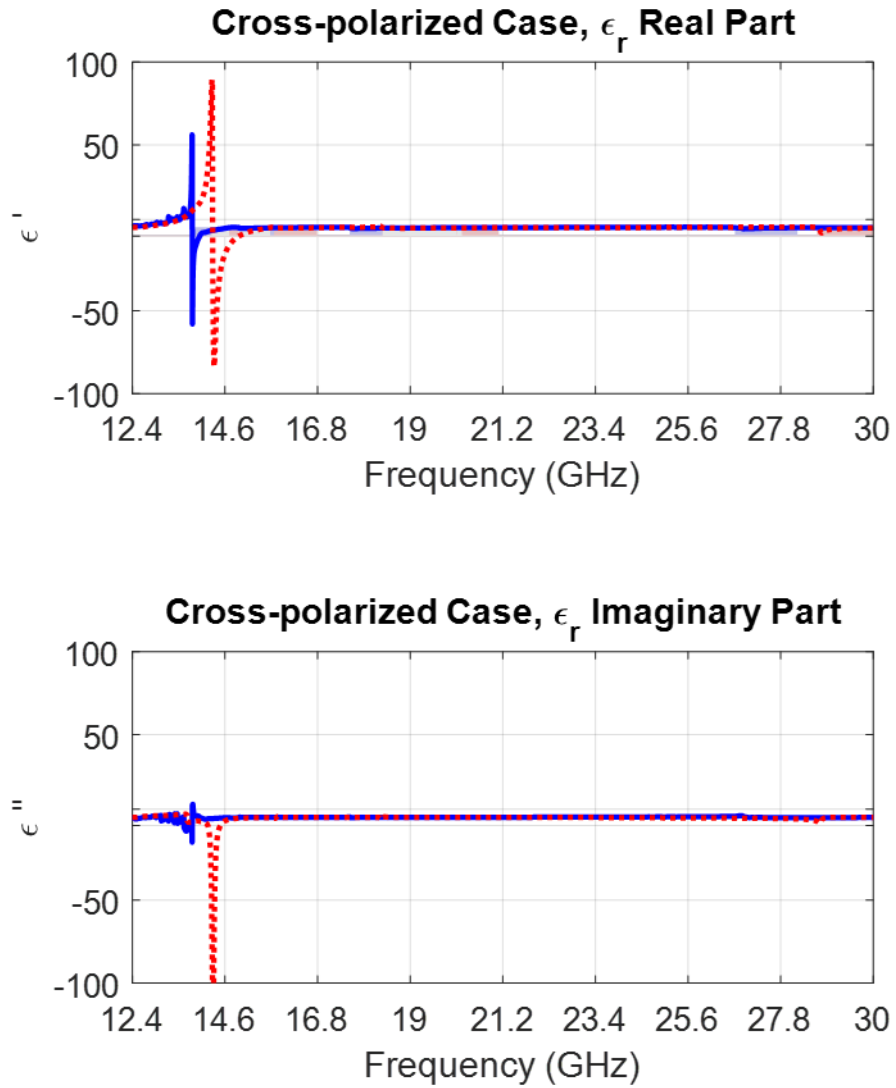
Figure III.20. Extracted permittivity for orientation 2, zoomed-out view.
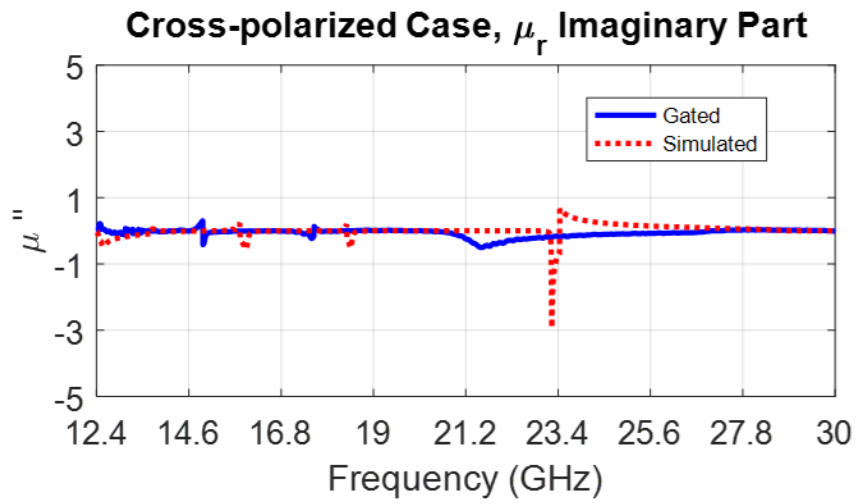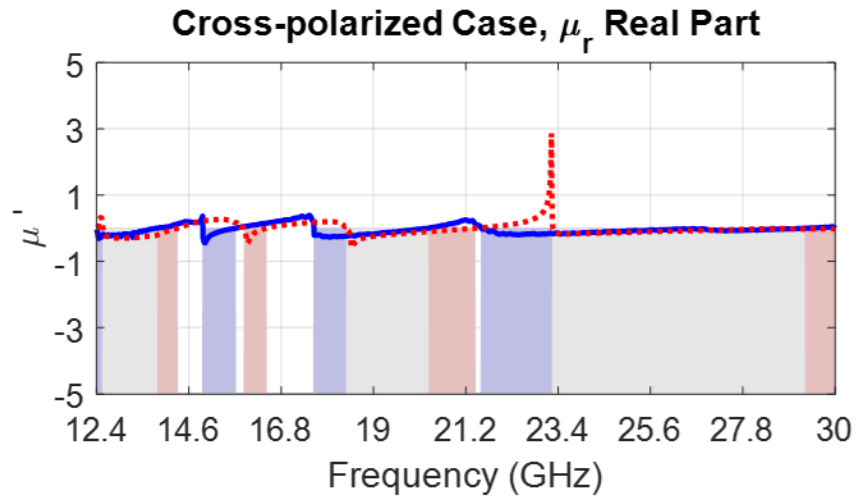
Figure III.21. Extracted permeability for orientation 2.

IV.   Summary and Conclusion

The focus of this work was to bring the University of Arkansas's free-space measurement system back on-line, validate its performance, and use it to determine if the electromagnetic properties of a metamaterial slab agree with its theoretical, simulated properties.

The commonly-encountered dielectric materials Teflon and quartz were used to validate the performance of the system. These materials exhibit very little change in dielectric constant over the frequency range covered by the free-space system. The methods used to extract permittivity from measured S-parameters, such as the Nicolson-Ross-Weir method, are considered sensitive to error. Measuring these benchmark materials and successfully extracting their parameters with low error thus indicates good performance of the system. Teflon and quartz were found to have a permittivity which deviated less than 5% from published values, across the entire span from 12.4 GHz to 110 GHz. Thus, the system's performance has been validated. Additionally, techniques such as time domain gating were presented, which allowed for more accurate measurements with the system by reducing some types of noise and interference.

A metamaterial structure was provided by the United States Army, one which was expected to exhibit negative permittivity, negative permeability and double-negative behavior. The structure was simulated in HFSS on the Arkansas High Performance Computing Center cluster. The simulation was able to converge, and showed several resonant frequencies over the measured range. The NRW method indicated that both negative permittivity and negative permeability would be observed.

Measurements of the metamaterial block using the free-space system showed a significant correlation with simulation results, with a consistent frequency shift observed between simulation and measured results. It is believed that this effect was primarily due to environment-driven

100

changes to the metamaterial's dielectric substrate and copper coating. The metamaterial block had been fabricated some time prior to measurement, allowing enough time for such changes to occur. These effects could have caused a shift in the dielectric constant of the substrate, resulting in a frequency shift of the observed resonances.

In conclusion, the research presented in this thesis demonstrates that the free-space measurement system at the University of Arkansas is a flexible system well-suited to a variety of microwave and millimeter-wave measurements. It has been successfully used to characterize a variety of dielectrics and metamaterials, and may provide useful imaging capabilities in the future.

Bibliography

[1]   R. L. Smith-Rose, "Radio-Wave Propagation Research in the Department of Scientific and Industrial Research During the Years 1937-46," 1947.

[2]   A. von Hippel, "Problems and Progress in Dielectric Research," vol. 7. pp. 69–114, 1967.

[3]   L. S. Liu, Y. Ju, M. J. Chen, and D. N. Fang, "Application of Microwaves for Nondestructive and High-Efficiency Detection of Wall Thinning Locations in a Long-Distance Metal Pipe," *Mater. Trans.*, vol. 52, no. 11, pp. 2091–2097, 2011.

[4]   K. Deepak, W. M. B. W. A, and B. Hilmi, "Microwave nondestructive testing of Malaysian timber for grading applications," 1986.

[5]   R. W. Heath, "Millimeter Wave: The Future of Commercial Wireless Systems," *Tech. Dig. - IEEE Compd. Semicond. Integr. Circuit Symp. CSIC*, vol. 2016–Novem, 2016.

[6]   P. Kumari, N. González-Prelcic, and R. W. Heath, "Investigating the IEEE 802.11ad standard for millimeter wave automotive radar," *IEEE 82nd Veh. Technol. Conf. VTC Fall 2015 - Proc.*, 2016.

[7]   Z. Abichar, Y. Peng, and J. M. Chang, "WiMAX: The emergence of wireless broadband," *IT Prof.*, vol. 8, no. 4, pp. 44–48, 2006.

[8]   U. Reimers, "Digital Video Broadcasting," *IEEE Commun. Mag.*, vol. 36, no. 6, pp. 104–110, 1998.

[9]   B. Ave and K. M. Slenes, "Pulse Power Capability of High Energy Density Capacitors," *IEEE Trans. Magn.*, vol. 37, no. 1, pp. 102–105, 2001.

[10]   T. Tanaka, "Dielectric nanocomposites with insulating properties," *IEEE Trans. Dielectr. Electr. Insul.*, vol. 12, no. 5, pp. 914–928, 2005.

[11]   L. Manchanda and M. Gurvitch, "Yttrium Oxide/Silicon Dioxide: A New Dielectric Structure for VLSI/ULSI Circuits," *IEEE Electron Device Lett.*, vol. 9, no. 4, pp. 180–182, 1988.

[12]   C. P. McShane, "Relative properties of the new combustion resistant vegetable oil based dielectric coolants," *IEEE Cem. Ind. Tech. Conf.*, vol. 37, no. 4, pp. 31–40, 2001.

[13]   B. Chantraine-Barès, R. Sauleau, L. Le Coq, and K. Mahdjoubi, "A new accurate design method for millimeter-wave homogeneous dielectric substrate lens antennas of arbitrary shape," *IEEE Trans. Antennas Propag.*, vol. 53, no. 3, pp. 1069–1082, 2005.

[14] L. Schulwitz and A. Mortazawi, "A new low loss Rotman lens design using a graded dielectric substrate," *IEEE Trans. Microw. Theory Tech.*, vol. 56, no. 12, pp. 2734–2741, 2008.

[15] G. Massie, M. Caillet, M. Cl??net, and Y. M. M. Antar, "A new wideband circularly polarized hybrid dielectric resonator antenna," *IEEE Antennas Wirel. Propag. Lett.*, vol. 9, pp. 347–350, 2010.

[16] D. Guha and Y. M. M. Antar, "New half-hemispherical dielectric resonator antenna for broadband monopole-type radiation," *IEEE Trans. Antennas Propag.*, vol. 54, no. 12, pp. 3621–3628, 2006.

[17] B. Ratni, A. De Lustrac, G. Piau, and S. N. Burokur, "3D Printed Gradient Index Dielectric Metasurface for Beam Steering Applications," in *European Conference on Antennas and Propagation*, 2017, vol. 2, pp. 3413–3415.

[18] M. K. Saleem, M. A. S. Alkanhal, and A. F. Sheta, "Wide Band Hybrid Dielectric Resonator Antenna with Beam Steering Capability," in *IEEE International Symposium on Antenna Technology and Applied Electromagnetics*, 2012.

[19] Y. Yuan, G. Xingchen, and X. Zhi, "A Design of Dielectric Lens Loaded Antenna Array for Beam Steering," in *Antennas, Propagation and EM Theory (ISAPE)*, 2016, pp. 5–8.

[20] P. S. Neelakanta, *Handbook of Electromagnetic Materials*. CRC Press, 1995.

[21] H. Nakano, *Low-Profile Natural and Metamaterial Antennas*. IEEE Press, 2017.

[22] J. Vehmas, P. Alitalo, and S. A. Tretyakov, "Experimental demonstration of antenna blockage reduction with a transmission-line cloak," *IET Microwaves, Antennas Propag.*, vol. 6, no. 7, p. 830, 2012.

[23] V. V. Varadan, "Radar Absorbing Applications of Metamaterials," *IEEE Reg. 5 Tech. Conf. TPS*, pp. 105–108, 2007.

[24] X. Liu, C. Li, K. Yao, X. Meng, and F. Li, "Invisibility cloaks modeled by anisotropic metamaterials based on inductor-capacitor networks," *IEEE Antennas Wirel. Propag. Lett.*, vol. 8, pp. 1154–1157, 2009.

[25] X. Wang, F. Chen, and E. Semouchkina, "Implementation of low scattering microwave cloaking by all-dielectric metamaterials," *IEEE Microw. Wirel. Components Lett.*, vol. 23, no. 2, pp. 63–65, 2013.

[26] A. L. Cullen, "A New Free-wave Method for Ferrite Measurement at Millimeter

Wavelengths," *Radio Sci.*, vol. 22, no. 7, pp. 1168–1170, 1987.

[27]   F. Sagnard, F. Bentabet, and C. Vignat, "In Situ Measurment Of The Complex Permittivity Of Materials Using Reflection Ellipsometry In The Microwave Band: Thery (Part I)," *IEEE Transcations Instrum. Meas.*, vol. 54, no. 3, pp. 1266–1273, 2005.

[28]   C. G. Montgomery, "Technique of Microwave Measurements," *Vol. 11 MIT Radiat. Lab. Ser.*, 1947.

[29]   D. K. Ghodgaonkar, V. V. Varadan, and V. K. Varadan, "A Free-Space Method for Measurement of Dielectric Constants and Loss Tangents at Microwave Frequencies," *IEEE Trans. Instrum. Meas.*, vol. 38, no. 3, pp. 789–793, 1989.

[30]   W. Culshaw and M. V. Anderson, "Measurement of Permittivity and Dielectric Loss with a Millimetre-wave Fabry-Perot Interferometer," *Inst. Electr. Eng.*, vol. May, no. 3763, pp. 820–826, 1962.

[31]   W. Culshaw, "A Spectrometer for Millimetre Wavelengths," *Meas. Sect.*, no. 1445, 1953.

[32]   V. V. Varadan, K. a. Jose, and V. K. Varadan, "In situ Microwave Characterization of Nonplanar Dielectric Objects," *IEEE Trans. Microw. Theory Tech.*, vol. 48, no. 3, pp. 388–394, 2000.

[33]   D. H. Whiffen and H. W. Thompson, "Dielectric Properteis of Water," *Trans. Faraday Soc.*, no. D, 1946.

[34]   C. K. Campbell, "Free-Space Permittivity Measurements on Dielectric Materials at Millimeter Wavelengths," *IEEE Trans. Instrum. Meas.*, vol. 27, no. 1, pp. 54–58, 1978.

[35]   M. N. Afsar, "Dielectric Measurements of Common Polymers at Millimeter Wavelength Range," in *IEEE MTT-S International Microwave Symposium Digest*, 1985, pp. 439–442.

[36]   R. D. Hollinger, K. A. Jose, A. Tellakula, V. V. Varadan, and V. K. Varadan, "Microwave Characterization of Dielectric Materials from 8 to 110 GHz using a Free-space Setup," *Microw. Opt. Technol. Lett.*, vol. 26, no. 2, pp. 100–105, 2000.

[37]   J. P. Dunsmore, *Handbook of Microwave Component Measurements: With Advanced VNA Techniques*. John Wiley & Sons, Inc., 2012.

[38]   B. A. Lengyel, "A Michelson-Type Interferometer Measurements," *Proc. IRE*, no. November, pp. 1242–1244, 1949.

[39]   J. Muñoz, M. Rojo, A. Parreño, and J. Margineda, "Normal and Oblique Incidence Free-

wave Technique for Automatic Measurement of Permittivity and Permeability at Microwave Frequencies," *Instrum. Meas. Technol. Conf. 1996. IMTC-96. Conf. Proceedings. Qual. Meas. Indispens. Bridg. between Theory Reality., IEEE*, pp. 957–92 vol. 2, 1996.

[40]   A. R. T. V. Varadan, Swetha Puligalla, "Experimental Demonstration of Cloaking by Metamaterials," in *Antennas and Propagation Society International Symposium*, 2007, vol. 1, no. 1, pp. 1173–1176.

[41]   U. Kaatze, "Measuring the Eielectric Properties of Materials. Ninety-year Development from Low-frequency Techniques to Broadband Spectroscopy and High-Frequency Imaging," *Meas. Sci. Technol.*, no. 24, 2013.

[42]   W. Culshaw, "High Resolution Millimeter Wave Fabry-Perot Interferometer," *IRE Trans. Microw. Theory Tech.*, vol. 8, no. 2, pp. 182–189, 1960.

[43]   A. M. Nicolson, "Broad-Band Microwave Transmission Characteristics from a Single Measurement of the Transient Response," *IEEE Trans. Instrum. Meas.*, vol. 17, no. 4, pp. 395–402, 1968.

[44]   A. M. Nicolson and G. F. F. Ross, "Measurement of the Intrinsic Properties of Materials by Time-Domain Techniques," *IEEE Trans. Instrum. Meas.*, vol. 19, no. 4, pp. 377–382, 1970.

[45]   W. B. Weir, "Automatic Measurement of Complex Dielectric Constant and Permeability," *Proc. IEEE*, vol. 62, no. 1, pp. 33–36, 1974.

[46]   D. K. Ghodgaonkar, V. V. Varadan, and V. K. Varadan, "Free-Space Measurement of Complex Permittivity and Complex Permeability of Magnetic Materials at Microwave Frequencies," *IEEE Trans. Microw. Theory Tech.*, vol. 39, no. 2, pp. 387–394, 1990.

[47]   C. T. A. Johnk, *Engineering Electromagnetic Fields and Waves*, 2nd ed. John Wiley & Sons, Inc., 1988.

[48]   J. A. Stratton, *Electromagnetic Theory*. 1941.

[49]   F. C. Smith, B. Chambers, and J. C. Bennett, "Calibration Techniques for Free Space Reflection Coefficient Measurements," *IEEE Proc. A Sci. Meas. Technol.*, vol. 139, no. 5, p. 247, 1992.

[50]   Z. Akhter and M. J. Akhtar, "Free-Space Time Domain Position Insensitive Technique for Simultaneous Measurement of Complex Permittivity and Thickness of Lossy Dielectric Samples," *IEEE Trans. Instrum. Meas.*, vol. 65, no. 10, pp. 2394–2405, 2016.

[51]   T. Watanabe, H. Yamada, M. Arii, S. E. Park, and Y. Yamaguchi, "Model experiment of permittivity retrieval method for forested area by using Brewster's angle," *Int. Geosci. Remote Sens. Symp.*, pp. 1477–1480, 2012.

[52]   A. H. Sihvola and I. V. Lindell, "Using Brewster Angle for Measuring Microwave Material Parameters of Bi-isotropic and Chiral Media," *IEEE Microw. Symp. Dig. MTT-S*, pp. 1135–1138, 1992.

[53]   D. E. Muller, "A Method for Solving Algebraic Equations Using an Automatic Computer," *Math. Tables Other Aids to Comput.*, vol. 10, no. 56, pp. 208–215, 1956.

[54]   L. F. Chen, C. K. Ong, C. P. Neo, V. V. Varadan, and V. K. Varadan, *Microwave Electronics: Measurement and Materials Characterisation*. West Sussex: Wiley, 2004.

[55]   V. V. Varadan, R. D. Hollinger, D. K. Ghodgaonkar, and V. K. Varadan, "Free-Space, Broadband Measurements of High-Temperature, Complex Dielectric Properties at Microwave Frequencies," *IEEE Trans. Instrum. Meas.*, vol. 40, no. 5, pp. 842–846, 1991.

[56]   S. Kim and J. Baker-Jarvis, "An Approximate Approach to Determining the Permittivity and Permeability near $\lambda / 2$ Resonances in Transmission / Reflection Measurements," *Prog. Electromagn. Res.*, vol. 58, no. January, pp. 95–109, 2014.

[57]   T. L. Blakney, "Comments on 'Automatic Measurement of Complex Dielectric Constant and Permeability at Microwave Frequencies,'" *Proc. IEEE*, no. January, pp. 203–205, 1975.

[58]   S. Kim and J. Baker-Jarvis, "Approximation for Measuring Complex Material Parameters at $\lambda / 2$ Resonances in Transmission-Line Measurements," in *Asia-Pacific Microwave Conference Proceedings, APMC*, 2013, vol. 1, pp. 1–3.

[59]   J. Baker-Jarvis, "Transmission / Reflection and Short-Circuit Line Permittivity Measurements," 1990.

[60]   Agilent Technologies, *Agilent E8361A Network Analyzer User's Manual*, E8356-9002nd ed. 2003.

[61]   Agilent Technologies, "TRL / LRM Calibration," no. 16000. 2004.

[62]   Keysight Technologies, "Network Analyzer Basics." 2014.

[63]   Keysight Technologies, "Exploring the Architectures of Network Analyzers." 2014.

[64]   Keysight Technologies, "Specifying Calibration Standards and Kits for Agilent Vector Network Analyzers," pp. 1–42, 2011.

[65] Keysight Technologies, "Specifying Calibration Standards and Kits for Keysight Vector Network Analyzers Application Note." 2016.

[66] Keysight Technologies, "Network Analysis: Applying the 8510 TRL Calibration for Non-Coaxial Measurements," vol. 4444. pp. 1–25, 2014.

[67] G. F. Engen and C. A. Hoer, "'Thru-Reflect-Line': An Improved Technique for Calibrating the Dual Six-Port Automatic Network Analyzer," *IEEE Trans. Microw. Theory Tech. Trans. Microw. Theory Tech.*, vol. MTT-27, no. 12, pp. 987–993, 1979.

[68] B. J. Fleury and O. Bernard, "Designing and Characterizing TRL Fixture Calibration Standards for Device Modeling," *Appl. Microw. Wirel.*, no. Figure 2, pp. 26–42, 2001.

[69] B. J. E. Penn, "Virtual Thru-Reflect-Line (TRL) Calibration," *High Frequency Electronics*, pp. 22–30, Apr-2016.

[70] Keysight Technologies, "De-embedding and Embedding S-Parameter Networks Using a Vector Network Analyzer." pp. 1–24, 2004.

[71] Keysight Technologies, "Basics of Measuring the Dielectric Properties of Materials." 2015.

[72] J. Muñoz, M. Rojo, A. Parreño, and J. Margineda, "Automatic measurement of permittivity and permeability at microwave frequencies using normal and oblique free-wave incidence with focused beam," *IEEE Trans. Instrum. Meas.*, vol. 47, no. 4, pp. 886–892, 1998.

[73] Keysight Technologies, "Time Domain Analysis Using a Network Analyzer," pp. 1–48, 2012.

[74] M. Dhillon and P. Dimri, "Design of Metamaterials in HFSS and Extraction of Permittivity and Permeability using NRW Method," *Int. J. Electron. Electr. Comput. Syst.*, vol. 4, no. May, pp. 38–43, 2015.

[75] I. K. Kim and V. V. Varadan, "LTCC Metamaterial Substrates for Millimeter-Wave Applications," *IEEE Reg. 5 Tech. Conf. TPS*, pp. 109–112, 2007.

[76] Ansys Incorporated, *HFSS User's Manual*, 17.1., no. November. 2013.

[77] M. H. Umari, D. K. Ghodgaonkar, V. V. Varadan, and V. K. Varadan, "A Free-Space Bistatic Calibration Technique for the Measurement of Parallel and Perpendicular Reflection Coefficients of Planar Samples," *IEEE Trans. Instrum. Meas.*, vol. 40, no. 1, pp. 19–24, 1991.

[78] A. N. Vicente, G. M. I. Dip, and C. Junqueira, "The Step by Step Development of NRW

Method," *SBMO/IEEE MTT-S Int. Microw. Optoelectron. Conf. Proc.*, pp. 738–742, 2011.

[79]   R. W. Ziolkowski, "Design, Fabrication, and Testing of Double Negative Metamaterials," *IEEE Trans. Antennas Propag.*, vol. 51, no. 7, pp. 1516–1529, 2003.

[80]   J. Shin, A. Akyurltu, and M. Deshpande, "Comments on 'Design, Fabrication and Testing of Double Negative Metamaterials,'" *IEEE Trans. Antennas Propag.*, vol. 53, no. 2, pp. 177–191, 2004.

[81]   Agilent Technologies, "Accurate Measurement of Packaged RF Devices." pp. 1–44, 1995.

[82]   V. G. Veselago, "The Electrodynamics of Substances with Simultaneously Negative Values of Epsilon and Mu," *Sov. Phys. Uspekhi*, vol. 10, no. 4, pp. 509–514, 1968.

[83]   V. V. Varadan and I. K. Kim, "Fabrication of 3-D metamaterials using LTCC techniques for high-frequency applications," *IEEE Trans. Components, Packag. Manuf. Technol.*, vol. 2, no. 3, pp. 410–417, 2012.

[84]   I. K. Kim and V. V. Varadan, "Microstrip patch antenna on LTCC metamaterial substrates in millimeter wave bands," *IEEE Int. Symp. Antennas Propag. Usn. Natl. Radio Sci. Meet. APSURSI*, pp. 0–3, 2008.

V.   Appendix A: Antenna Polarization Measurements

The polarization of the horn-lens antennas was determined experimentally using the RF anechoic chamber at the University of Arkansas. The anechoic chamber is equipped with a dual linearly-polarized ridged horn antenna, shown below in Figure V.1.
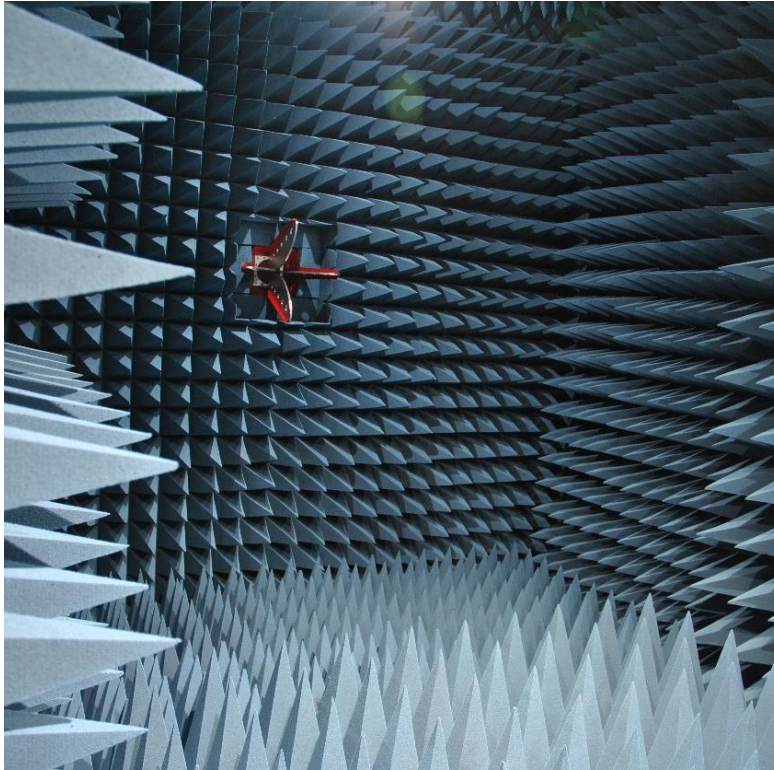
Figure V.1. RF anechoic chamber with linearly-polarized ridged horn antenna.

When using a linearly polarized antenna to measure an antenna under rotation about the phi axis, three possible measurement cases present themselves. These are shown below in Figure V.2.

Circular case:
Pattern does not vary with rotation in Phi direction

Elliptical case:
Pattern varies with rotation in Phi direction; No nulls in pattern

Linear case:
Pattern varies with rotation in Phi direction; Nulls occur at angle of polarization mismatch
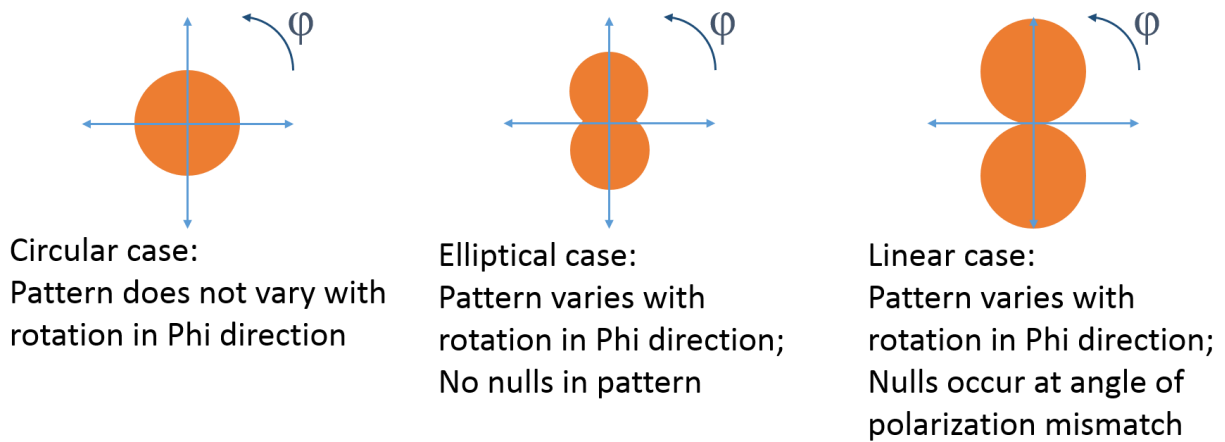
Figure V.2. Possible radiation patterns when rotating an unknown antenna about the phi axis.

To determine the polarization of the horn-lens antennas, one of the horn-lens antennas was mounted inside the RF anechoic chamber, shown below in Figure V.4. A sketch of the measurement setup is shown below in Figure V.3. The unknown antenna is rotated about the phi axis while recording the transmitted signal S_{21} with a network analyzer.
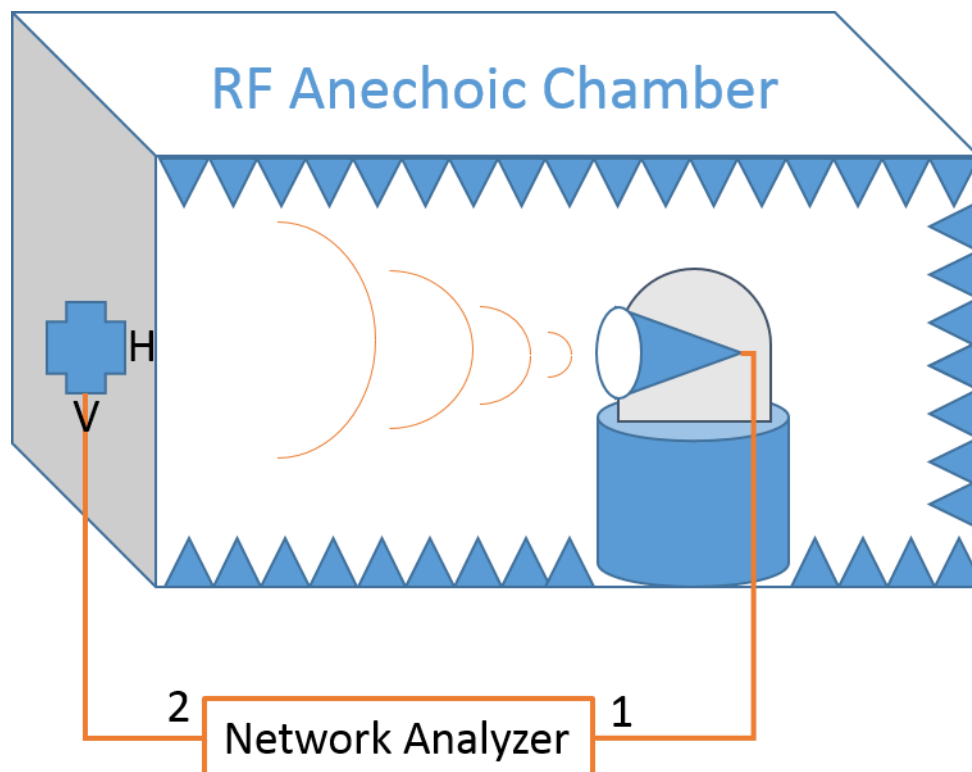
Figure V.3. Experimental setup for determining antenna polarization.
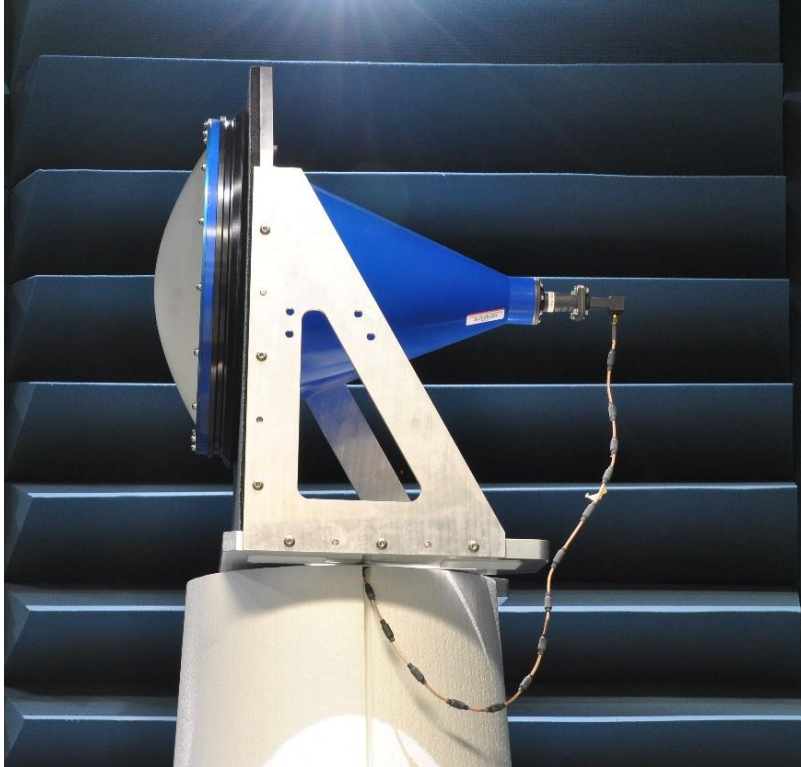
Figure V.4. Horn-lens antenna mounted in the RF anechoic chamber.

The antenna was then rotated about the phi axis. The radiation pattern was recorded for both the horizontal and vertical polarizations of the receiving horn antenna. The results are presented as normalized radiation patterns below in Figure V.5 and Figure V.6. These results clearly correspond with the case of a linearly-polarized antenna under rotation, and thus the horn-lens antennas are linearly polarized.

Horizontal Polarization Pattern
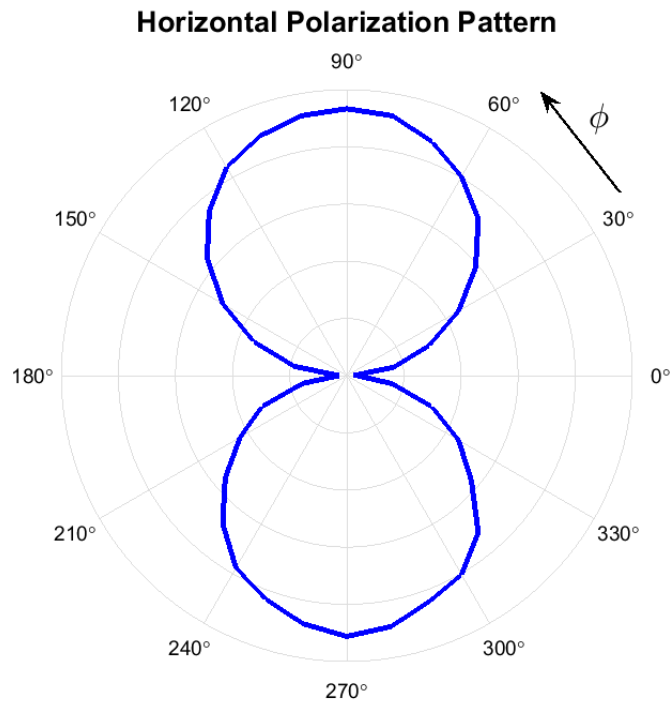
Figure V.5. Horizontal polarization pattern for horn-lens antenna under test.

Vertical Polarization Pattern
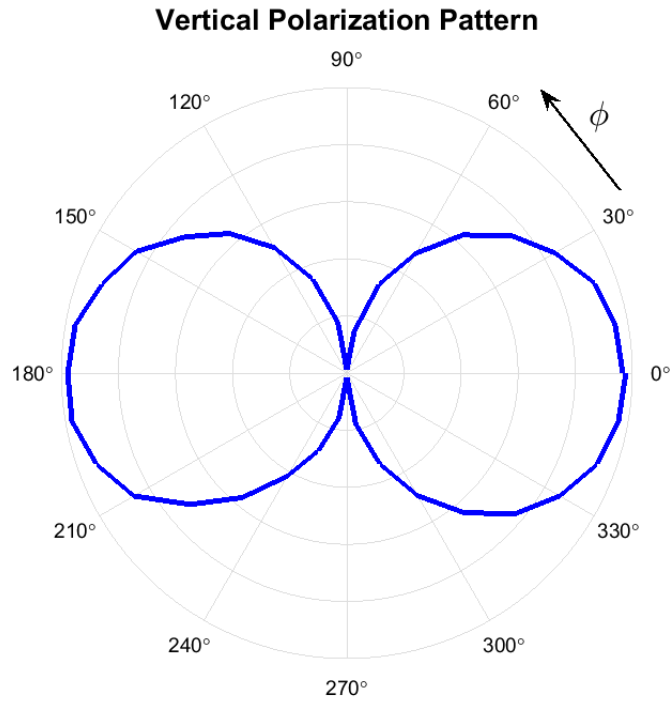
Figure V.6. Vertical polarization pattern for horn-lens antenna under test.

112

VI.　　Appendix B: MATLAB Codes

1. Nicolson-Ross-Weir algorithm

This algorithm uses the Nicolson-Ross-Weir method to extract permittivity and permeability values from transmission and reflection measurement data. It accepts complex-valued, linear-scaled scattering parameter data S_{11} and S_{21} and returns complex-valued epsilon and mu values.

```matlab
function [ eps, mu ] = nrw_extract( d, freq, S11, S21 )
% nrw_extract calculates the permittivity and permeability for a sample.
%
% nrw_extract implements the NRW (Nicholson-Ross-Weir) method for extraction
% of complex permittivity (epsilon) and complex permeability (mu) of a given
% material sample.  This method uses transmission scattering-parameter
% measurements taken with a network analyzer connected to a free-space
% microwave measurement system.
%
% Syntax:  [ eps, mu ] = nrw_extract( d, freq, S11, S21 )
%   Returns:
%     eps - complex-valued vector of permittivity (epsilon)
%     mu - complex-valued vector of permeability (mu)
%   Inputs:
%     d - sample thickness (in meters)
%     freq - real-valued vector of frequency points
%     S11 - complex-valued vector of reflection measurements
%     S21 - complex-valued vector of transmission measurements
% Input vectors f, S11 and S21 should be of equal length.
% S11 and S21 should be in complex (real-imaginary) format,
% not amplitude/phase format.
% Output vectors eps and mu will be of equal length to f.
%
% Implemented by Clifford Kintner, kintner@uark.edu, in 2016 at the
% University of Arkansas, Department of Electrical Engineering.
%
% Note that this method is sensitive to resonances that occur near
% lambda/2 as explained in Sung Kim and James Baker-Jarvis' paper.
% This code can be adapted to waveguide-based measurements by following the
% form in Weir's original paper regarding wavelength inside a waveguide.
%
% Sources:
%   "Measurement of the Intrinsic Properties of Materials by Time-Domain
%   Techniques" Nicholson, A. M. and Ross, G. F., IEEE Transactions on
%   Instrumentation and Measurement, Vol. IM-19, No. 4, November 1970.
%
%   "Automatic Measurement of Complex Dielectric Constant and Permeability
%   at Microwave Frequencies" Weir, W. B., Proceedings of the IEEE, Vol. 62,
%   No. 1, January 1974.
%
%   "An Approximate Approach to Determining the Permittivity and Permeability
%   near lambda/2 Resonances in Transmission/Reflection Measurements" Sung
```

```
%    Kim and James Baker-Jarvis, Progress in Electromagnetics Research B, Vol.
%    58, 2014.
%

for m=1:size(S11)
    % Calculate relationship between S11 and S21 (chi)
    X(m)=(S11(m)^2-S21(m)^2+1)/(2*S11(m));

    % Calculate reflection coefficient (gamma) and reject impossible values
    Gamma(m)=X(m)+sqrt(X(m)^2-1);
    if abs(Gamma(m))<1
        Gamma(m)=X(m)+sqrt(X(m)^2-1);
    else
        Gamma(m)=X(m)-sqrt(X(m)^2-1);
    end

    % Calculate transmission and propagation constants
    T(m)=(S11(m)+S21(m)-Gamma(m))/(1-(S11(m)+S21(m))*Gamma(m));
    gam_0(m)=complex(0,2*pi*freq(m)/(3e8));
    gam(m)=(log(1/T(m))/d);

    % Extract epsilon and mu
    eps(m)=(gam(m)/gam_0(m))*((1-Gamma(m))/(1+Gamma(m)));
    mu(m)=(gam(m)/gam_0(m))*((1+Gamma(m))/(1-Gamma(m)));
end
```

2. Iterative algorithm

This algorithm uses an iterative method to extract permittivity from reflection measurement data. It accepts complex-valued, linear-scaled scattering parameter data S_{11} and returns complex-valued epsilon values.

```
%% Iterative Permittivity Solver v1.3 2015-10-28
% Clifford Kintner [kintner@uark.edu], Dr. Magda El-Shenawee - advisor
% Based on technique from Ghodgaonkar, Varadan & Varadan,
% "A Free-Space Method for Measurement of Dielectric Constants
% and Loss Tangents at Microwave Frequencies" (1989)
%
% This program imports data in the real/imaginary format output by the
% HVS software (similar to the plain text file format of the HP 8510C).
% Only S_11 data is used as the technique in the '89 paper relies on
% measurements of metal-backed samples; S_21=0 is assumed true.
%
% The program then attempts to solve for permittivity of the sample.
% It uses Müller's method to converge, starting with an initial guess
% of epsilon, then solving for the zero of the error between the expected
% and measured S_11 values for a sample.
%
clear all

%% Get sample data and starting parameters
```

```matlab
file_name = input('File containing S_11 data (real/imag format): ','s');
[Freq, S11r, S11i, S21r, S21i] = import_real_imag_hvs(file_name);
S11 = complex(S11r, S11i);
clearvars S21r S21i
f = Freq.*1e9;
disp(strcat(['Data contains',' ',num2str(size(S11r,1)),' points, ', ...
    num2str(min(Freq)),' to ',num2str(max(Freq)),' GHz']))
thickness = input('Sample thickness (in mm): ');
d = thickness*0.001;
eps_guess = input('Initial guess for relative epsilon: ');
guess_margin = input('Initial over/under for epsilon (default: 0.25)');
if isempty(guess_margin)
    guess_margin = 0.25;
end
itmax = input('Max iterations per point (default: 500): ');
if isempty(itmax)
    itmax = 500;
end
itmaxhits = 0;
clearvars file_name thickness Freq S11r S11i;

%% Main program loop - process all data points
for (m=1:size(Freq))
    eps_guess_1 = eps_guess - guess_margin;
    eps_guess_2 = eps_guess;
    eps_guess_3 = eps_guess + guess_margin;

    y0 = S11(m) - get_S11_expected(eps_guess_1,d,f(m));
    y1 = S11(m) - get_S11_expected(eps_guess_2,d,f(m));
    y2 = S11(m) - get_S11_expected(eps_guess_3,d,f(m));

    %% Do Müller's method to find epsilon for a single point
    for it = 4:itmax                                    % already did 3 its
        q = (eps_guess_3 - eps_guess_2)/(eps_guess_2 - eps_guess_1);
        A = (q)*y2 - (q*(1+q))*y1 + (q^2)*y0;
        B = (2*q + 1)*y2 - ((1 + q)^2)*y1 + (q^2)*y0;
        C = (1 + q)*y2;

        if (A ~= 0)                                     % don't divide by 0
            disc = B^2 - 4*A*C;
            den1 = (B + sqrt(disc));
            den2 = (B - sqrt(disc));

            if (abs(den1) < abs(den2))
                eps_guess_4 = eps_guess_3 - ...
                    (eps_guess_3 - eps_guess_2)*(2*C/den2);
            else
                eps_guess_4 = eps_guess_3 - ...
                    (eps_guess_3 - eps_guess_2)*(2*C/den1);
            end

        elseif (B ~= 0)                                 % don't divide by 0
            eps_guess_4 = eps_guess_3 - ...
                (eps_guess_3 - eps_guess_2)*(2*C/B);
        else
            itcount(m) = it;
```

115

```matlab
                break
        end


        % equation (4), error between measured and expected S11
        y3 = S11(m) - get_S11_expected(eps_guess_4,d,f(m));


        eps_guess_1 = eps_guess_2;                      % shift eps guesses
        eps_guess_2 = eps_guess_3;
        eps_guess_3 = eps_guess_4;


        y0 = y1;                                        % recycle outputs
        y1 = y2;
        y2 = y3;
    end

%% Store the result of Müller's method before moving on to the next point
    eps(m) = eps_guess_3;
    E(m) = y2;
    if (it==itmax)          % save our it count if we didn't hit 0 for A or B
        itcount(m) = itmax;
        itmaxhits = itmaxhits + 1;
    end


end


%% Show some basic statistics
divergences = 0;
eps_sum = 0;                                            % initialize salts
for (m=1:size(S11))
    if (eps(m) > 10*eps_guess)      % guess was way off, or answer diverged
        divergences = divergences + 1;
    elseif (eps(m) < 1)                         % epsilon > 1 unless vacuum
        divergences = divergences + 1;
    else
        if ((eps(m) > 1) && (eps(m) < 10*eps_guess))
            eps_sum = eps_sum + eps(m);         % add epsilon for our mean
        end
    end
end
eps_average = eps_sum / ((size(S11,1) - divergences));    % calculate mean

disp(' ')
disp('Results:')
disp(strcat(['Epsilon min/max: ',num2str(min(eps)),' / ', ...
    num2str(max(eps))]))
disp(strcat(['S11 error min/max: ',num2str(min(E)),' / ', ...
    num2str(max(E)),' [',num2str(20.*log10(abs(min(E)))),' / ', ...
    num2str(20.*log10(abs(max(E)))),' dB]']))
disp(strcat(['Mean iterations per point: ',num2str(mean(itcount))]))
disp(strcat(['Max iterations reached ',num2str(itmaxhits),' times']))
disp(strcat(['Divergence count: ',num2str(divergences),' points']))
disp(strcat(['Average epsilon (next starting guess?): ', ...
    num2str(eps_average)]))

realeps=[f real(eps)'];
```

```matlab
exit

function [ expected_S11 ] = get_S11_expected( expected_eps,d,f )
% get_S11_expected calculates the expected S11 value from a real-valued
% relative permittivity/dielectric constant/epsilon (expected_eps), with
% a sample thickness (d, in meters) and frequency (f, in Hz) as inputs.
% The result is a complex-valued reflection scattering parameter (S11).
%
% Based on technique from Ghodgaonkar, Varadan & Varadan,
% "A Free-Space Method for Measurement of Dielectric Constants
% and Loss Tangents at Microwave Frequencies" (1989)

% equation (2), normalized wave impedance in the dielectric material
expected_Z_dn = 1/sqrt(expected_eps);

% equation (3), phase constant in the dielectric material
% freespace wavelength = c/f
expected_beta_d = 2*pi*sqrt(expected_eps) / ((3e8)/(f));

% equation (1), complex reflection coefficient
expected_S11_num = j*expected_Z_dn*tan(expected_beta_d*d) - 1;
expected_S11_den = j*expected_Z_dn*tan(expected_beta_d*d) + 1;
expected_S11_den_recip = (expected_S11_den).^-1;
expected_S11 = expected_S11_num*expected_S11_den_recip;

end
```

3. Time-domain gating algorithm

This algorithm performs time-domain gating on complex-valued, linear-scaled scattering

parameter data S_{11} and S_{21}. It returns complex-valued scattering parameter data and shows decibel-

scaled amplitude response before and after the gating process.

```matlab
function [ S11_out, S21_out ] = tdgator( S11_in, S21_in, FreqAxis )
%TDGator v6 -- Clifford Kintner
%   TDGator now only uses a Kaiser window as this is the
%   function used in most Network Analyzers.
%   This is chosen as the Kaiser-Bessel window is the
%   simplest implementation of the DPSS (Slepian) window,
%   which maximizes the energy concentration in the main lobe
%   of the fourier-transformed signal.

N = size(FreqAxis,1);
gate_width = input(strcat('Gate width (',num2str(N),' samples total):',32));
    if (mod(N-gate_width,2)==1) gate_width = gate_width + 1; end
beta = input(strcat('Kaiser window beta (default is 2.5):',32));
    if (isempty(beta)); beta=2.5; end
gate_shape = [zeros(1,(N-gate_width)/2) kaiser(gate_width,beta)' ...
  zeros(1,(N-gate_width)/2)]';
```

```
% truncate gate if it's oversized
if gate_width > N
    left_gate = (gate_width - N)/2;
    right_gate = gate_width - left_gate - 1;
    truncated_gate = gate_shape(left_gate:right_gate);
    gate_shape = truncated_gate;
end

% do transform and gating
S11_in_td = ifftshift(ifft(S11_in));
S21_in_td = ifftshift(ifft(S21_in));
S11_td_gated = gate_shape.*S11_M_O1_td;
S21_td_gated = gate_shape.*S21_M_O1_td;
S11_gated = fft(fftshift(S11_td_gated));
S21_gated = fft(fftshift(S21_td_gated));

figure(1)
subplot(5,1,1); plot(20*log10(abs(S11_M_O1_copol)))
subplot(5,1,2); plot(20*log10(abs(S11_M_O1_td)))
subplot(5,1,3); plot(gate_shape)
subplot(5,1,4); plot(20*log10(abs(S11_M_O1_td_gate)))
subplot(5,1,5); plot(20*log10(abs(S11_M_O1_gated)))
disp('Pausing...')
pause
end
```

4. Waveguide cutoff frequencies calculator

This code demonstrates the calculation of cutoff frequencies for a variety of waveguide sizes. The common waveguide dimensions used in this research are stored in the vectors "a" and "b" which contain the longer and shorter interior dimensions, respectively, of the waveguide.

```
clc
clear all
c0 = 299792458;
mu0 = 4 * pi * 1e-7;
eps0 = (mu0 * c0 * c0)^-1;

a = [0.0157988 0.010668 0.007112 0.0056896 0.0037592 0.00254];
b = [0.0078994 0.004318 0.003556 0.0028448 0.0018796 0.00127];

for m = [1 2 3]
    for n = [1 2 3]
        for wg = 1:length(a)
            fc(wg,m,n) = (1/(2*sqrt(mu0*eps0)))*sqrt(((m-1)/a(wg))^2 + ((n-
1)/b(wg))^2)*1e-9;
        end
    end
end

fc1 = [fc(1,1,1) fc(1,1,2) fc(1,1,3) fc(1,2,1) fc(1,2,2) fc(1,2,3) ...
```

```
    fc(1,3,1) fc(1,3,2) fc(1,3,3)]
fc2 = [fc(2,1,1) fc(2,1,2) fc(2,1,3) fc(2,2,1) fc(2,2,2) fc(2,2,3) ...
    fc(2,3,1) fc(2,3,2) fc(2,3,3)]
fc3 = [fc(3,1,1) fc(3,1,2) fc(3,1,3) fc(3,2,1) fc(3,2,2) fc(3,2,3) ...
    fc(3,3,1) fc(3,3,2) fc(3,3,3)]
fc4 = [fc(4,1,1) fc(4,1,2) fc(4,1,3) fc(4,2,1) fc(4,2,2) fc(4,2,3) ...
    fc(4,3,1) fc(4,3,2) fc(4,3,3)]
fc5 = [fc(5,1,1) fc(5,1,2) fc(5,1,3) fc(5,2,1) fc(5,2,2) fc(5,2,3) ...
    fc(5,3,1) fc(5,3,2) fc(5,3,3)]
fc6 = [fc(6,1,1) fc(6,1,2) fc(6,1,3) fc(6,2,1) fc(6,2,2) fc(6,2,3) ...
    fc(6,3,1) fc(6,3,2) fc(6,3,3)]
```

5. Import_Real_Imag_HVS

This supporting code loads complex-valued data from the HVS free-space measurement system for processing with the extraction algorithms included in this research.

```matlab
function [Freqaxis,S11r,S11i,S21r,S21i] = import_real_imag_hvs(filename,
startRow, endRow)
% This code loads data files from the HVS system in real/imaginary format.
% If startRow and endRow are omitted, the entire file is processed.
%

%% initialize variables
if nargin<=2
    startRow = 4;
    endRow = inf;
end
formatSpec = '%7f%15f%15f%15f%f%[^\n\r]';

%% open the text file
fileID = fopen(filename,'r');

%% read columns of data according to format string
dataArray = textscan(fileID, formatSpec, endRow(1)-startRow(1)+1, ...
    'Delimiter', '', 'WhiteSpace', '', 'HeaderLines', startRow(1)-1, ...
    'ReturnOnError', false);
for block=2:length(startRow)
    frewind(fileID);
    dataArrayBlock = textscan(fileID, formatSpec, ...
        endRow(block)-startRow(block)+1, 'Delimiter', '', 'WhiteSpace',...
        '', 'HeaderLines', startRow(block)-1, 'ReturnOnError', false);
    for col=1:length(dataArray)
        dataArray{col} = [dataArray{col};dataArrayBlock{col}];
    end
end

%% close the text file
fclose(fileID);

%% allocate imported array to column variable names
Freqaxis = dataArray{:, 1};
```

```
S11r = dataArray{:, 2};
S11i = dataArray{:, 3};
S21r = dataArray{:, 4};
S21i = dataArray{:, 5};

return
```

6. S_converter

This supporting code performs conversion between the various formats of scattering parameters. It can accept linear-scaled or decibel-scaled inputs, in amplitude/phase or complex-valued format. It can return results in these formats, and can perform unwrapping of phase for amplitude/phase form data.

```
function [ out1, out2 ] = S_converter( in1, in2, form_in1, form_in2,
form_out1, form_out2 )
%S_converter converts S-parameters between common units
% v1.3 Clifford Kintner
%   in1 and in2 are input vectors, out1 and out2 are output vectors
%   form_in1 and form_out1 can be the following:
%     mag_lin  - magnitude in linear scale
%     mag_db   - magnitude in dB scale
%     real_lin - real part of complex form (linear scale)
%   form_in2 and form_out2 can be the following:
%     imag_lin - imaginary part of complex form (linear scale)
%     pha_deg  - phase in degrees
%     pha_rad  - phase in radians
%     pha_degu - phase in degrees, unwrapped (output only)
%     pha_degu - phase in radians, unwrapped (output only)
%   S_converter internally uses complex (real/imaginary) format;
%     some loss of precision will naturally occur.
%   Complex (real/imaginary) format may not be mixed with other
%     units, i.e. if form_in1 is real_lin then form_in2 must be
%     imag_lin.  The same holds true for outputs.

%% convert inputs to real / imaginary format
if (strcmp(form_in1,'mag_db'))  % put in linear units first
    in1_b = 10.^(in1./20); in1 = in1_b;
    form_in1='mag_lin';
end  % end if form_in1

if (strcmp(form_in2,'pha_deg'))  % put in radians first
    in2_b = deg2rad(in2); in2 = in2_b;
    form_in2='pha_rad';
end  % end if form_in2

switch (form_in1)
    case ('mag_lin')  % form_in1
        switch (form_in2)
```

```matlab
            case ('pha_rad')  % form_in2
                % convert to real/imaginary
                in0 = complex(in1.*cos(in2), in1.*sin(in2));
            case ('imag_lin')  % form_in2
                error('Can''t mix real/imaginary units')
            otherwise  % form_in2
                error('Bad input on form_in2')
        end  % end switch form_in2

    case ('real_lin')  % form_in1
        if strcmp(form_in2,'imag_lin')
            % join real/imaginary to complex
            in0 = complex(in1,in2);
        else
            error('Can''t mix real/imaginary units for input')
        end  % end if form_in2

    otherwise  % form_in1
        error('Bad input on form_in1')
end  % end switch form_in1

%% convert outputs to desired format
    switch (form_out1)
        case ({'mag_lin','mag_db'})  % form_out1
            out1 = abs(in0);
            switch (form_out2)
                case ('pha_deg')  % form_out2
                    out2 = rad2deg(angle(in0));
                case ('pha_degu')  % form_out2
                    out2 = rad2deg(unwrap(angle(in0)));
                case ('pha_rad')  % form_out2
                    out2 = angle(in0);
                case ('pha_radu')  % form_out2
                    out2 = unwrap(angle(in0));
                otherwise  % form_out2
                    error('Bad input on form_out2')
            end  % end switch form_out2

        case ('real_lin')  % form_out1
            if (strcmp(form_out2,'imag_lin'))
                out1 = real(in0);
                out2 = imag(in0);
                % do nothing
            else
                error('Can''t mix real/imaginary units for output')
            end  % end if form_out2
        otherwise  % form_out1
            error('Bad input on form_out1')
    end  % end switch form_out1

if (strcmp(form_out1,'mag_db'))  % convert to decibel scale
    out1_b = 20*log10(out1); out1 = out1_b;
end  % end if out_form1
end
```